SPECIFIC ABSORPTION RATE CALCULATIONS USING FINITE DIFFERENCE TIME DOMAIN METHOD

A THESIS SUBMITTED TO
THE GRADUATE SCHOOL OF NATURAL AND APPLIED SCIENCES
OF
THE MIDDLE EAST TECHNICAL UNIVERSITY

BY

İBRAHİM TÜRER

IN PARTIAL FULFILLMENT OF THE REQUIREMENTS
FOR
THE DEGREE OF MASTER OF SCIENCE
IN
ELECTRICAL AND ELECTRONICS ENGINEERING

AUGUST 2004

Approval of the Graduate School of Natural and Applied Sciences

_____

Prof.Dr.Canan Özgen

Director

I certify that this thesis satisfies all the requirements as a thesis for the degree of Master of Science.

_____

Prof. Dr. Mübeccel Demirekler

Chair of Electrical and Electronics Engineering Department

This is to certify that we have read this thesis and that in our opinion it is fully adequate, in scope and quality, as a thesis for the degree of Master of Science.

Prof. Dr. Mustafa Kuzuoğlu

Supervisor

Examining Committee Members

Assoc. Prof. Dr. Sencer Koç	(METU, EE)	_____
Prof. Dr. Mustafa Kuzuoğlu	(METU, EE)	_____
Assoc. Prof. Dr. Gülbin Dural	(METU, EE)	_____
Asst. Prof. Dr. Lale Alatan	(METU, EE)	_____
Prof. Dr. Adnan Köksal	(HU, EE)	_____

I hereby declare that all information in this document has been obtained and presented in accordance with academic rules and ethical conduct. I also declare that, as required by these rules and conduct, I have fully cited and referenced all material and results that are not original to this work.

Name, Last name : İBRAHİM TÜRER

Signature :

ABSTRACT

SPECIFIC ABSORPTION RATE CALCULATIONS USING
FINITE DIFFERENCE TIME DOMAIN METHOD

Türer, İbrahim

MSc., Department of Electrical and Electronics Engineering

Supervisor : Prof. Dr. Mustafa Kuzuoğlu

August 2004, 106 pages

This thesis investigates the problem of interaction of electromagnetic radiation with human tissues. A Finite Difference Time Domain (FDTD) code has been developed to model a cellular phone radiating in the presence of a human head. In order to implement the code, FDTD difference equations have been solved in a computational domain truncated by a Perfectly Matched Layer (PML). Specific Absorption Rate (SAR) calculations have been carried out to study safety issues in mobile communication.

Keywords: FDTD, PML, SAR, mobile communication

ÖZ

ZAMANDA FARKLAR METODU KULLANILARAK ÖZGÜL EMİLİM ORANI HESAPLAMALARI

Türer, İbrahim
Yüksek Lisans, Elektrik ve Elektronik Mühendisliği Bölümü
Tez Yöneticisi: Prof. Dr. Mustafa Kuzuoğlu

Ağustos 2004, 106 sayfa

Bu tezde elektromanyetik radyasyonun insan dokularıyla olan etkileşimi araştırılmıştır. İnsan kafasının yakınında radyasyon yayan bir cep telefonunu modellemek için zamanda sonlu farklar (ZSF) kodu geliştirilmiştir. Kodu uygulayabilmek için ZSF fark denklemleri Mükemmel Eşlenmiş Katman (MEK) ile sonlandırılmış bir uzayda çözülmüştür. Mobil haberleşmedeki güvenlik sorunlarını incelemek için Özgül Emilim Oran (ÖEO) hesaplamaları yapılmıştır.

Anahtar Kelimeler: ZSF, MEK, ÖEO, mobil haberleşme

ACKNOWLEDGMENTS

The author wishes to express his deepest gratitude to his supervisor, Prof. Dr. Mustafa Kuzuoğlu, for his guidance, advice, criticism, encouragement and insight throughout the research without which this thesis work could never be completed.

The author also would like to thank Prof. Dr. Nilgün Günalp, for her suggestions and comments.

The technical assistance of Prof. Dr. Levent Çelik at Maltepe University Medicine Faculty Radiology Department, about the MRI images used in my thesis is gratefully acknowledged.

To My Family

TABLE OF CONTENTS

LIST OF TABLES

TABLES

LIST OF FIGURES

FIGURES

CHAPTER 1

INTRODUCTION

1.1 Numerical Solution of Electromagnetic Initial/Boundary Value Problems

Electromagnetic radiation/scattering problems may be modeled as initial/boundary value problems governed by partial differential equations subject to properly defined initial and/or boundary values. The spatial domain of the initial/boundary value problem may be quite complicated in general, and the direct analytical solution of the problem is usually impossible. As a result, spatial and/or temporal discretization is employed for the approximate numerical solution of the problem. To this end, several approximate solution techniques have been developed so far, the most important ones being the Method of Moments (MoM), the Finite Element Method (FEM) and the Finite Difference Time Domain (FDTD) method. There are also hybrid methods which employ combinations of different approaches (such as combining FEM and MoM) as well as combinations of numerical and asymptotic techniques. A summary of the most frequently-used numerical techniques is given below.

1.1.1 The Method of Moments (MoM)

The Method of Moments (MoM), which has been introduced by Harrington [1], is one of the most popular numerical methods developed for the solution of electromagnetic boundary value problems. The electromagnetic scattering/radiation problem is first

modeled in terms of an integral equation, and the unknown function is approximated as a linear combination of explicitly defined functions known as shape functions. The last step of the MoM approach is the reduction of the operator equation to a matrix equation by taking the inner product of the operator equation with a set of weight functions. A major drawback of the MoM approach is the difficulty encountered in the construction of the Green's function (which is the kernel of the operator equation) in certain applications. However, for problems involving PEC (Perfect Electric Conductor) objects in free space, the method brings forth a reduction in dimension (A three-dimensional (3D) problem is modeled as an integral equation on a two-dimensional (2D) surface, and a 2D problem is reduced to an integral equation defined on a one-dimensional (1D) curve), which leads to a reduction in the number of unknowns. The resulting MoM matrix is full, due to the fact that the kernel of the integral operator links any spatial point to all the remaining spatial points. This last property may also be interpreted as a consequence of the non-local character of integral operators.

1.1.2 The Finite Element Method (FEM)

The Finite Element Method (FEM) [2] has been introduced to solve boundary value problems governed by partial differential equations, and hence, it requires the discretization of the entire problem domain. As a first step, the boundary value problem is expressed in terms of an equivalent weak variational formulation. Next, the spatial domain is divided into a number of subdomains, known as elements. The unknown function is approximated in terms of locally defined shape functions, leading to a sparse matrix equation. The major strength of the FEM is its ability to model complex-shaped domains and inhomogeneous material objects. The method is very flexible since the elements can be chosen to closely conform the original geometry of material boundaries. A major difficulty in the FEM is mesh truncation, i.e. the termination of the unbounded spatial domain by an absorbing boundary. Several methods have been proposed to achieve efficient mesh truncation, in terms of suitably-defined Absorbing Boundary

Conditions (ABCs) [3], and the more recently-introduced Perfectly Matched Layers (PMLs) [4].

The MOM and FEM can be interpreted as projection methods, where an approximate solution is sought as a linear combination of shape functions, which means that the exact solution is projected to the subspace spanned by the shape functions.

1.1.3 The Finite Difference Time Domain (FDTD) Method

The FDTD method, which has been introduced by Yee [5], is based on the direct discretization of Maxwell's curl equations. The spatial and temporal partial differential operators are approximated by their finite difference counterparts in such a way that there is spatio-temporal staggering in the definition of space-time points for the electric and magnetic field vectors. This property of the FDTD algorithm is very important in the iterative solution of the field quantities starting from an initial value. The method is easy to understand, easy to implement as software, and since it is a time-domain technique, a single simulation run can cover a wide frequency range provided that the excitation is a wide-band signal.

Since the FDTD is a time-domain technique which evaluates the electromagnetic field intensities everywhere in the computational domain, it lends itself to providing animation displays (movies) of the spatio-temporal field variation throughout the model. This capability is extremely useful to understand exactly what is going on in the model, and to help insure that the model is working correctly.

In addition, the FDTD method allows the user to specify the material parameters at all points within the computational domain. The constitutive parameters of conducting, dielectric as well as magnetic materials can be modeled without too much effort.

Since the computational domain must be bounded, one must employ a domain truncation approach in FDTD simulations for radiation/scattering problems where the physical domain extends to infinity. Similar to the FEM case, domain truncation in FDTD can be achieved by defining ABCs over the outer boundary or by a PML.

The FDTD technique offers many advantages as an electromagnetic modeling, simulation, and analysis tool. Its capabilities include [6]:

1. Broadband response predictions centered about the system resonances
2. Arbitrary three-dimensional (3-D) model geometries
3. Interaction with an object of any conductivity from that of a perfect conductor, to that of a real metal, to that of low or zero conductivity
4. Frequency-dependent constitutive parameters for modeling most materials
    i. Lossy dielectrics
    ii. Magnetic materials
    iii. Unconventional materials, including anisotropic plasmas and magnetized ferrites
5. Any type of response, including far fields derived from near fields, such as
    i. Scattered fields
    ii. Antenna patterns
    iii. Radar cross-section (RCS)
    iv. Surface response
    v. Currents, power density
    vi. Penetration/interior coupling

Although the FDTD method is a very convenient numerical approximation approach, it also has a number of drawbacks as mentioned below:

1. Since the FDTD method requires a grid to be formed over the entire computational domain, the restrictions on the cell size (with respect to the

wavelength and the problem geometry), may lead to a large number of cells, resulting long run times.

2. Objects with long, thin features, (like wires) are difficult to model in the FDTD method because of the excessively large computational domain required.
3. The computational domain in the FDTD method is usually modeled in Cartesian coordinates, where the cell surfaces are parallel to the coordinate axes. The modeling of curved surfaces introduces a source of error, known as staircasing.
4. The electromagnetic field components are evaluated directly everywhere in the computational domain, which is basically the near-field region of the scatterer or the antenna. If RCS or radiation pattern calculations are required, the far-field expressions of the electromagnetic field must be available. For this purpose, near-to-far field transformations are used based on integrations over a Huygens' box enclosing the scatterer/radiator.

1.2 Objective of the Thesis

The main aim of this thesis is to study the interaction of electromagnetic waves with human body parts. In particular, power dissipation in human head due to a closely spaced radiator (simulating a mobile phone device) is studied. For this purpose, an FDTD code has been developed to calculate specific absorption rates in a dielectric lossy object simulating the human head. To achieve this goal:

- A 3D FDTD MATLAB code has been designed including a PML mesh truncation and human head model.
- In order to verify the accuracy of the method, the numerical results are compared with analytical solutions in some test cases.
- The tissue distribution in a human head is extensively studied to model the object successfully.

1.3 Outline of the Thesis

Following the Introduction chapter, theoretical details of the FDTD method are explained in Chapter 2. Also, 1D, 2D and 3D wave propagation and scattering examples are given. In Chapter 2, the formulations do not include any absorbing boundary conditions. For the realistic simulation of open region problems, absorbing boundary conditions must be employed, which is explained in Chapter 3. In Chapter 4, a human head model is developed. The input impedance and field distribution of a wire antenna are calculated and compared with analytical results for the purpose of code verification in Chapter 5. Finally, in Chapter 6 for the problem of human head/mobile phone radiator interaction, SAR values within the human head are calculated via the FDTD code and results are discussed.

The main subject of the thesis work is to discuss the interaction of human head tissues with the electromagnetic radiation from a cellular phone located close to the head. Several results related to this problem have been reported in the literature [16-22]. In these papers, the researchers investigated the same problem with different head and/or phone models. As a result of different modeling approaches, the results differ in magnitude. However, there is not much difference in the order of magnitude of the result. The results obtained in this thesis are also of the same order of magnitude with the results in the literature.

CHAPTER 2

DESCRIPTION OF THE FINITE DIFFERENCE TIME DOMAIN (FDTD) APPROXIMATION

The FDTD approach is an approximate iterative solution method for Maxwell's curl equations in time domain. The partial differential operators are discretized by using the finite difference expressions, leading to a coupled system of difference equations, which are solved in a leap-frog manner; that is, the electric field intensity vector is solved at a given instant in time, followed by the calculation of the magnetic field intensity vector at the next instant in time. In addition, the electric and magnetic fields are specified at neighboring points leading to a staggered pattern in space.

When Maxwell's curl equations are examined, it can be seen that the time derivative of the E field is related to the curl of the H field. This implies that the temporal rate of change in the E field (i.e. the time derivative) is related to the spatial rate of change of the H field (i.e. the spatial derivatives in the curl operator). A finite difference approximation of the time derivative leads to a difference expression where the new value of the E field (which is still unknown) is expressed in terms of the old value of the E field (which has already been calculated) and the spatial partial derivatives of the old value of the H field (which has also been calculated). This picture illustrates the fact that the field components are calculated iteratively by marching-on in time. Because of the apparent symmetry in Maxwell's curl equations, a similar iterative scheme is applicable for the equation which relates the time derivative of the H-field to the curl of the E-field.

The spatial derivatives may also be approximated in terms of finite differences such that the E and H field points are staggered in space, leading to the final form of equations used in FDTD applications.

In order to use the FDTD approach, a computational domain must be established. This domain is a rectangular prism filled with points (known as a grid or mesh) where E or H fields are specified. If there are material bodies, the constitutive relations must also be specified at each point. Typically, the material may be either air (taken as free space), conducting metal (taken as perfect electrical conductors (PEC)), or insulators. There are of course other possibilities where the objects are modeled as anisotropic or bianisotropic materials.

Once the computational domain is established, sources creating the electromagnetic field must be specified. The source can be an impinging plane wave, a current on a wire, or an electric field between metal bodies (basically a voltage difference between two metal objects), depending on the type of excitation to be modeled.

Since the E and H fields are determined iteratively, the output of the simulation is usually the E or H field at the grid points within the computational domain. Additional quantities, such as the power density, far-field expressions, etc. can be evaluated in terms of the already calculated field expressions.

2.1 Maxwell's Equations in Time Domain

All electromagnetic phenomena can be expressed in terms of a coupled system of partial differential equations known as Maxwell's equations as given below for the source-free case:

$$\nabla x\overline{E} = -\frac{\partial \overline{B}}{\partial t} \tag{2.1a}$$

$$\nabla x\overline{H} = \frac{\partial \overline{D}}{\partial t} + \overline{J}_C \tag{2.1b}$$

$$\nabla .\overline{D} = 0 \tag{2.1c}$$

$$\nabla .\overline{B} = 0 \tag{2.1d}$$

In linear, isotropic, non-dispersive materials (i.e. materials having field-independent, direction-independent and frequency-independent electric and magnetic properties)

$$\overline{D} = \in \overline{E} \ , \ \overline{B} = \mu \overline{H} \text{ and } \overline{J_c} = \sigma \overline{E} \tag{2.2}$$

(2.1a) and (2.1b) can be rewritten as:

$$\frac{\partial \overline{H}}{\partial t} = -\frac{1}{\mu} \nabla x\overline{E} \tag{2.3a}$$

$$\frac{\partial \overline{E}}{\partial t} = \frac{1}{\varepsilon} \nabla x\overline{H} - \frac{\sigma}{\varepsilon} \overline{E} \tag{2.3b}$$

The open form of (2.3a) is

$$\frac{\partial}{\partial t}(H_x \hat{a}_x + H_y \hat{a}_y + H_z \hat{a}_z) = -\frac{1}{\mu} \begin{vmatrix} \hat{a}_x & \hat{a}_y & \hat{a}_z \\ \frac{\partial}{\partial x} & \frac{\partial}{\partial y} & \frac{\partial}{\partial z} \\ E_x & E_y & E_z \end{vmatrix} \tag{2.4}$$

A similar equation can be defined for (2.3b) as well, and after equating x, y and z components on both sides of (2.3a) and (2.3b), the following scalar equation set is obtained

$$\begin{aligned}
\frac{\partial H_x}{\partial t} &= \frac{1}{\mu}\left(\frac{\partial E_y}{\partial z} - \frac{\partial E_z}{\partial y}\right) \\
\frac{\partial H_y}{\partial t} &= \frac{1}{\mu}\left(\frac{\partial E_z}{\partial x} - \frac{\partial E_x}{\partial z}\right) \\
\frac{\partial H_z}{\partial t} &= \frac{1}{\mu}\left(\frac{\partial E_x}{\partial y} - \frac{\partial E_y}{\partial x}\right) \\
\frac{\partial E_x}{\partial t} &= \frac{1}{\varepsilon}\left(\frac{\partial H_z}{\partial y} - \frac{\partial H_y}{\partial z} - \sigma E_x\right) \\
\frac{\partial E_y}{\partial t} &= \frac{1}{\varepsilon}\left(\frac{\partial H_x}{\partial z} - \frac{\partial H_z}{\partial x} - \sigma E_y\right) \\
\frac{\partial E_z}{\partial t} &= \frac{1}{\varepsilon}\left(\frac{\partial H_y}{\partial x} - \frac{\partial H_x}{\partial y} - \sigma E_z\right)
\end{aligned} \tag{2.5}$$

2.1.1 Maxwell's Curl Equations in Two Dimensions

If the field components are functions of x and y only, and independent of z, the equations are simplified as given below.

2.1.1.a Transverse Magnetic (TM) Mode

In Transverse Magnetic mode, H_z must be zero. The nonzero components are E_z, H_x and H_y.

$$\frac{\partial H_x}{\partial t} = \frac{1}{\mu}\left(-\frac{\partial E_z}{\partial y}\right)$$
$$\frac{\partial H_y}{\partial t} = \frac{1}{\mu}\left(\frac{\partial E_z}{\partial x}\right) \qquad (2.6a)$$
$$\frac{\partial E_z}{\partial t} = \frac{1}{\varepsilon}\left(\frac{\partial H_y}{\partial x} - \frac{\partial H_x}{\partial y} - \sigma E_z\right)$$

2.1.1.b Transverse Electric (TE) Mode

In contrast to the TM mode, the non-zero field components in this case are H_z, E_x and E_y.

$$\frac{\partial E_x}{\partial t} = \frac{1}{\varepsilon}\left(\frac{\partial H_z}{\partial y} - \sigma E_x\right)$$
$$\frac{\partial E_y}{\partial t} = \frac{1}{\varepsilon}\left(-\frac{\partial H_z}{\partial x} - \sigma E_y\right) \qquad (2.6b)$$
$$\frac{\partial H_z}{\partial t} = \frac{1}{\mu}\left(\frac{\partial E_x}{\partial y} - \frac{\partial E_y}{\partial x}\right)$$

2.1.2 Maxwell's Curl Equations for the 1D Case

Consider the case where neither the electromagnetic field intensity vectors nor the modeled geometry has any variation in the y and z directions. Therefore, all field partial derivatives with respect to z and y are equal to zero. In TM mode, equations reduce to,

$$\frac{\partial H_y}{\partial t} = \frac{1}{\mu}\left(\frac{\partial E_z}{\partial x}\right)$$
$$\frac{\partial E_z}{\partial t} = \frac{1}{\varepsilon}\left(\frac{\partial H_y}{\partial x} - \sigma E_z\right) \qquad (2.7a)$$

Again assuming that all partial derivatives with respect to y and z are equal zero, the two-dimensional TE mode of Maxwell's equations in rectangular coordinates reduces to,

$$\frac{\partial H_z}{\partial t} = \frac{1}{\mu}\left(-\frac{\partial E_y}{\partial x}\right)$$
$$\frac{\partial E_y}{\partial t} = \frac{1}{\varepsilon}\left(-\frac{\partial H_z}{\partial x} - \sigma E_y\right) \tag{2.7b}$$

2.2 Approximation of Derivatives by Finite Differences

In the FDTD approach, Maxwell's equations are discretized by approximating the spatio-temporal derivatives by their finite difference counterparts. To this end, it is essential to develop the finite difference expressions starting from the definition of the derivative of a function $f(x)$ at point x_0 , as given below

$$\frac{d}{dx} f(x)\bigg|_{x=x_0} = \lim_{h\to 0} \frac{f(x_0+h) - f(x_0)}{h} \tag{2.8}$$

In the finite difference method, the derivatives are approximated locally by finite difference quotients $(h > 0)$ instead of a limit.

For example,

$$\frac{d}{dx} f(x)\bigg|_{x=x_0} \approx \frac{f(x_0+h) - f(x_0)}{h} \tag{2.8a}$$

is called the forward difference expression. The geometric interpretation of this approximation is illustrated in Fig. 2.1.

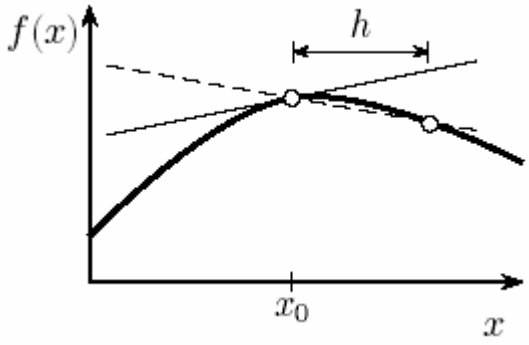

Figure 2.1: Forward Difference of a Function

Similarly, the backward difference operation is defined as

$$\frac{d}{dx} f(x)\Big|_{x=x_0} \approx \frac{f(x_0) - f(x_0 - h)}{h} \tag{2.8b}$$

The geometric interpretation of (2.8b) is shown in Fig. 2.2.

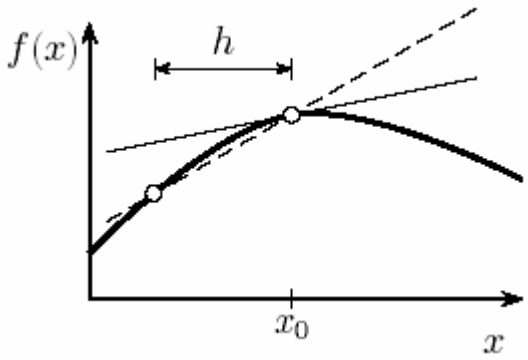

Figure 2.2: Backward Difference of a Function

From Figs. 2.1 and 2.2 it can be concluded that the backward or forward difference expressions fail to approximate the differentiation operation accurately. If the average of the forward and backward differences is evaluated, we get the central difference formula

$$\left.\frac{d}{dx}f(x)\right|_{x=x_0} \approx \frac{1}{2}\left[\frac{f(x_0+h)-f(x_0)}{h}+\frac{f(x_0)-f(x_0-h)}{h}\right]$$

$$=\frac{f(x_0+h)-f(x_0-h)}{2h} \tag{2.9}$$

The geometric meaning of (2.9) is also explained in Fig. 2.3.

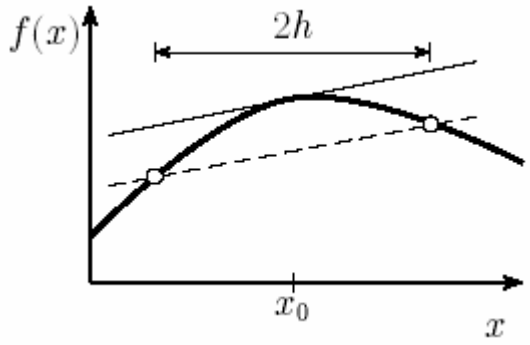

Figure 2.3: Central Difference of a Function

It is also possible to approximate higher order derivatives by finite difference expressions. For example, the central difference approximation of the second derivative of a function is,

$$\left.\frac{d^2}{dx^2}f(x)\right|_{x=x_0} \approx \left[\frac{\dfrac{f(x_0+h)-f(x_0)}{h}-\dfrac{f(x_0)-f(x_0-h)}{h}}{h}\right]$$

$$=\left[\frac{f(x_0+h)-2f(x_0)+f(x_0-h)}{h^2}\right] \tag{2.10}$$

2.3 The Yee Algorithm

K. S. Yee introduced a finite difference approximation for the coupled system of differential equations given by (2.5) [5]. In his formulation, he used central difference expressions for both space and time derivatives. Throughout this thesis, a special notation introduced by Yee (involving super and subscripts) will be employed, as explained below.

2.3.1 Yee's Notation

(i, j, k) : Integers

$(\Delta x, \Delta y, \Delta z)$: Space increments in the x, y and z directions.

$$A^{n}{}_{i,j,k} = A(i\Delta x,\, j\Delta y, k\Delta z, n\Delta t)$$

where A denotes any field component.

Consider the first expression in (2.5)

$$\frac{\partial H_x}{\partial t} = \frac{1}{\mu}\left(\frac{\partial E_y}{\partial z} - \frac{\partial E_z}{\partial y}\right)$$

$$\frac{H_x\Big|^{n+1}_{i,j+\frac{1}{2},k+\frac{1}{2}} - H_x\Big|^{n}_{i,j+\frac{1}{2},k+\frac{1}{2}}}{\Delta t} = \frac{1}{\mu_{i,j+\frac{1}{2},k+\frac{1}{2}}}\left[\frac{E_y\Big|^{n+\frac{1}{2}}_{i,j+\frac{1}{2},k+1} - E_y\Big|^{n+\frac{1}{2}}_{i,j+\frac{1}{2},k}}{\Delta z} - \frac{E_z\Big|^{n+\frac{1}{2}}_{i,j+1,k+\frac{1}{2}} - E_z\Big|^{n+\frac{1}{2}}_{i,j,k+\frac{1}{2}}}{\Delta y}\right] \tag{2.11}$$

Multiplying both sides by Δt and isolating $H_x\Big|^{n+1}_{i,j+\frac{1}{2},k+\frac{1}{2}}$ on the left hand side yields:

$$H_x\Big|^{n+1}_{i,j+\frac{1}{2},k+\frac{1}{2}} =$$

$$H_x\Big|^{n}_{i,j+\frac{1}{2},k+\frac{1}{2}} + \frac{\Delta t}{\mu_{i,j+\frac{1}{2},k+\frac{1}{2}}}\left[\frac{E_y\Big|^{n+\frac{1}{2}}_{i,j+\frac{1}{2},k+1} - E_y\Big|^{n+\frac{1}{2}}_{i,j+\frac{1}{2},k}}{\Delta z} - \frac{E_z\Big|^{n+\frac{1}{2}}_{i,j+1,k+\frac{1}{2}} - E_z\Big|^{n+\frac{1}{2}}_{i,j,k+\frac{1}{2}}}{\Delta y}\right] \qquad (2.12)$$

So, H_x at the time step n+1 is evaluated in terms of previously calculated values of H_x (at the time step n), E_y and E_z (at time step n+$\frac{1}{2}$).

In a similar manner, we can derive the finite-difference expressions for

$H_y\Big|^{n+1}_{i+\frac{1}{2},j,k+\frac{1}{2}}$ and $H_z\Big|^{n+1}_{i+\frac{1}{2},j+\frac{1}{2},k}$

from (2.5).

Now consider the fourth expression in (2.5):

$$\frac{\partial E_x}{\partial t} = \frac{1}{\varepsilon}\left(\frac{\partial H_z}{\partial y} - \frac{\partial H_y}{\partial z} - \sigma E_x\right)$$

which is approximated as follows

$$\frac{E_x\Big|^{n+\frac{1}{2}}_{i+\frac{1}{2},j,k} - E_x\Big|^{n-\frac{1}{2}}_{i+\frac{1}{2},j,k}}{\Delta t} = \frac{1}{\varepsilon_{i+\frac{1}{2},j,k}}$$
$$\left[\begin{array}{l} \dfrac{H_z\Big|^{n}_{i+\frac{1}{2},j+\frac{1}{2},k} - H_z\Big|^{n}_{i+\frac{1}{2},j-\frac{1}{2},k}}{\Delta y} - \dfrac{H_y\Big|^{n}_{i+\frac{1}{2},j,k+\frac{1}{2}} - H_y\Big|^{n}_{i+\frac{1}{2},j,k-\frac{1}{2}}}{\Delta z} \\ -\sigma\big|_{i+\frac{1}{2},j,k}\, E_x\Big|^{n}_{i+\frac{1}{2},j,k} \end{array}\right] \tag{2.13}$$

Since E_x is not specified at n-th time step, it can be approximated as follows.

$$E_x\Big|^{n}_{i+\frac{1}{2},j,k} = \frac{E_x\Big|^{n+\frac{1}{2}}_{i+\frac{1}{2},j,k} + E_x\Big|^{n-\frac{1}{2}}_{i+\frac{1}{2},j,k}}{2} \tag{2.14}$$

which is called a semi-implicit approximation, implying that $E_x\Big|^{n}_{i+\frac{1}{2},j,k}$ is the temporal average of $E_x\Big|^{n+\frac{1}{2}}_{i+\frac{1}{2},j,k}$ and $E_x\Big|^{n-\frac{1}{2}}_{i+\frac{1}{2},j,k}$.

If this expression is substituted into the right hand side of (2.13), the following expression is obtained

$$E_x\Big|^{n+\frac{1}{2}}_{i+\frac{1}{2},j,k}\left(\frac{1}{\Delta t}+\frac{\sigma}{2\varepsilon}\right) = E_x\Big|^{n-\frac{1}{2}}_{i+\frac{1}{2},j,k}\left(\frac{1}{\Delta t}-\frac{\sigma}{2\varepsilon}\right) +$$
$$\frac{1}{\varepsilon}\left(\frac{H_z\Big|^{n}_{i+\frac{1}{2},j+\frac{1}{2},k} - H_z\Big|^{n}_{i+\frac{1}{2},j-\frac{1}{2},k}}{\Delta y} - \frac{H_y\Big|^{n}_{i+\frac{1}{2},j,k+\frac{1}{2}} - H_y\Big|^{n}_{i+\frac{1}{2},j,k-\frac{1}{2}}}{\Delta z}\right) \tag{2.15}$$

If the term $E_x\Big|^{n+\frac{1}{2}}_{i+\frac{1}{2},j,k}$ is isolated on the left hand side, the following iterative expression is found

$$E_x\Big|^{n+\frac{1}{2}}_{i+\frac{1}{2},j,k} = E_x\Big|^{n-\frac{1}{2}}_{i+\frac{1}{2},j,k}\left(\frac{2\varepsilon-\sigma\Delta t}{2\varepsilon+\sigma\Delta t}\right)+$$
$$\left(\frac{2\Delta t}{2\varepsilon+\sigma\Delta t}\right)\left(\frac{H_z\Big|^{n}_{i+\frac{1}{2},j+\frac{1}{2},k}-H_z\Big|^{n}_{i+\frac{1}{2},j-\frac{1}{2},k}}{\Delta y}-\frac{H_y\Big|^{n}_{i+\frac{1}{2},j,k+\frac{1}{2}}-H_y\Big|^{n}_{i+\frac{1}{2},j,k-\frac{1}{2}}}{\Delta z}\right) \qquad (2.16)$$

In a similar manner, finite-difference expressions for $E_y\Big|^{n+\frac{1}{2}}_{i,j+\frac{1}{2},k}$ and $E_z\Big|^{n+\frac{1}{2}}_{i,j,k+\frac{1}{2}}$ can be derived from (2.5).

2.4 Yee Cell

In the previous section, the finite difference approximation of the field variations has been given. The most remarkable aspect of these expressions is that the field components are staggered in space and time. That is, the electric and magnetic field components are defined at different space points and different time instants. This property is shown in Fig. 2.4, which is an illustration of the Yee cell representing the building block of the FDTD grid. As shown below, every E component is surrounded by four circulating H components, and every H component is surrounded by four circulating E components.

If the front face is considered in particular, H_x is expressed in terms of the E_z values at the left and right and E_y values above and below.

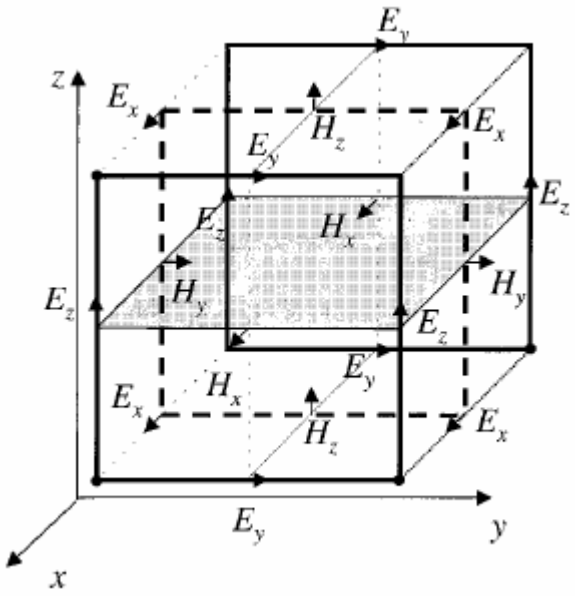

Figure 2.4: Yee Cell

The six spatio-temporal difference equations relating the field components are given below

$$\frac{H_x\Big|^{n+1}_{i,j+\frac{1}{2},k+\frac{1}{2}} - H_x\Big|^{n}_{i,j+\frac{1}{2},k+\frac{1}{2}}}{\Delta t} = \frac{1}{\mu_{i,j+\frac{1}{2},k+\frac{1}{2}}}\left[\frac{E_y\Big|^{n+\frac{1}{2}}_{i,j+\frac{1}{2},k+1} - E_y\Big|^{n+\frac{1}{2}}_{i,j+\frac{1}{2},k}}{\Delta z} - \frac{E_z\Big|^{n+\frac{1}{2}}_{i,j+1,k+\frac{1}{2}} - E_z\Big|^{n+\frac{1}{2}}_{i,j,k+\frac{1}{2}}}{\Delta y}\right] \tag{2.17a}$$

$$\frac{H_y\Big|^{n+1}_{i+\frac{1}{2},j,k+\frac{1}{2}} - H_y\Big|^{n}_{i+\frac{1}{2},j,k+\frac{1}{2}}}{\Delta t} = \frac{1}{\mu_{i+\frac{1}{2},j,k+\frac{1}{2}}}\left[\frac{E_z\Big|^{n+\frac{1}{2}}_{i+1,j,k+\frac{1}{2}} - E_z\Big|^{n+\frac{1}{2}}_{i,j,k+\frac{1}{2}}}{\Delta x} - \frac{E_x\Big|^{n+\frac{1}{2}}_{i+\frac{1}{2},j,k+1} - E_x\Big|^{n+\frac{1}{2}}_{i+\frac{1}{2},j,k}}{\Delta z}\right] \tag{2.17b}$$

$$\frac{H_z\Big|^{n+1}_{i+\frac{1}{2},j+\frac{1}{2},k} - H_z\Big|^{n}_{i+\frac{1}{2},j+\frac{1}{2},k}}{\Delta t} = \frac{1}{\mu_{i+\frac{1}{2},j+\frac{1}{2},k}}\left[\frac{E_x\Big|^{n+\frac{1}{2}}_{i+\frac{1}{2},j+1,k} - E_x\Big|^{n+\frac{1}{2}}_{i+\frac{1}{2},j,k}}{\Delta y} - \frac{E_y\Big|^{n+\frac{1}{2}}_{i+1,j+\frac{1}{2},k} - E_y\Big|^{n+\frac{1}{2}}_{i,j+\frac{1}{2},k}}{\Delta x}\right] \tag{2.17c}$$

$$\frac{E_x\Big|^{n+\frac{1}{2}}_{i+\frac{1}{2},j,k} - E_x\Big|^{n-\frac{1}{2}}_{i+\frac{1}{2},j,k}}{\Delta t} = \frac{1}{\varepsilon_{i+\frac{1}{2},j,k}}\left[\frac{H_z\Big|^{n}_{i+\frac{1}{2},j+\frac{1}{2},k} - H_z\Big|^{n}_{i+\frac{1}{2},j-\frac{1}{2},k}}{\Delta y} - \frac{H_y\Big|^{n}_{i+\frac{1}{2},j,k+\frac{1}{2}} - H_y\Big|^{n}_{i+\frac{1}{2},j,k-\frac{1}{2}}}{\Delta z} - \sigma\Big|_{i+\frac{1}{2},j,k} E_x\Big|^{n}_{i+\frac{1}{2},j,k}\right] \tag{2.17d}$$

$$\frac{E_y\Big|^{n+\frac{1}{2}}_{i,j+\frac{1}{2},k} - E_y\Big|^{n-\frac{1}{2}}_{i,j+\frac{1}{2},k}}{\Delta t} = \frac{1}{\varepsilon_{i,j+\frac{1}{2},k}}\left[\frac{H_x\Big|^{n}_{i,j+\frac{1}{2},k+\frac{1}{2}} - H_x\Big|^{n}_{i,j+\frac{1}{2},k-\frac{1}{2}}}{\Delta z} - \frac{H_z\Big|^{n}_{i+\frac{1}{2},j+\frac{1}{2},k} - H_z\Big|^{n}_{i-\frac{1}{2},j+\frac{1}{2},k}}{\Delta x} - \sigma\Big|_{i,j+\frac{1}{2},k} E_y\Big|^{n}_{i,j+\frac{1}{2},k}\right] \tag{2.17e}$$

$$\frac{E_z\Big|^{n+\frac{1}{2}}_{i,j,k+\frac{1}{2}} - E_z\Big|^{n-\frac{1}{2}}_{i,j,k+\frac{1}{2}}}{\Delta t} = \frac{1}{\varepsilon_{i,j,k+\frac{1}{2}}}\left[\frac{H_y\Big|^{n}_{i+\frac{1}{2},j,k+\frac{1}{2}} - H_y\Big|^{n}_{i-\frac{1}{2},j,k+\frac{1}{2}}}{\Delta x} - \frac{H_x\Big|^{n}_{i,j+\frac{1}{2},k+\frac{1}{2}} - H_x\Big|^{n}_{i,j-\frac{1}{2},k+\frac{1}{2}}}{\Delta y} - \sigma\Big|_{i,j,k+\frac{1}{2}} E_z\Big|^{n}_{i,j,k+\frac{1}{2}}\right] \tag{2.17f}$$

The equations (2.17a-2.17f) are the FDTD counterparts for the source-free 3D Maxwell's curl equations.

2.5 Stability Condition for the FDTD Equations

As explained in the previous section, the spatio-temporal discretization of Maxwell's curl equations leads to a coupled system of difference equations. The solution of this equation system can be obtained iteratively starting from an initial condition. It is well known that if the solution stays bounded for all time instants, the difference equation system is said to be stable. The stability condition, which gives the relationship between space and time increments, is given in [6, 7]. For 3D applications, it is given by

$$\Delta t \leq \frac{1}{c\sqrt{\frac{1}{(\Delta x)^2}+\frac{1}{(\Delta y)^2}+\frac{1}{(\Delta z)^2}}} \tag{2.18}$$

Let $\Delta x = \Delta y = \Delta z = \Delta$, then (2.18) reduces to

$$\Delta t \leq \frac{\Delta}{c\sqrt{3}} \tag{2.19}$$

In many applications, (2.19) is replaced by the expression

$$\Delta t = \frac{\Delta}{2c} \tag{2.20}$$

2.6 Introductory Examples

In this section, some examples will be given to validate the FDTD code in 1D, 2D and 3D cases. The main emphasis will be to demonstrate the simulation of electromagnetic wave propagation for some simple applications.

2.6.1 1D Wave Propagation

Simulation of one dimensional wave propagation is the simplest possible example in FDTD approach. As a first example, it is shown below in Fig. 2.5 that a Gaussian pulse is excited in the middle portion of the grid and propagates in both directions without any attenuation due to the fact that the medium is lossless.

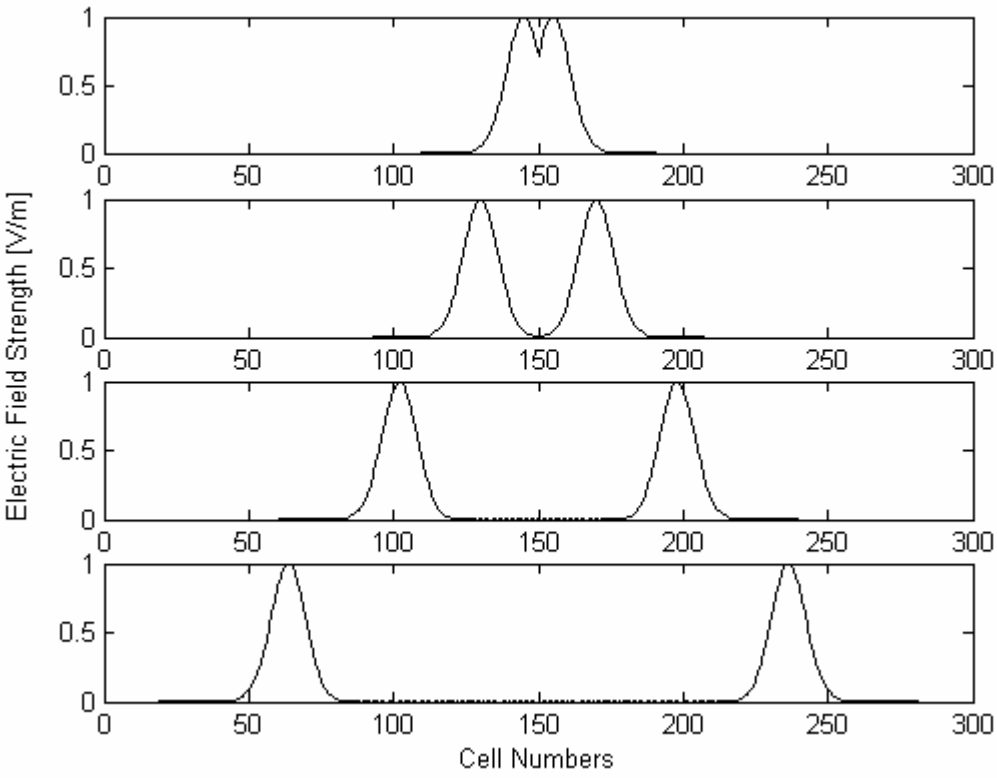

Figure 2.5: Propagation of a Gaussian Pulse in Free Space

If the medium is not homogeneous, several reflections will occur, as demonstrated in Fig. 2.6.

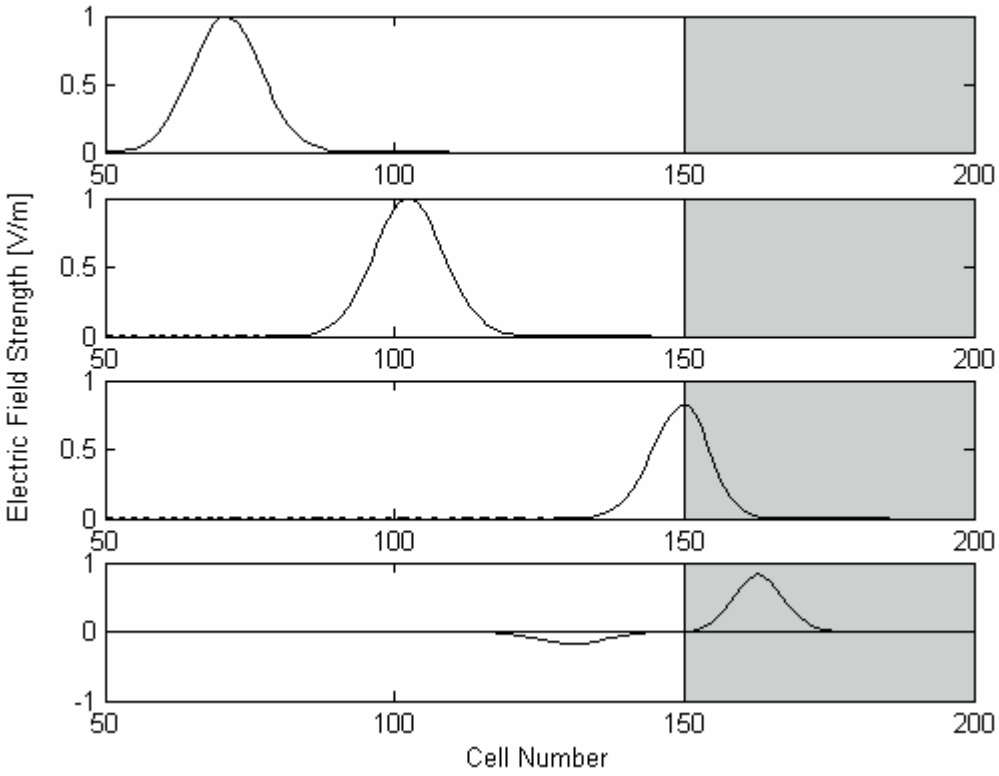

Figure 2.6: Propagation of a Gaussian Pulse through the Interface of Two Different Media

The gray area represents a medium having a relative dielectric constant equal to 2. As a result, a reflection will occur at the interface, because of the discontinuity in the dielectric constant.

The reflection coefficient for a normally-incident plane wave is given by [8]

$$\Gamma_{ref} = \frac{E_{ref}}{E_{inc}} = \frac{\eta_2 - \eta_1}{\eta_2 + \eta_1} \tag{2.21}$$

The intrinsic impedance expression is given by

$$\eta = \sqrt{\frac{\mu}{\varepsilon_0 \varepsilon_r}} \tag{2.22}$$

where ε_r is the relative dielectric constant.

It is obvious that for a lossless medium, the impedance is proportional to $\frac{1}{\sqrt{\varepsilon_r}}$. In the example above, gray area has a relative dielectric constant 2. So, the reflection coefficient is:

$$\Gamma = \frac{\frac{1}{\sqrt{2}} - 1}{\frac{1}{\sqrt{2}} + 1} = -0.1716$$

The peak value of the reflected wave is -0.1719 for the example given above. The relative error between numerical and analytical solution is

$$E = \frac{|0.1716 - 0.1719|}{0.1716} = 0.17\%$$

2.6.2 2D Wave Propagation

In order to demonstrate the FDTD code developed in this thesis, the example in Yee's 1966 paper is duplicated. In this example, there is no dependence on z coordinate. The source is chosen as a plane wave (a sinusoidal pulse) which propagates towards an obstacle with a square cross-section. Below, in Fig. 2.7, the incident plane wave is plotted at different time instants in the absence of the obstacle, which is essentially a pulse propagating in x direction.

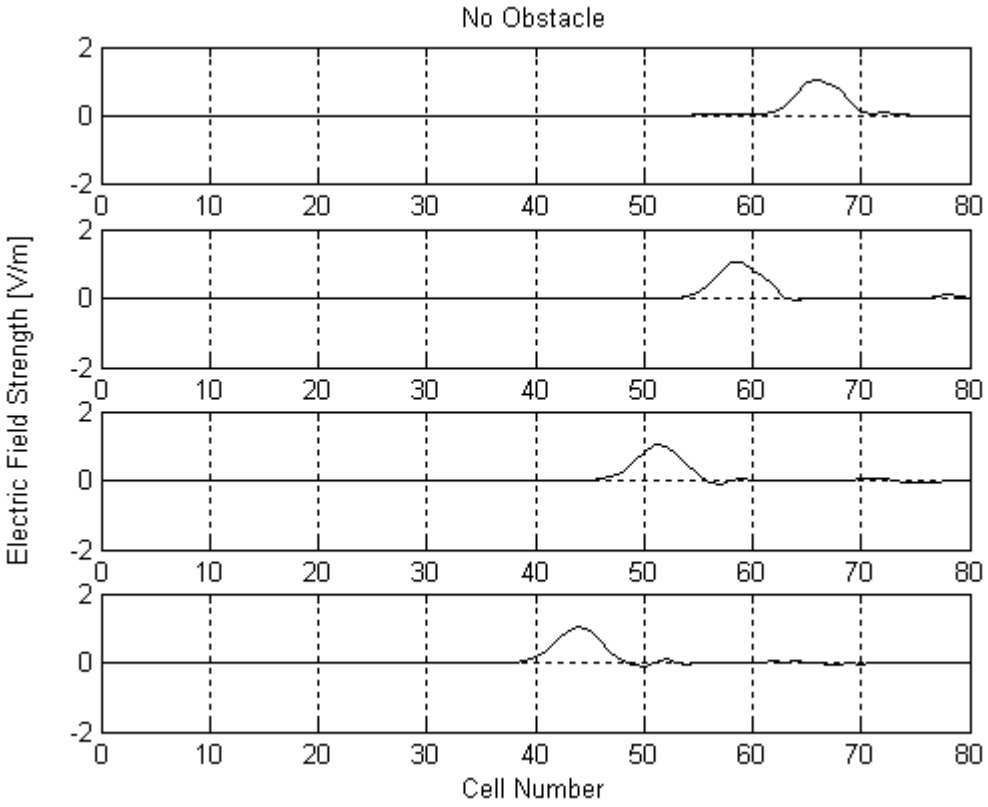

Figure 2.7: Snapshots of the Sinusoidal Pulse at Time Steps 15, 30, 45, 60

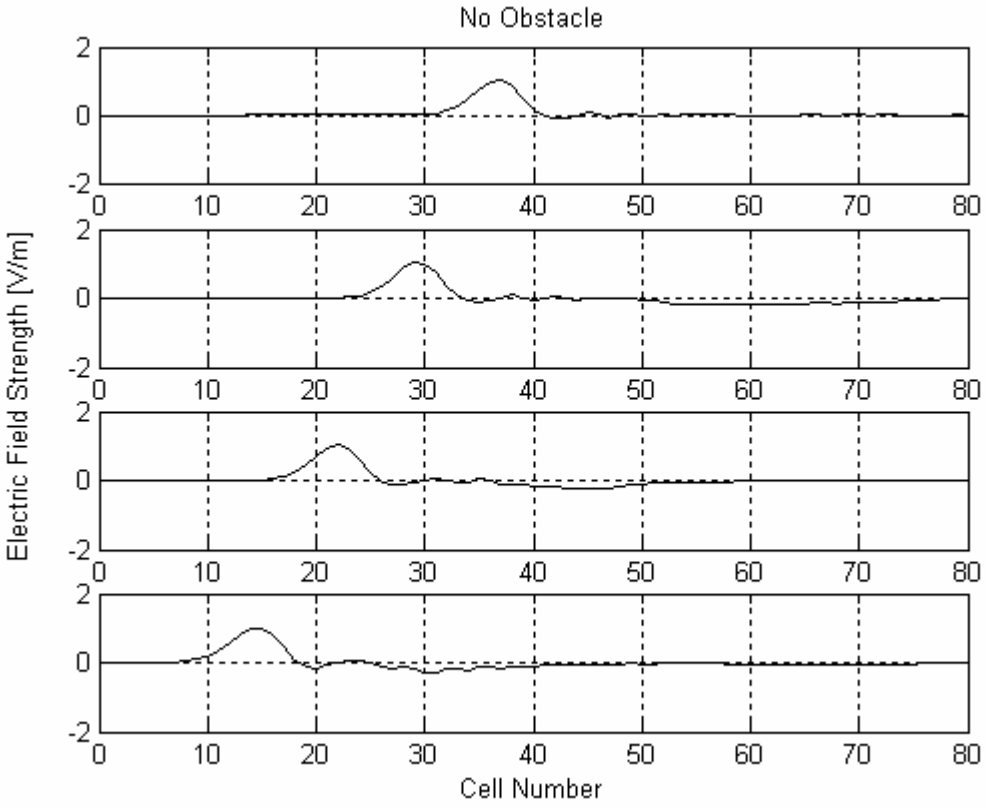

Figure 2.8: Snapshots of the Sinusoidal Pulse at Time Steps 75, 90, 105, 120

In Yee's paper, a PEC obstacle with a square cross-section is located in the middle of the computational domain to simulate the reflection phenomenon. The snapshots are shown in Figs. 2.9 and 2.10. The remaining figures (Figs. 2.11-2.12) are gray-scale images of the field variation. The artifacts in these figures are due to numerical reflections from the boundary.

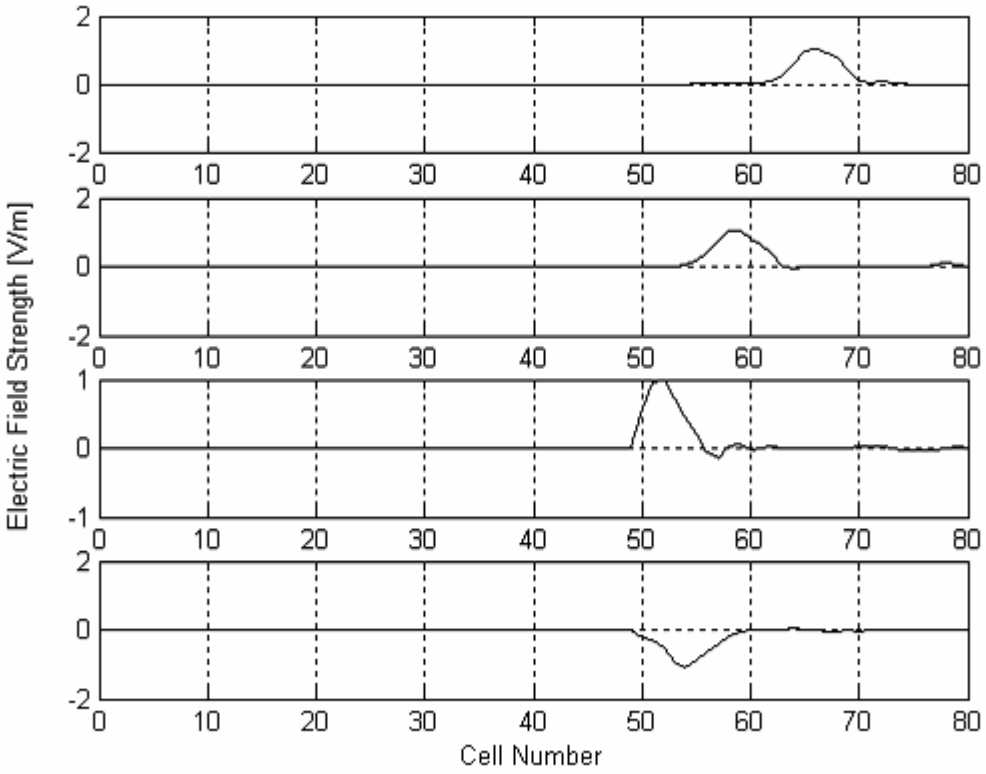

Figure 2.9: Snapshots of the Sinusoidal Pulse at Time Steps 15 ,30 ,45 ,60 (in the presence of the obstacle)

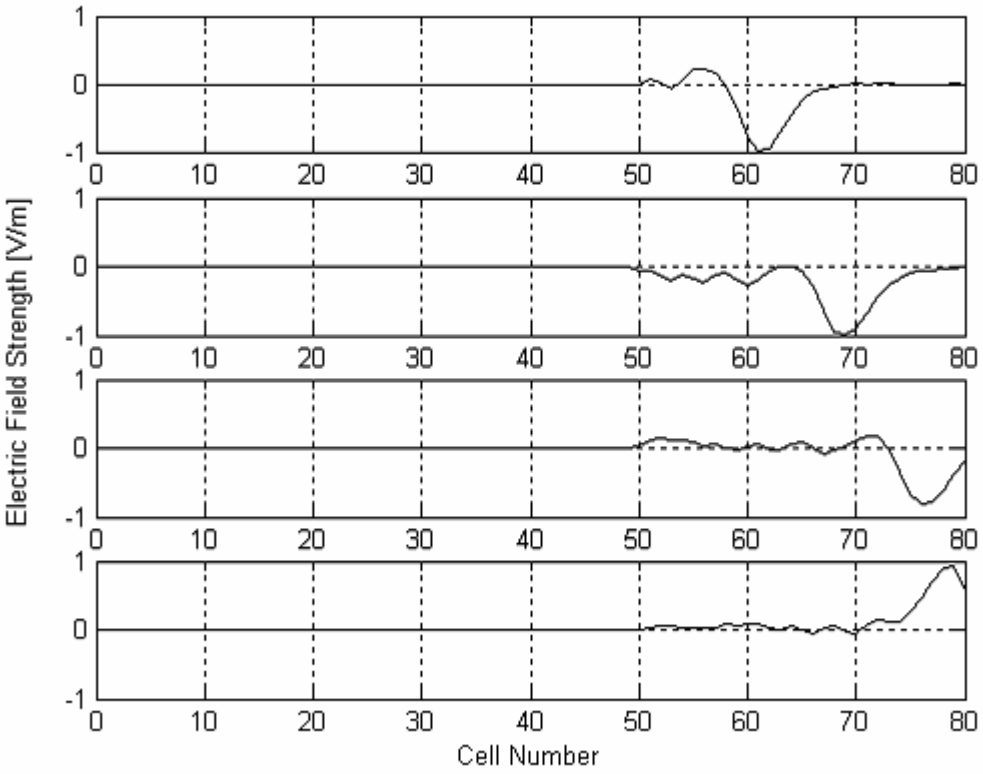

Figure 2.10: Snapshots of the Sinusoidal Pulse at Time Steps 75, 90, 105, 120 (in the presence of the obstacle)

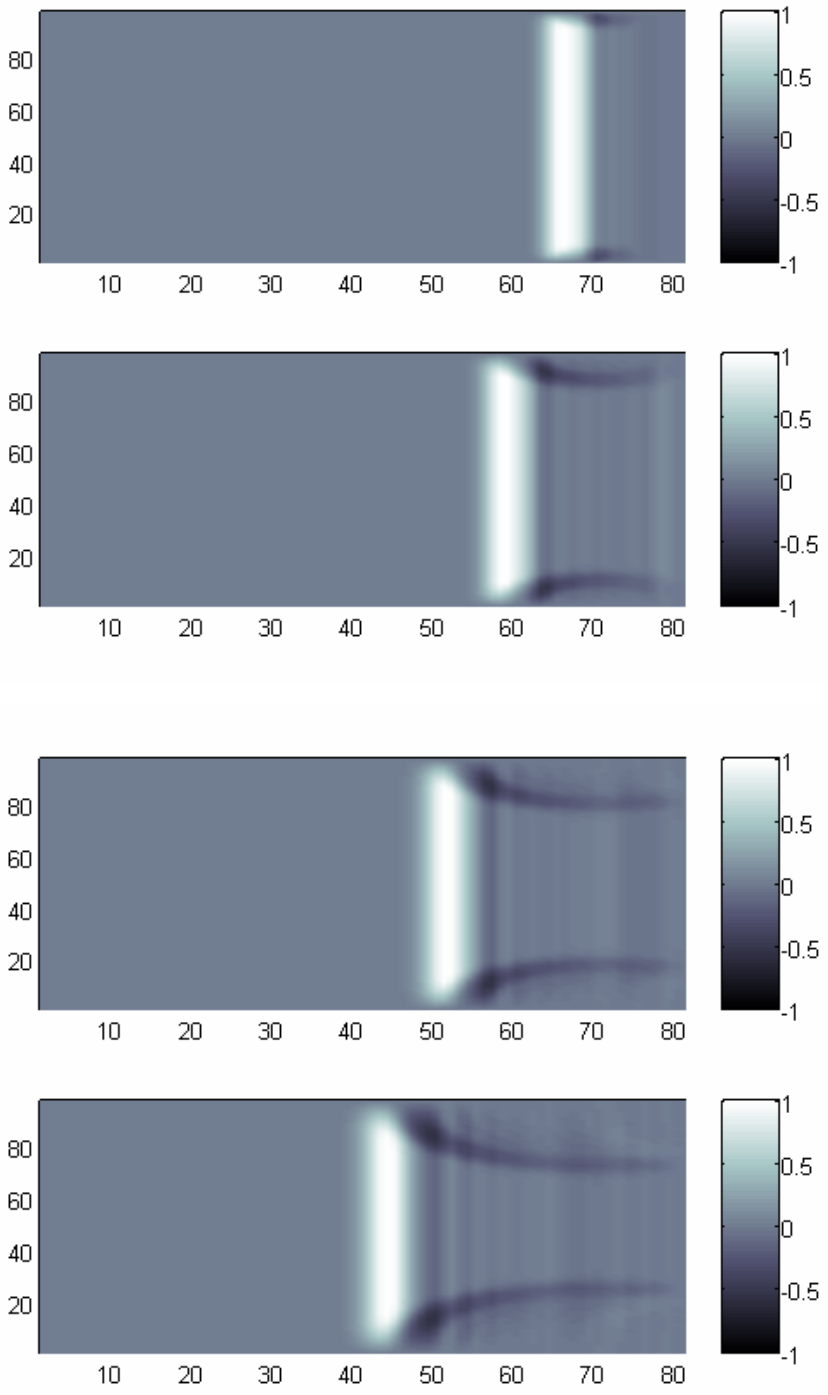

Figure 2.11: Gray-scale Snapshots of a Plane Wave Propagating towards Left (No Obstacle)

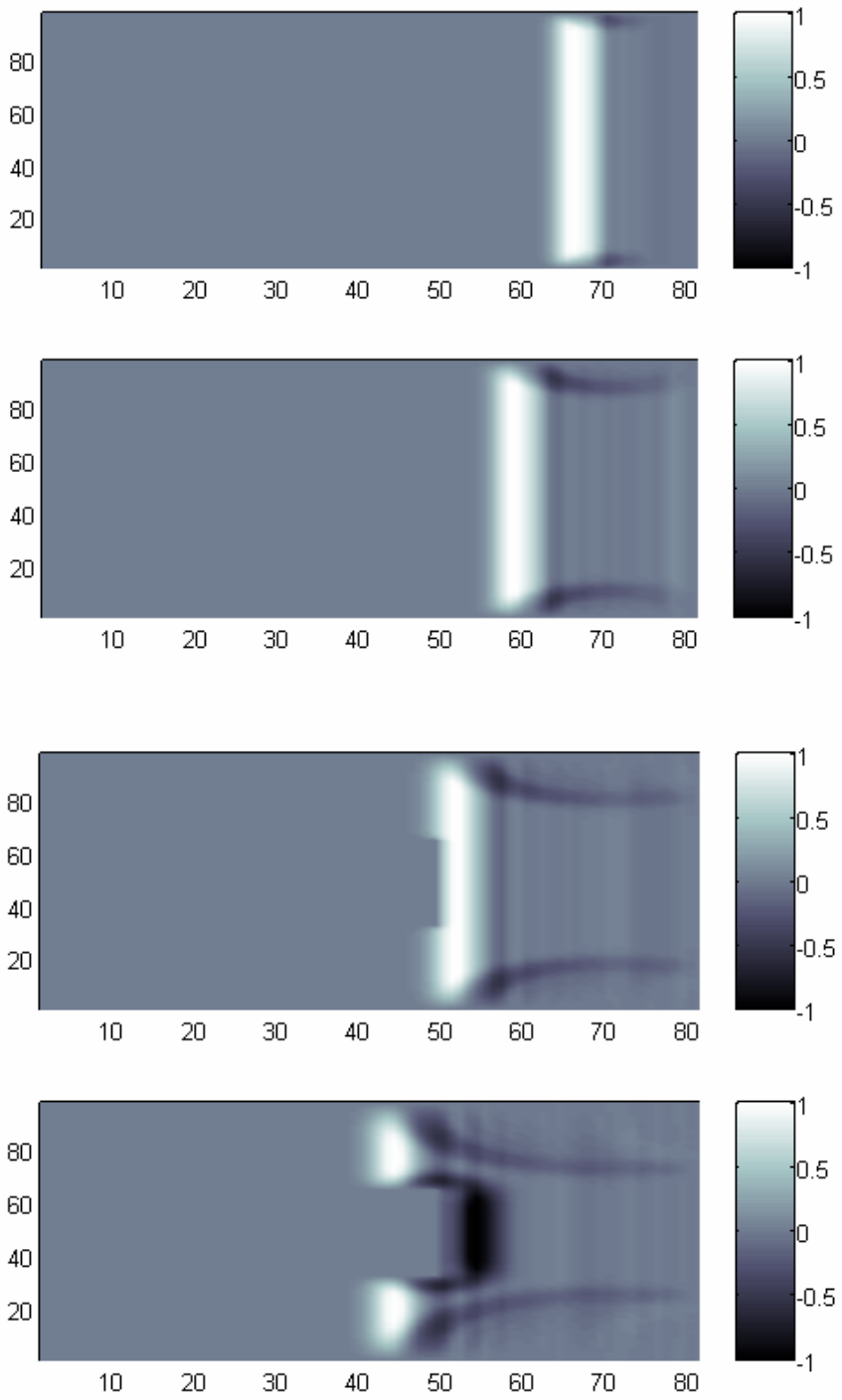

Figure 2.12: Gray-scale Snapshots of a Plane Wave Propagating towards Left (in the presence of the obstacle)

2.6.3 3D Wave Propagation

Although 3D FDTD simulation is similar to the 2D case, it is geometrically and computationally more involved. The increased complexity in 3D is due to the fact that all vector field components ($E_x, E_y, E_z, H_x, H_y, H_z$) are non-zero in general and each component is a function of three coordinate variables.

Below, in Figs. 2.13-2.19, snapshots of the radiation from a dipole antenna are given in terms of graphs of the E_z component on xy plane. The computational domain is a cube with side length 138 cm. ($\Delta x = \Delta y = \Delta z = 3$ cm, which means that there are $46x46x46 = 97336$ Yee cells in the grid. The time increment satisfies $\Delta t = \frac{\Delta x}{2c_0}$) The dipole antenna is modeled as a 72 cm center-fed thin wire antenna extending in z direction, located symmetrically at the center of the computational domain. The excitation is applied at the center as an impressed E_z field (i.e. gap voltage) whose temporal variation is a continuous sinusoid with frequency 900 MHz.

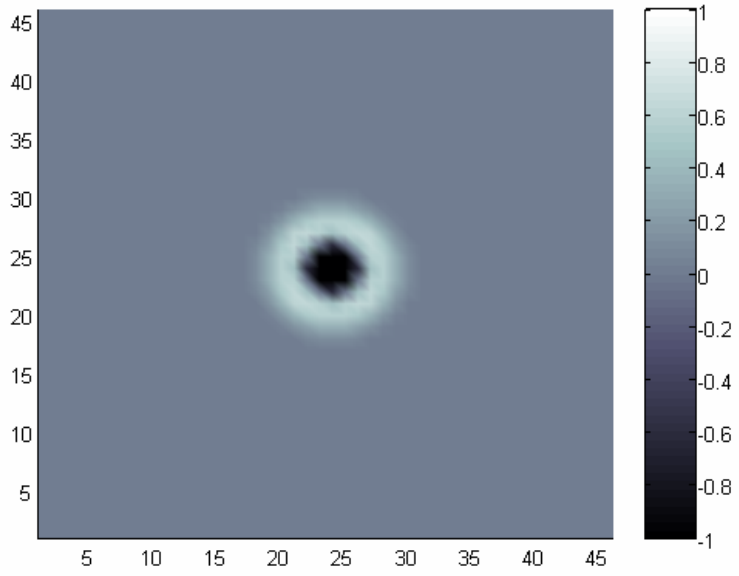

Figure 2.13: Gray-scale snapshot of E_z over xy plane ($t = 15\,\Delta t$)

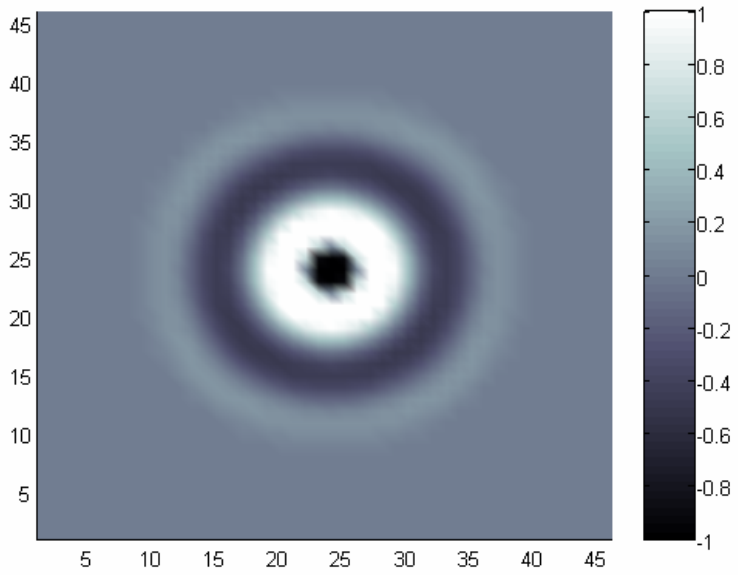

Figure 2.14: Gray-scale snapshot of E_z over xy plane ($t = 30\,\Delta t$)

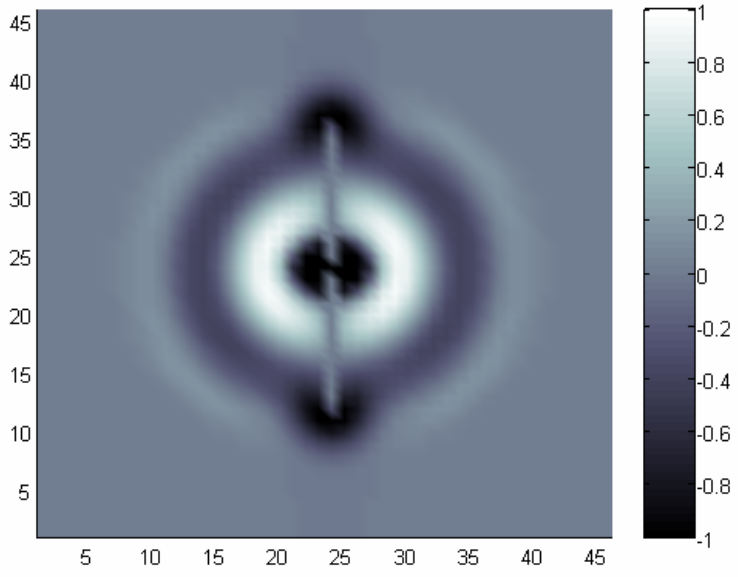

Figure 2.15: Gray-scale snapshot of E_z over xz plane ($t = 30\,\Delta t$)

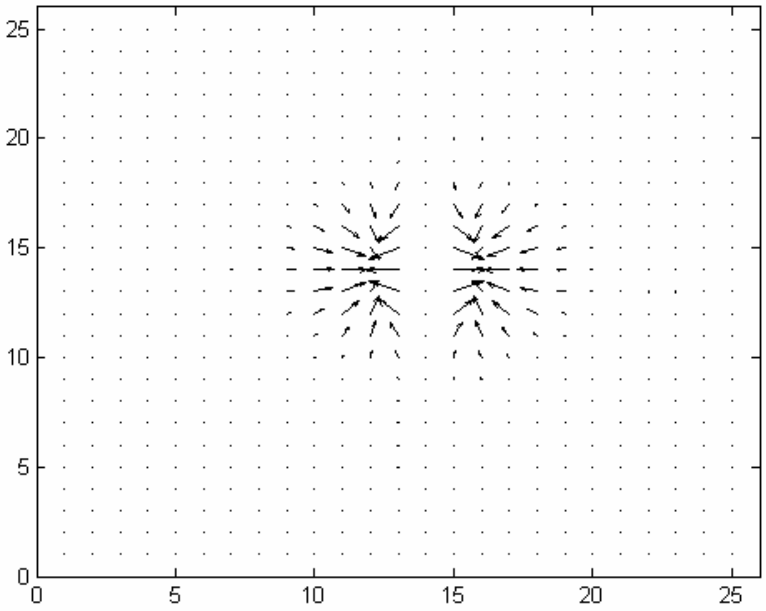

Figure 2.16: Gradient map snapshot of E_z over xz plane ($t = 30\,\Delta t$)

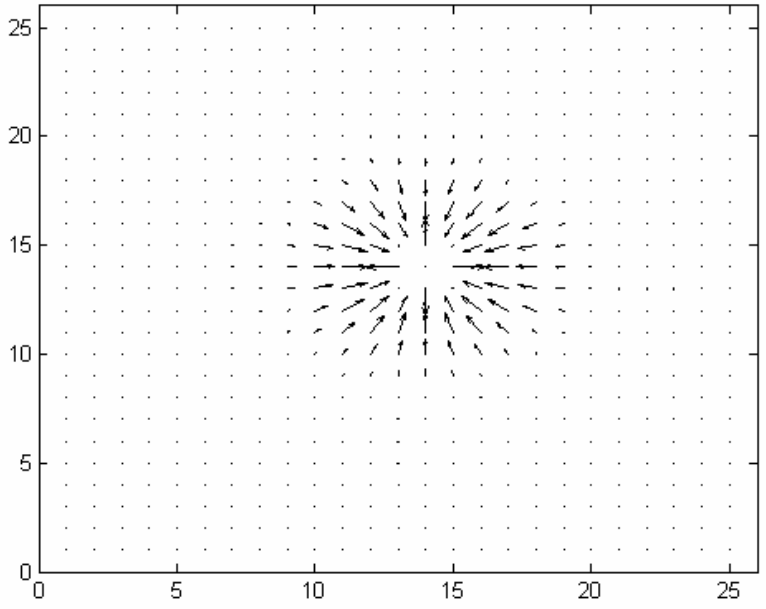

Figure 2.17: Gradient map snapshot of E_z over xy plane ($t = 30\,\Delta t$)

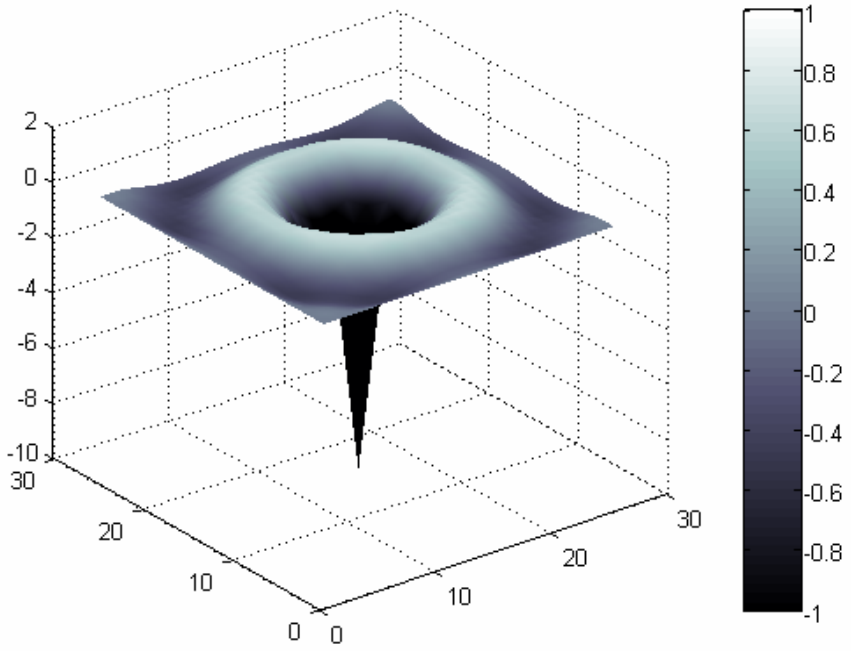

Figure 2.18: Gray-scale snapshot of E_z over xy plane ($t = 40\,\Delta t$)

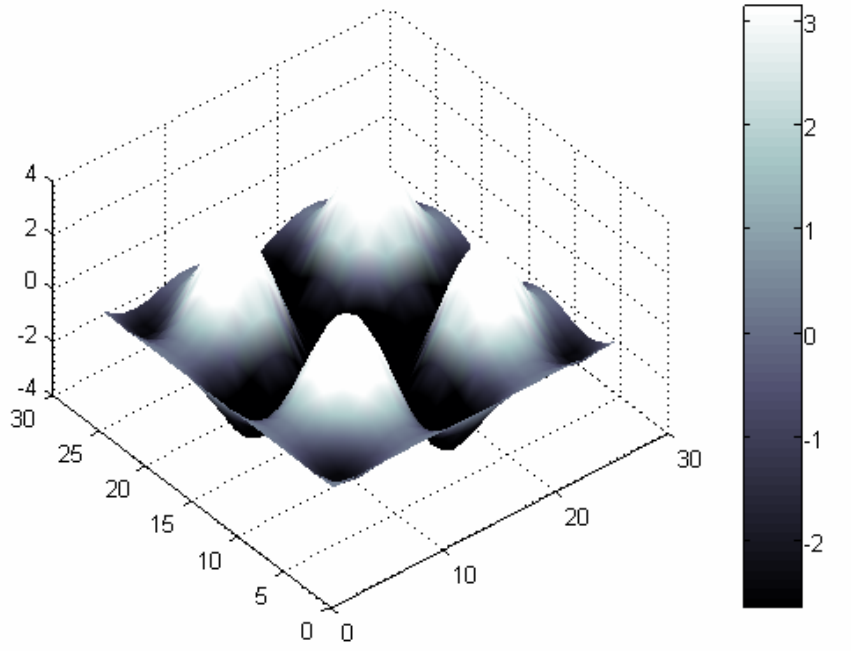

Figure 2.19: Gray-scale snapshot of E_z over xy plane ($t = 100\,\Delta t$)

In Figs. 2.18 and 2.19, it is observed that when the wave reaches the outer boundary, it is reflected back to the inner region, which means that the boundary behaves like a PEC wall. In reality, the antenna is located in free space which extends to infinity. In order to simulate this case, the outer walls must be transparent. This difficulty can be resolved by defining Absorbing Boundary Conditions (ABCs) over the outer boundary. Another possibility is the Perfectly Matched Layer (PML) approach, which is essentially a material layer which absorbs electromagnetic waves (with arbitrary frequency and direction) without any reflection. In this thesis, a special PML has been implemented as will be explained in the next chapter.

CHAPTER 3

PML GRID TRUNCATION IN FDTD

In most of the initial/boundary value problems of electromagnetics, the physical domain is unbounded. In numerical simulations, the computational domain must be bounded because of the necessity to handle a finite number of unknowns. For this purpose, either Absorbing Boundary Conditions (ABCs) are used at the outer boundary, or an absorbing layer is used. These approaches aim to simulate a reflectionless grid truncation as successfully as possible. The PML approach, introduced by Berenger, is an effective method to absorb plane electromagnetic waves without any reflection.

3.1 The Perfectly Matched Layer (PML) Concept

In FDTD simulations, the electromagnetic wave initiated by a source distribution propagates outward and reaches the outer boundary of the computational domain. If no conditions are imposed at this boundary, reflections will occur and the numerical results will fail to simulate the correct behavior of electromagnetic wave propagation. Ideally, the outer boundary must be transparent in order to simulate outgoing waves. ABCs and several types of PMLs are effective solutions in this direction [4, 9, 10].

In Berenger's PML method [4], which is the first successful attempt to use absorbers in mesh truncation, each component of the electromagnetic field vectors is split into two parts. In Cartesian coordinates, the six components yield 12 subcomponents. There are

advantages and disadvantages of Berenger's technique. The prominent advantage of this method is that it is a perfectly matched layer. So, reflection is independent of angle of incidence. Regardless of angle and polarization, very small amount of reflection occurs. However, the equations in Berenger's formulation are non-Maxwellian, that is, they do not satisfy Maxwell's equations.

In December 1996, S. Gedney presented a new PML absorbing material composed of a uniaxial anisotropic material for the truncation of FDTD lattices [9]. Unlike Berenger's technique, the uniaxial PML medium presented by Gedney is Maxwellian. Also, FDTD implementation of the uniaxial PML medium is stable, effective and more computationally efficient than the others.

3.2 Theoretical Basis of the PML Concept

Consider a time-harmonic, arbitrarily polarized plane wave propagating in an isotropic medium, whose H_y component is given in (3.1).

$$H^{inc} = H_o e^{-j\beta^i{}_x x - j\beta^i{}_z z} \tag{3.1}$$

The wave is incident on a material half-space described as a uniaxial anisotropic medium. The interface between two media is the $z = 0$ plane. In the plane wave space the curl equations are expressed as

$$\begin{aligned} \beta^a x E &= \omega \mu_0 \mu_r \overline{\overline{\mu}} H \\ \beta^a x H &= -\omega \varepsilon_0 \varepsilon_r \overline{\overline{\varepsilon}} E \end{aligned} \tag{3.2}$$

In equations above,

$$\beta^a = \hat{x}\beta^i{}_x + \hat{z}\beta^a{}_z \tag{3.3}$$

and ε_r expresses relative permittivity while μ_r refers to relative permeability.

The parameters are defined as

$$\begin{aligned} \overline{\overline{\varepsilon}} &= \begin{bmatrix} a & 0 & 0 \\ 0 & a & 0 \\ 0 & 0 & b \end{bmatrix} \\ \overline{\overline{\mu}} &= \begin{bmatrix} c & 0 & 0 \\ 0 & c & 0 \\ 0 & 0 & d \end{bmatrix} \end{aligned} \tag{3.4}$$

The entries ε_{xx} and ε_{yy} , as well as μ_{xx} and μ_{yy} are equal, implying that the medium is symmetric about the z axis.

The wave equation is derived from the coupled curl equations (3.2) as

$$\beta^a x \overline{\overline{\varepsilon}}^{-1} \beta^a x H + k^2 \overline{\overline{\mu}} H = 0 \tag{3.5}$$

where $k^2 = \omega^2 \mu_0 \mu_r \varepsilon_0 \varepsilon_r$.

First, assume the presence of a TE_y incident wave. In the isotropic space the fields are expressed as a superposition of the incident and reflected fields as

$$H_1 = \hat{y} H_0 (1 + \Gamma e^{2j\beta^i{}_z z}) e^{-j\beta^i{}_x x - j\beta^i{}_z z} \tag{3.6a}$$

$$E_1 = \left[\hat{x} \frac{\beta^i{}_z}{\omega\varepsilon} (1 - \Gamma e^{2j\beta^i{}_z z}) - \hat{z} \frac{\beta^i{}_x}{\omega\varepsilon} (1 + \Gamma e^{2j\beta^i{}_z z}) \right] H_0 e^{-j\beta^i{}_x x - j\beta^i{}_z z} \tag{3.6b}$$

The wave transmitted into the anisotropic half-space will also be TE_y as given below

$$H_2 = \hat{y} H_0 \mathrm{T} e^{-j\beta^i{}_x x - j\beta^a{}_z z} \tag{3.7a}$$

$$E_2 = \left[\hat{x} \frac{\beta^a{}_z a^{-1}}{\omega\varepsilon} - \hat{z} \frac{\beta^i{}_x b^{-1}}{\omega\varepsilon} \right] H_0 \mathrm{T} e^{-j\beta^i{}_x x - j\beta^a{}_z z} \tag{3.7b}$$

From the equations (3.6a), (3.6b), (3.7a) and (3.7b), by enforcing the continuity of the tangential fields across the boundary, it is found that:

$$\begin{aligned} \Gamma &= \frac{\beta^i{}_z - \beta^a{}_z a^{-1}}{\beta^i{}_z + \beta^a{}_z a^{-1}} \\ \mathrm{T} &= 1 + \Gamma = \frac{2\beta^i{}_z}{\beta^i{}_z + \beta^a{}_z a^{-1}} \end{aligned} \tag{3.8}$$

The main objective is to make the reflection coefficient zero for all angles of incidence.

$$\Gamma = 0$$

$$\beta^i{}_z = \beta^a{}_z a^{-1} \tag{3.9}$$

From the wave equation, dispersion relationship can be derived for TE_y polarization.

$$\beta^i{}_z{}^2 = k^2 c a^{-1} - \beta^i{}_x{}^2 b^{-1} a^{-1} \tag{3.10}$$

where $\beta^i{}_z{}^2 = k^2 - \beta^i{}_x{}^2$.

If $c = a$ and $b = a^{-1}$, dispersion equation is valid.

All the derivations given above can be repeated for TM_y polarization as well. In conclusion, it is found that, if $a = c = b^{-1} = d^{-1}$, the plane wave will be transmitted into the uniaxial medium without reflection. This result is completely independent of the angle of incidence, polarization and frequency.

While implementing the PML medium, conductivity of the anisotropic half-space must be high enough to attenuate the incoming wave within a finite longitudinal distance. Since the computational domain must be finite in extent, there will be a PEC (or PMC) termination. If the wave is attenuated to a negligible level before it hits the outer boundary, the reflection may be negligible. For this reason, the PML termination is effective if the uniaxial medium is highly lossy. However, there is an upper limit of the conductivity value of the uniaxial medium, because of restrictions related to stability.

For the lossy uniaxial medium, constitutive parameters can be selected as given in (3.11-3.12). In the limit as σ tends to zero, the uniaxial medium reduces to an isotropic space.

$$\overline{\overline{\varepsilon}} = \begin{bmatrix} 1+\dfrac{\sigma}{j\omega\varepsilon_0} & 0 & 0 \\ 0 & 1+\dfrac{\sigma}{j\omega\varepsilon_0} & 0 \\ 0 & 0 & \dfrac{1}{1+\dfrac{\sigma}{j\omega\varepsilon_0}} \end{bmatrix} \tag{3.11}$$

$$\overline{\overline{\mu}} = \begin{bmatrix} 1+\dfrac{\sigma}{j\omega\varepsilon_0} & 0 & 0 \\ 0 & 1+\dfrac{\sigma}{j\omega\varepsilon_0} & 0 \\ 0 & 0 & \dfrac{1}{1+\dfrac{\sigma}{j\omega\varepsilon_0}} \end{bmatrix} \tag{3.12}$$

3.3 FDTD Equations in the PML Region

In the uniaxial medium, Ampere's law is expressed in matrix form as

$$\begin{bmatrix} \frac{\partial H_z}{\partial y} - \frac{\partial H_y}{\partial z} \\ \frac{\partial H_x}{\partial z} - \frac{\partial H_z}{\partial x} \\ \frac{\partial H_y}{\partial x} - \frac{\partial H_x}{\partial y} \end{bmatrix} = j\omega\varepsilon_0\varepsilon_r \begin{bmatrix} 1+\frac{\sigma}{j\omega\varepsilon_0} & 0 & 0 \\ 0 & 1+\frac{\sigma}{j\omega\varepsilon_0} & 0 \\ 0 & 0 & \frac{1}{1+\frac{\sigma}{j\omega\varepsilon_0}} \end{bmatrix} \begin{bmatrix} E_x \\ E_y \\ E_z \end{bmatrix} \tag{3.13}$$

The first two rows represent lossy isotropic media. Subsequently, FDTD equations follow as

$$E_x\Big|^{n+\frac{1}{2}}_{i+\frac{1}{2},j,k} = E_x\Big|^{n-\frac{1}{2}}_{i+\frac{1}{2},j,k}\left(\frac{2\varepsilon_0-\sigma\Delta t}{2\varepsilon_0+\sigma\Delta t}\right)+ \left(\frac{\frac{2\Delta t}{\varepsilon_r}}{2\varepsilon_0+\sigma\Delta t}\right)\left(\frac{H_z\Big|^n_{i+\frac{1}{2},j+\frac{1}{2},k} - H_z\Big|^n_{i+\frac{1}{2},j-\frac{1}{2},k}}{\Delta y} - \frac{H_y\Big|^n_{i+\frac{1}{2},j,k+\frac{1}{2}} - H_y\Big|^n_{i+\frac{1}{2},j,k-\frac{1}{2}}}{\Delta z}\right) \tag{3.14}$$

Nevertheless, it is not very easy to write the equation for E_z in this manner. Because, frequency dependence of ε_{zz} is nonlinear. E_z updates are obtained in the following manner

$$D_z = \frac{\varepsilon_0\varepsilon_r}{1+\frac{\sigma}{j\omega\varepsilon_0}}E_z \tag{3.15}$$

$$D_z\Big|^{n+\frac{1}{2}}_{i,j,k+\frac{1}{2}} = D_z\Big|^{n-\frac{1}{2}}_{i,j,k+\frac{1}{2}} + \Delta t \left(\frac{H_y\Big|^{n}_{i+\frac{1}{2},j,k+\frac{1}{2}} - H_y\Big|^{n}_{i-\frac{1}{2},j,k+\frac{1}{2}}}{\Delta x} - \frac{H_x\Big|^{n}_{i,j+\frac{1}{2},k+\frac{1}{2}} - H_x\Big|^{n}_{i,j-\frac{1}{2},k+\frac{1}{2}}}{\Delta y} \right) \tag{3.16}$$

From (3.15), E_z can be calculated in terms of D_z.

$$j\omega D_z + \frac{\sigma}{\varepsilon_0} D_z = j\omega \varepsilon_0 \varepsilon_r E_z \tag{3.17}$$

$$E_z\Big|^{n+\frac{1}{2}}_{i,j,k+\frac{1}{2}} = E_z\Big|^{n-\frac{1}{2}}_{i,j,k+\frac{1}{2}} + \frac{1}{\varepsilon_0 \varepsilon_r} \left(D_z\Big|^{n+\frac{1}{2}}_{i,j,k+\frac{1}{2}} \left(1 + \frac{\sigma \Delta t}{2\varepsilon_0} \right) - D_z\Big|^{n-\frac{1}{2}}_{i,j,k+\frac{1}{2}} \left(1 - \frac{\sigma \Delta t}{2\varepsilon_0} \right) \right) \tag{3.18}$$

The previous analysis only considers the case of a wave incident on a single planar interface. However, for 3D problems the FDTD lattice must be terminated by a PML region on all six sides of the computational domain, as shown in Fig. 3.1.

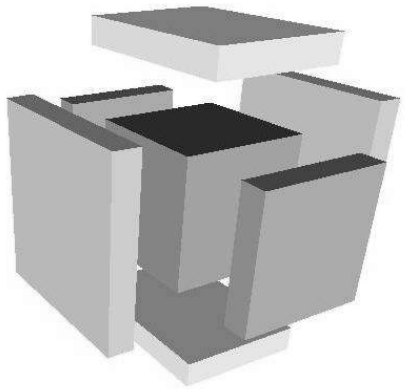

Figure 3.1: An FDTD Lattice terminated by six Perfectly Matched Layers

An ambiguity occurs in the corner regions where there is more than one normal interface boundary. Within these regions, a more generalized constitutive relationship is necessary. In this region, Maxwell's curl equations are expressed as

$$\begin{aligned} \nabla x\bar{H} &= j\omega\varepsilon_0\varepsilon_r \overline{\overline{\varepsilon}}\bar{E} \\ \nabla x\bar{E} &= -j\omega\mu_0 \overline{\overline{\mu}}\bar{H} \end{aligned} \tag{3.19}$$

where

$$\overline{\overline{\varepsilon}} = \overline{\overline{\mu}} = \begin{bmatrix} \frac{s_y s_z}{s_x} & 0 & 0 \\ 0 & \frac{s_x s_z}{s_y} & 0 \\ 0 & 0 & \frac{s_x s_y}{s_z} \end{bmatrix} \tag{3.20}$$

and

$$\begin{aligned} s_x &= 1 + \frac{\sigma_x}{j\omega\varepsilon_0} \\ s_y &= 1 + \frac{\sigma_y}{j\omega\varepsilon_0} \\ s_z &= 1 + \frac{\sigma_z}{j\omega\varepsilon_0} \end{aligned} \tag{3.21}$$

In the computational space, σ_i is equal to zero (outside the PML regions). In the corner regions, the time-dependent fields are updated by using techniques similar to the previously given derivations. As an example, consider the update of E_z

$$D_z = \varepsilon_0\varepsilon_r \frac{s_x}{s_z} E_z \tag{3.22}$$

Then, from (3.19) and (3.20)

$$\frac{\partial}{\partial x}H_y - \frac{\partial}{\partial y}H_x = j\omega s_y D_z = j\omega D_z + \frac{\sigma_y}{\varepsilon_0}D_z \tag{3.23}$$

Transforming this into the time domain, D_z is then updated using a standard explicit FDTD expression similar to (3.14).

From (3.22), E_z can be found as

$$E_z\Big|^{n+\frac{1}{2}} = E_z\Big|^{n-\frac{1}{2}} \frac{1-\frac{\sigma_x \Delta t}{2\varepsilon_0}}{1+\frac{\sigma_x \Delta t}{2\varepsilon_0}} + \frac{1}{\left(1+\frac{\sigma_x \Delta t}{2\varepsilon_0}\right)\varepsilon_0 \varepsilon_r} \tag{3.24}$$
$$\left(D_z\Big|^{n+\frac{1}{2}}\left(1+\frac{\sigma_z \Delta t}{2\varepsilon_0}\right) - D_z\Big|^{n-\frac{1}{2}}\left(1-\frac{\sigma_z \Delta t}{2\varepsilon_0}\right)\right)$$

The other field component updates can be obtained by using similar approaches.

3.4 Simulation of the PML-FDTD Formulation

In the simulation, there is a dipole antenna radiating at 900 MHz. The antenna and computational domain dimensions are identical to those in the example given in Sec. 2.6. The only difference is that the chosen cell size is λ/50. The PML extent is 10 cells. E_z component is observed one cell away (within free space) from the PML interface, in order to discriminate the reflected field (which is expected to be negligibly small). In FDTD applications, in order to avoid abrupt oscillations and overshoots, the sinusoidal excitation is multiplied by an envelope function which starts from zero initially and tends to unity in a uniform way in early time, as shown in Fig. 3.2. In Fig. 3.3, the results of the FDTD code under different conditions are given. In order to illustrate how the E_z component tends to sinusoidal steady-state, the peak values are shown in Fig. 3.4.

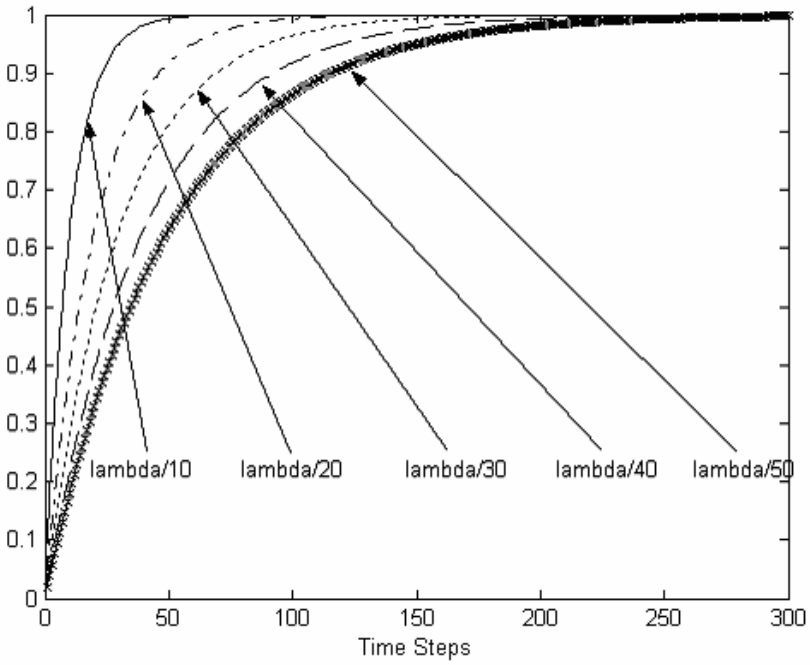

Figure 3.2: Envelope Function Variation with respect to Cell Size

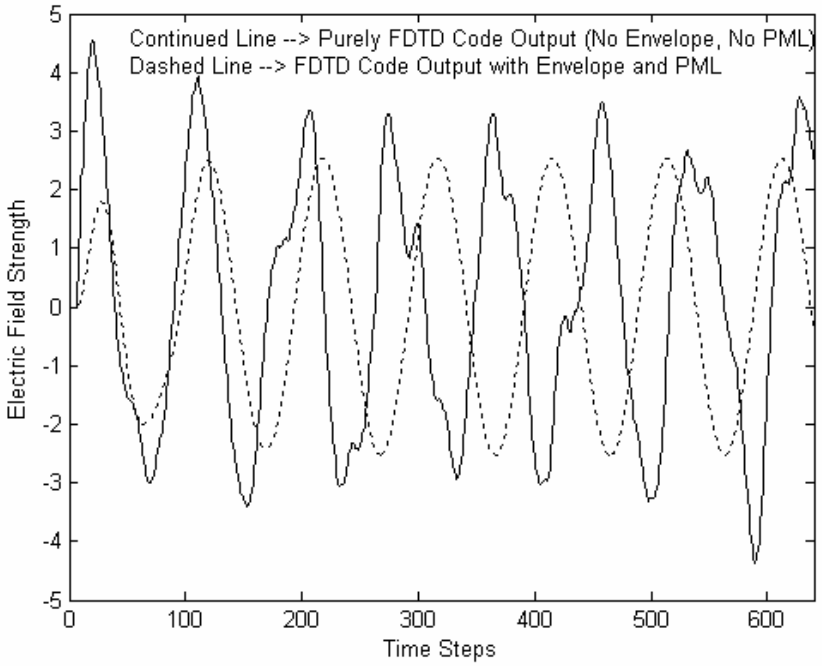

Figure 3.3: Results Generated by the FDTD code with and without PML termination

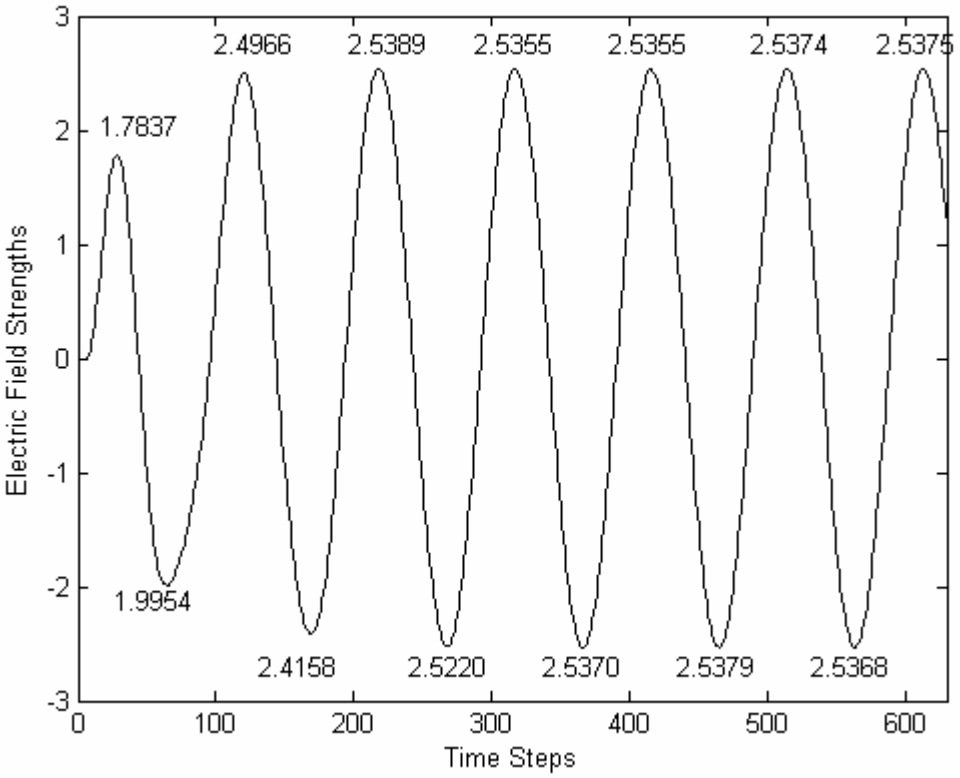

Figure 3.4: Maximum and Minimum Values of the E_z component

3.5 The Conductivity Variation within the PML Region

The conductivity variation within the PML must be chosen such that the magnitudes of the field components decrease to a negligible value before they reach the outermost termination. A constant conductivity may cause numerical reflections, because of the sudden jump at the interface. It is preferable that the conductivity starts from zero at the interface and increase in the longitudinal direction as given below [9]

$$\sigma(z) = \frac{\sigma_{\max} |z - z_o|^m}{d^m} \tag{3.25}$$

where d is the thickness of the PML, z_0 is the coordinate of the interface, and m is the order of polynomial variation, and σ_{max} is the maximum value of the conductivity. In this work, best results are obtained when maximum conductivity is about 3.3 and polynomial order is 4.

The conductivity variation along a PML region occupying 10 Yee cells is shown in Fig. 3.5.

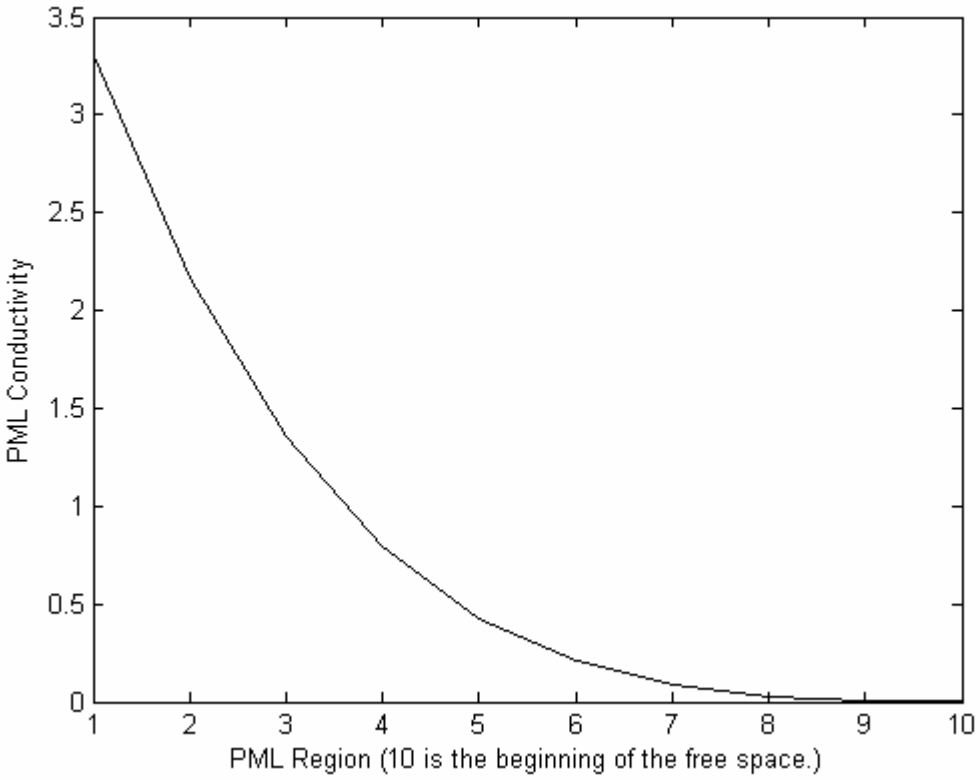

Figure 3.5: Conductivity Variation within a PML Region

The final graphs given in Figs. (3.6-3.9) are snapshots at time steps 81 and 1001. Using the periodicity of the sinusoidal time variation, these time instants are chosen such that the field strengths should be identical. In these figures, it is clear that the PML absorbs the incoming wave without any reflection.

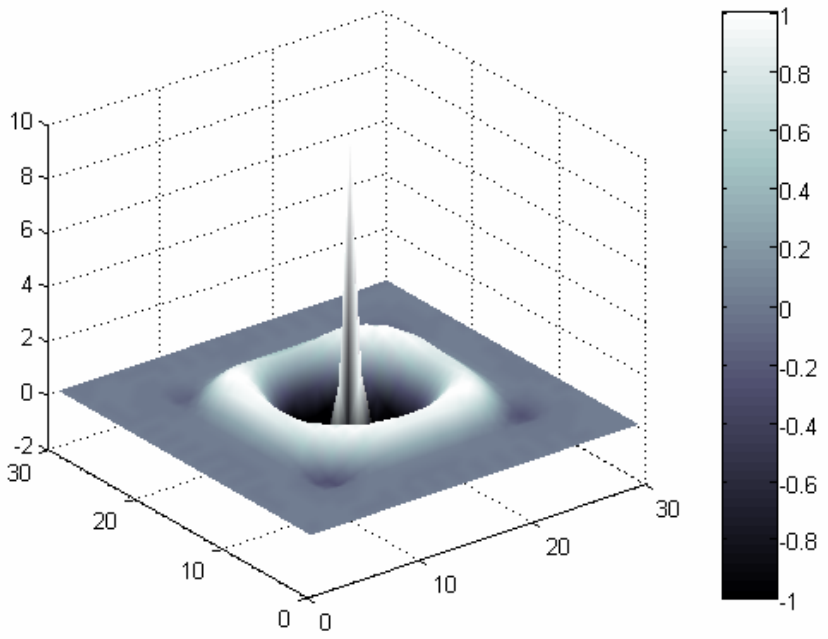

Figure 3.6: Snapshot of E_z component (over xy plane and $t = 81\Delta t$)

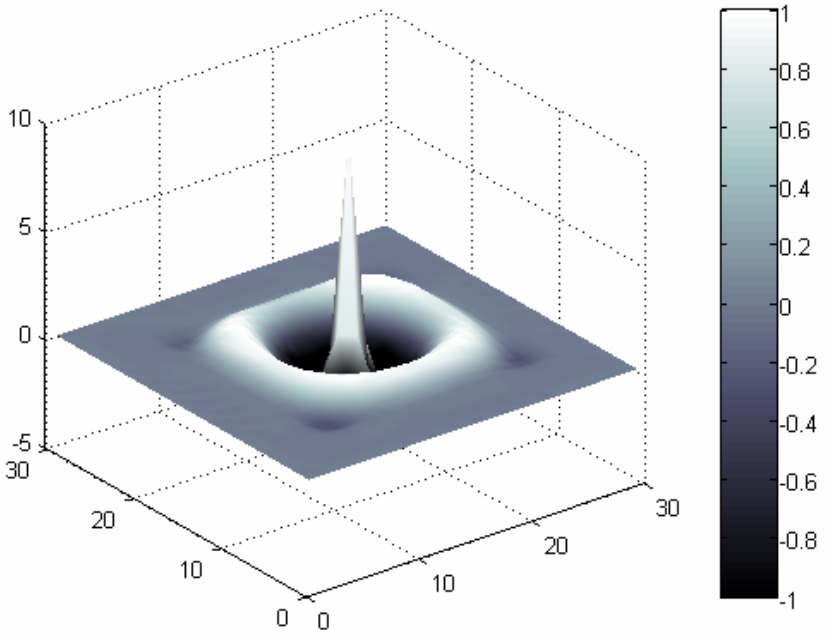

Figure 3.7: Snapshot of E_z component (over xy plane and $t = 1001\Delta t$)

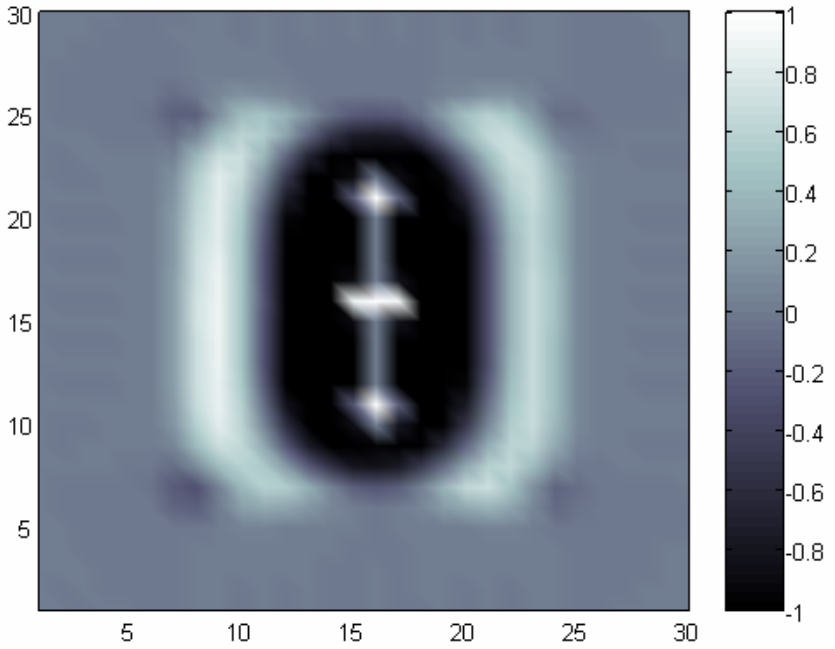

Figure 3.8: Snapshot of E_z component (over xz plane and $t = 81\Delta t$)

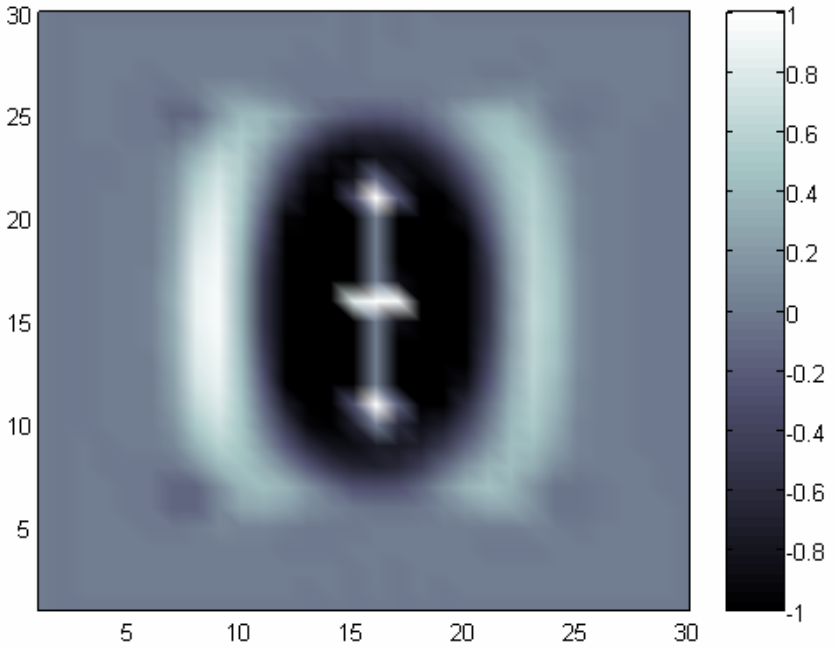

Figure 3.9: Snapshot of E_z component (over xz plane and $t = 1001\Delta t$)

CHAPTER 4

HUMAN HEAD MODEL FOR USE IN FDTD APPLICATIONS

In order to study the interaction of electromagnetic waves with human body tissues, a human head model is developed in this chapter. This model enables us to estimate the power dissipated inside a human head in the presence of an antenna located nearby simulating a mobile phone. The geometric information about the human head is obtained by MRI (Magnetic Resonance Imaging) images, and using these images different tissues are identified within the head. Finally, the constitutive parameters corresponding to different tissues are mapped to the Yee cells in the FDTD grid. In the last part of this chapter, details of a human head together with a tilted phone model is explained.

4.1 Human Head Tissues

In order to study the interaction of a human head with electromagnetic waves, permittivity, conductivity and mass density constants of a human head tissues are needed. From [11, 12], for 900 MHz mass density, relative dielectric and conductivity constants are shown at Table 4.1.

Table 4.1: Tissue Parameters for 900 MHz

Tissue	Mass Density (10^3 kg/m^3)	900 MHz.	
		ε_r	σ
Muscle	1.04	56.87	0.99
Bone (Skull)	1.85	16.62	0.24
Skin	1.10	41.40	0.86
Eye Humour	1.01	68.63	2.41
Lens	1.05	46.57	0.79
Cornea	1.05	55.23	1.39
Pitutary Gland	1.07	45.26	0.92
Brain	1.03	45.80	0.76

4.2 Human Head Discretization

MRI images of a female head are used to model the FDTD mesh. The cell size in the FDTD grid is chosen as 6.5 mm. The dimensions of the head are 218.10 mm (about 33 cells) in x-direction, 156.96 mm (24 cells) in y-direction and 204.41 mm (31 cells) in z-direction. The MRI images are available slice by slice, from which the geometry, as well as the tissue type are deduced. In Figs. 4.1 and 4.2, Middle Sagital and Middle Axial slices are given. In Appendix A, all 24 Sagital slices are given for the sake of completeness. The relevant information obtained from the $33x24x31$ slices is transferred to a file so that it can be imported by MATLAB during the execution of the code. In the FDTD model, each cell is assigned a tissue type (and the corresponding permittivity and conductivity values) by using the MRI slices as shown in Figs. 4.3 and 4.4.

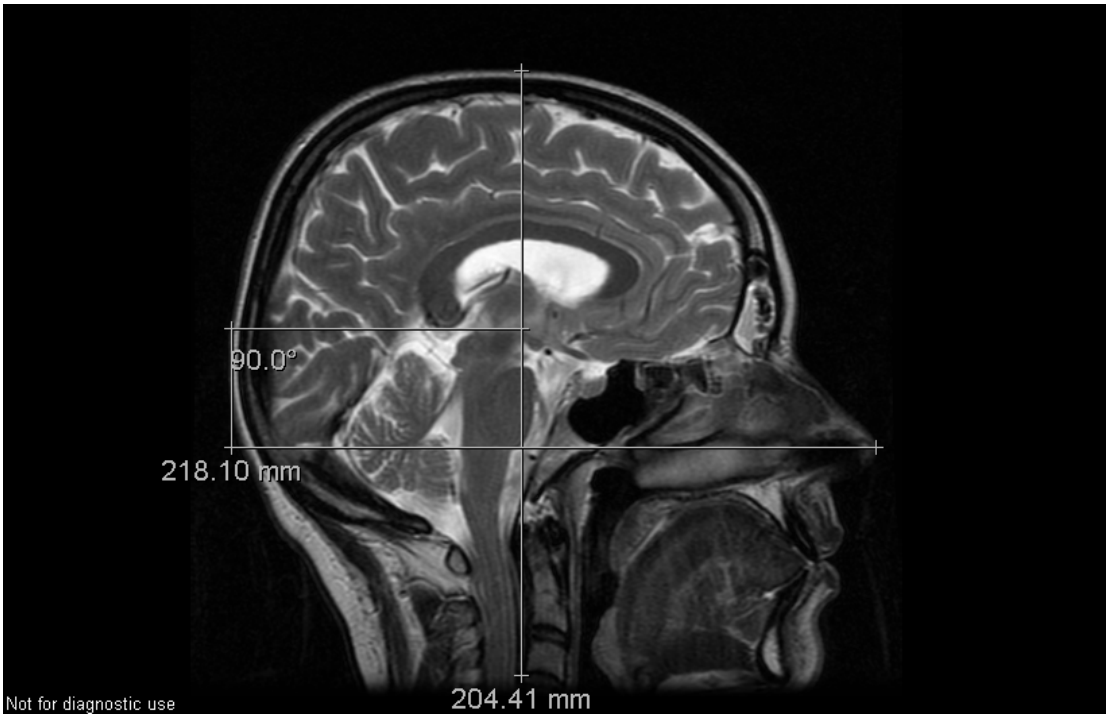

Figure 4.1: MRI Image of a Human Head in *xz* plane (Middle Sagital Slice)

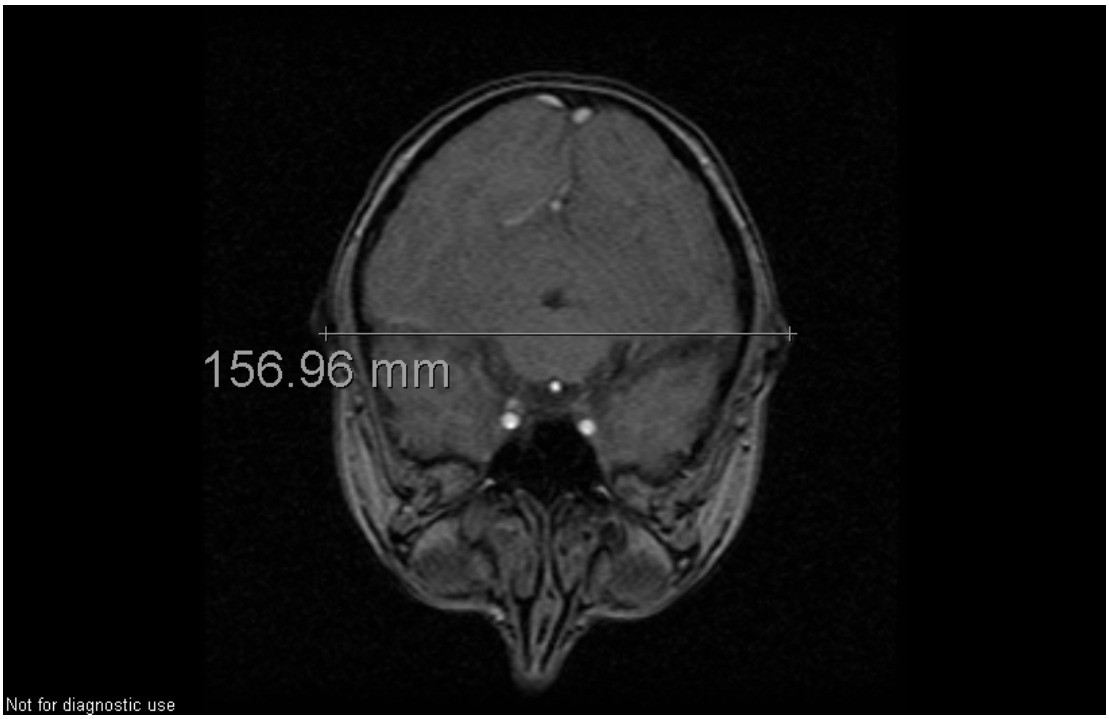

Figure 4.2: MRI Image of a Human Head in *xy* plane (Middle Axial Slice)

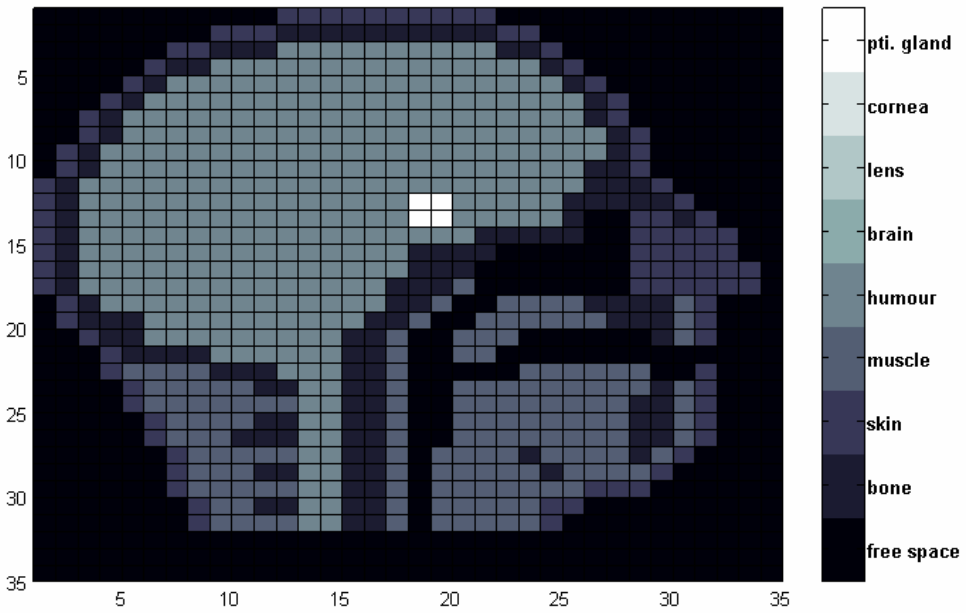

Figure 4.3: FDTD Model of the Head (Middle *xz* plane)

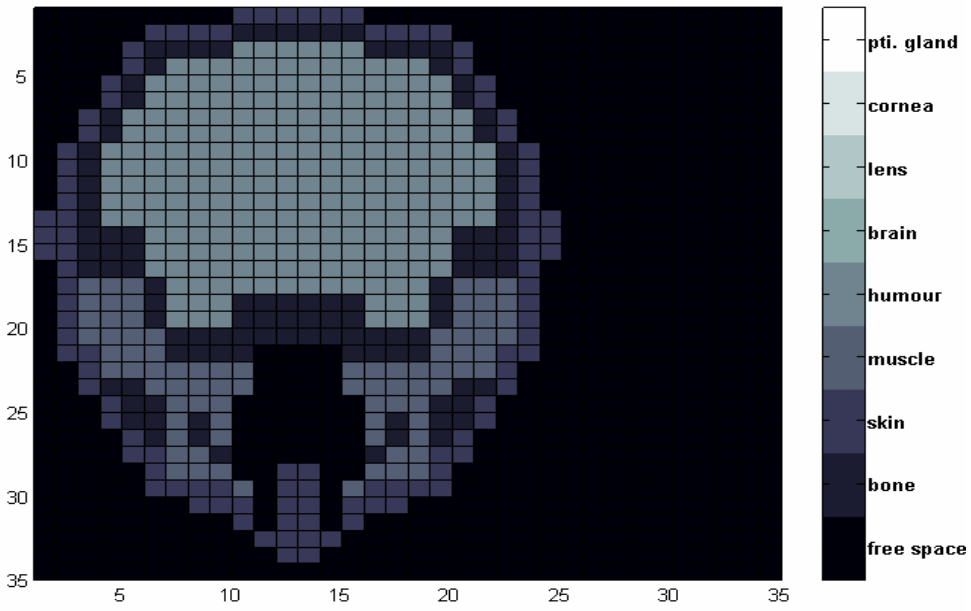

Figure 4.4: FDTD Model of the Head (Middle *xy* plane)

4.3 Human Head Model with a Tilted Mobile Phone

The easiest model combining a human head with a mobile phone is the case where the human head axis and the phone antenna are in the same direction, which means that the angle between head axis and antenna axis is zero. However, this model is not realistic since people generally hold phones tilted with respect to their heads. This angle may be chosen from the range of angles 15-30 degrees. It is certain that in the FDTD model, it is more efficient to rotate the human head rather than the phone. In Figs. 4.6 and 4.7, the tilted head models are illustrated. A non-tilted mobile phone model is coupled to complete the picture.

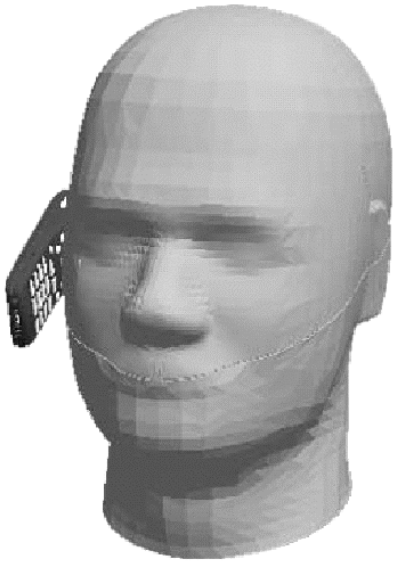

Figure 4.5: Human Head with a Tilted Mobile Phone

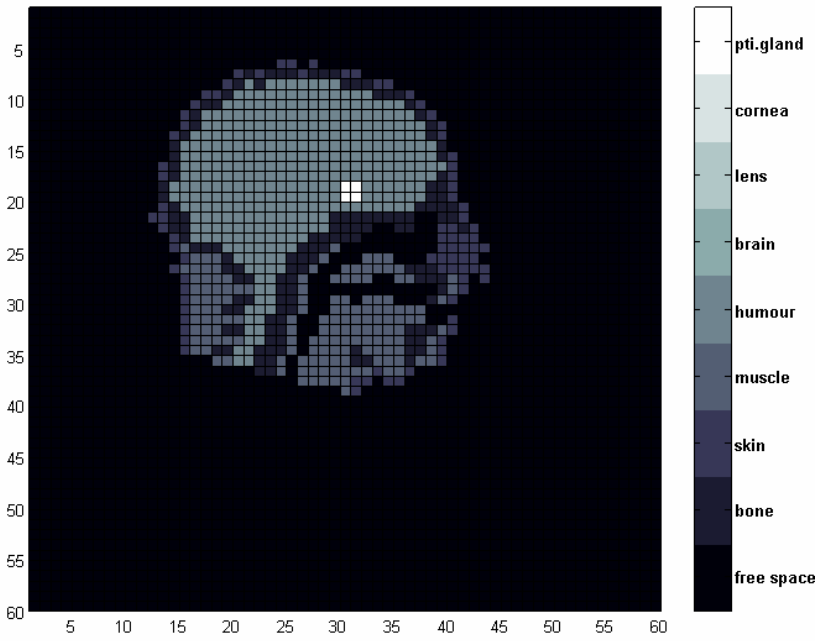

Figure 4.6: Middle Sagital Head Slice (15° tilted with respect to the Antenna Axis)

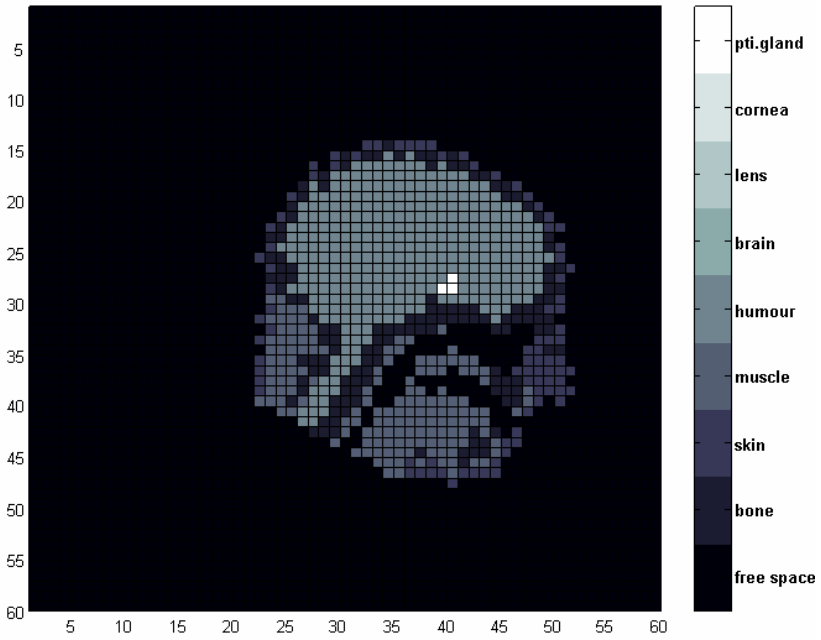

Figure 4.7: Middle Sagital Head Slice (30° tilted with respect to the Antenna Axis)

CHAPTER 5

ANTENNA MODELS AND FDTD CODE VERIFICATION

Since the human head model is developed in the previous chapter, the next step will be the derivation of antenna models (including the feed structure) and verification and validation of these models in radiation problems in free space or in the presence of PEC or dielectric obstacles.

5.1 Antennas

An antenna is defined as "a usually metallic device for radiating or receiving radio waves" [13]. It is well-known that charges must be accelerated (or decelerated) in order to create radiation. This result may be obtained either by time-varying excitations or geometric discontinuities (terminations, changes in curvature,..etc.).

5.2. Source Models in the FDTD Approach

The simplest and most common approach for source modeling is known as E-field or voltage excitation. In Fig. 5.1, a dipole antenna feed gap is represented by a single cell (the arms of the dipole antenna extends above and below the cell representing the gap). The gap is excited by a voltage source and the electric field intensity within the gap is evaluated as the voltage of the source divided by the gap width δ. In FDTD models, the gap may not be infinitesimal, since the gap extent cannot be smaller than the cell size.

This is one of the drawbacks of the FDTD method, in modeling antenna feeds realistically.

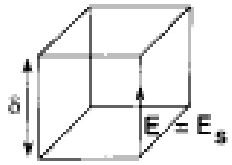

Figure 5.1: E Field Excitation in a Cell (Representing an Antenna Feed)

Another method to model the feed is to use an equivalent frill generator by forcing the four tangential magnetic field components at the position of the feed surrounding the wire to a known sinusoidal form.

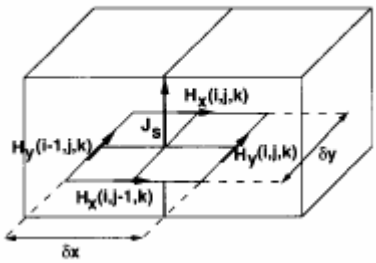

Figure 5.2: An Equivalent Frill Generator to model Current Density

As a third possibility, if the current distribution is known current density can be substituted directly into the curl equation as impressed source.

5.3 Examples and Validation

In this section, some examples will be considered to validate the FDTD antenna models with or without scatterers. The results obtained by FDTD simulations are either compared with analytical results (provided that they are available) or in the case of antenna radiation problems in the presence of scatterers, numerical results are

interpreted in terms of the problem physics.

5.3.1 Evaluation of the Radiation Resistance of a Half-Wave Dipole Antenna

In this example, the radiation resistance of a half-wave dipole antenna is evaluated in terms of the FDTD code, and the result is compared with the analytical solution. For this purpose, the analytical solution is given below.

5.3.1.a Analytical Solution

For the dipole, the average Poynting vector can be written as

$$W_{av} = \frac{1}{2}\mathrm{Re}[ExH^*] = \frac{1}{2}\mathrm{Re}[\hat{a}_\theta E_\theta x \hat{a}_\phi H_\phi{}^*] = \frac{1}{2}\mathrm{Re}[\hat{a}_\theta E_\theta x \hat{a}_\phi \frac{E_\theta{}^*}{\eta}] \tag{5.1}$$

$$W_{av} = \hat{a}_r \frac{1}{2\eta}\left|E_\theta\right|^2 = \eta \frac{\left|I_0\right|^2}{8\pi^2 r^2}\left[\frac{\cos(\frac{kl}{2}\cos\theta) - \cos(\frac{kl}{2})}{\sin\theta}\right]^2 \tag{5.2}$$

To find the total radiated power, the average Poynting vector from (5.2) is integrated over a sphere of radius r.

$$P_{rad} = \iint W_{av}.dS = \int_0^{2\pi}\int_0^{\pi} \hat{a}_r W_{av}.\hat{a}_r r^2 \sin\theta d\theta d\phi = \int_0^{2\pi}\int_0^{\pi} W_{av} r^2 \sin\theta d\theta d\phi \tag{5.3}$$

$$P_{rad} = \eta \frac{\left|I_0\right|^2}{4\pi}\int_0^{\pi}\left[\frac{\cos(\frac{kl}{2}\cos\theta) - \cos(\frac{kl}{2})}{\sin\theta}\right]^2 d\theta \tag{5.4}$$

After some extensive manipulation, in can be shown that the (5.4) reduces to

$$P_{rad} = \eta \frac{|I_0|^2}{4\pi}\{C + \ln(kl) - Ci(kl) + \frac{1}{2}\sin(kl)[Si(2kl) - 2Si(kl)] + \frac{1}{2}\cos(kl)[C + \ln(kl/2) + Ci(2kl) - 2Ci(kl)]\} \quad (5.5)$$

where C=0.5772 (Euler's constant) and $Ci(x)$ and $Si(x)$ are the cosine and sine integrals given by

$$Ci(x) = -\int_x^\infty \frac{\cos y}{y} dy = \int_\infty^x \frac{\cos y}{y} dy$$
$$Si(x) = \int_0^x \frac{\sin y}{y} dy \quad (5.6)$$

The radiation resistance can be obtained as

$$R_r = \frac{2P_{rad}}{|I_0|^2} = \frac{\eta}{2\pi}\{C + \ln(kl) - Ci(kl) + \frac{1}{2}\sin(kl)[Si(2kl) - 2Si(kl)] + \frac{1}{2}\cos(kl)[C + \ln(kl/2) + Ci(2kl) - 2Ci(kl)]\} \quad (5.7)$$

The radiation resistance R_r is related to the input resistance R_{in} as follows [13]

$$\frac{|I_{in}|^2}{2} R_{in} = \frac{|I_0|^2}{2} R_r \quad (5.8)$$

where I_{in} is the input current and I_0 is the maximum value of the current.

Thus the input resistance can be expressed as

$$R_{in} = \frac{R_r}{\sin^2(\frac{kl}{2})} \quad (5.9)$$

The variation of R_r and R_{in} with respect to antenna length is given in Fig. 5.3

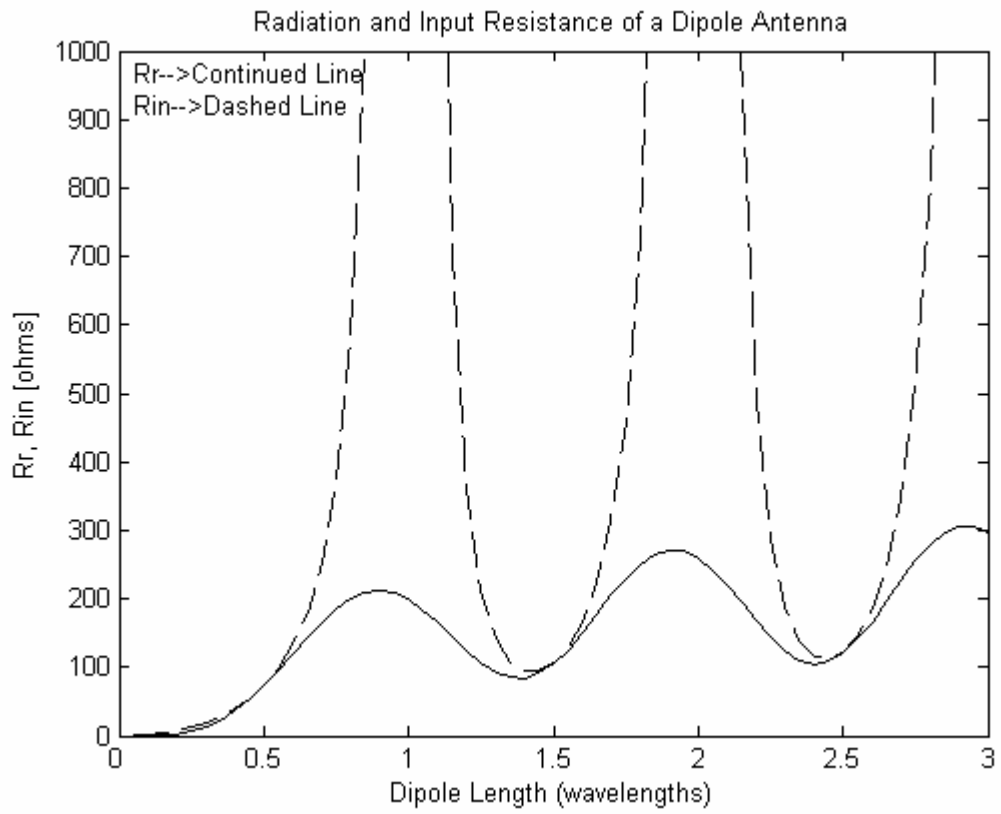

Figure 5.3: R_r and R_{in} of a Thin Dipole Antenna

In a similar manner, imaginary part of input impedance can be expressed as

$$X_m = \frac{\eta}{4\pi}\{2Si(kl) + \cos(kl)[2Si(kl) - Si(2kl)] - \sin(kl)[2Ci(kl) - Ci(2kl) - Ci(\frac{2ka^2}{l})]\} \tag{5.10}$$

$$X_{in} = \left(\frac{I_0}{I_{in}}\right)^2 X_m = \frac{X_m}{\sin^2(\frac{kl}{2})} \tag{5.11}$$

Where a is the radius of the wire. ($a = 10^{-10}\lambda$ is chosen)

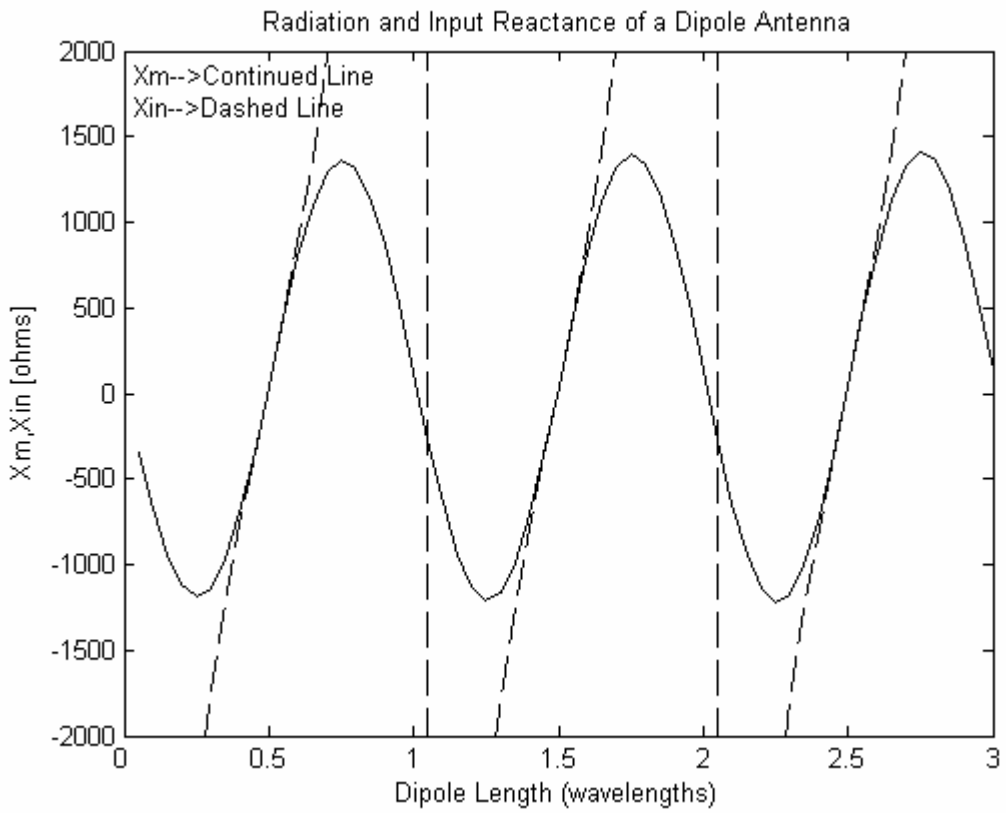

Figure 5.4: Radiation and Input Reactance of a Thin Dipole Antenna

The magnitude of the input impedance is found as

$$Z_{in} = \sqrt{R_{in}^{\ 2} + X_{in}^{\ 2}} \tag{5.12}$$

For a half-wave dipole antenna

R_{in} and X_{in} are 73.1291 and 42.5445 Ω.

Hence, the analytical result for the magnitude of the input impedance is Z_{in} =84.6044 Ω

5.3.1.b Numerical Solution

In the simulation, a sinusoidal voltage with amplitude 1 V (shown in Fig. 5.5) is applied to the gap of the dipole antenna. At each time step, current is calculated by implementing Ampere's Law.

$$I = \int H.dl \tag{5.13}$$

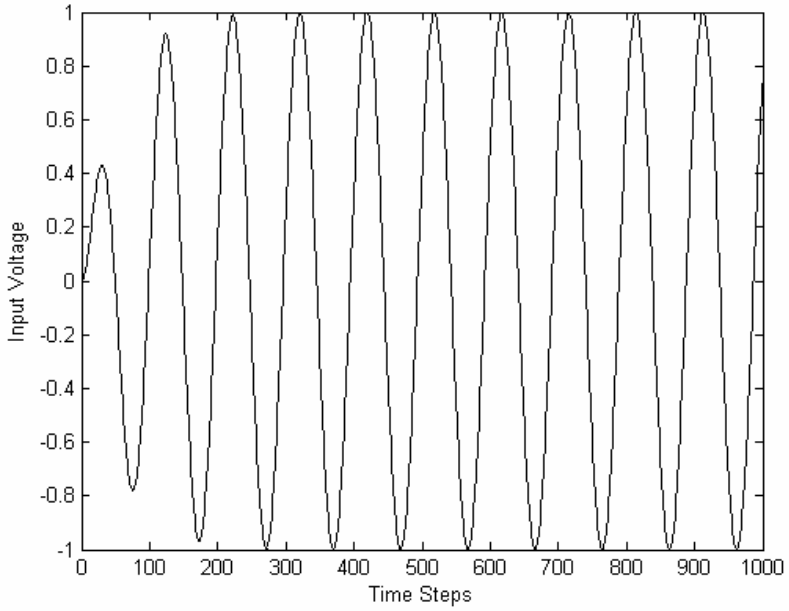

Figure 5.5: Input Voltage of the Dipole Antenna versus Time

In Fig. 5.6, the input current of the dipole antenna is shown, whose amplitude turns out to be 0.0117 A. As a result, the magnitude of the input impedance is found as $Z_{in} = 85.2047\Omega$. This result is very close to the exact one.

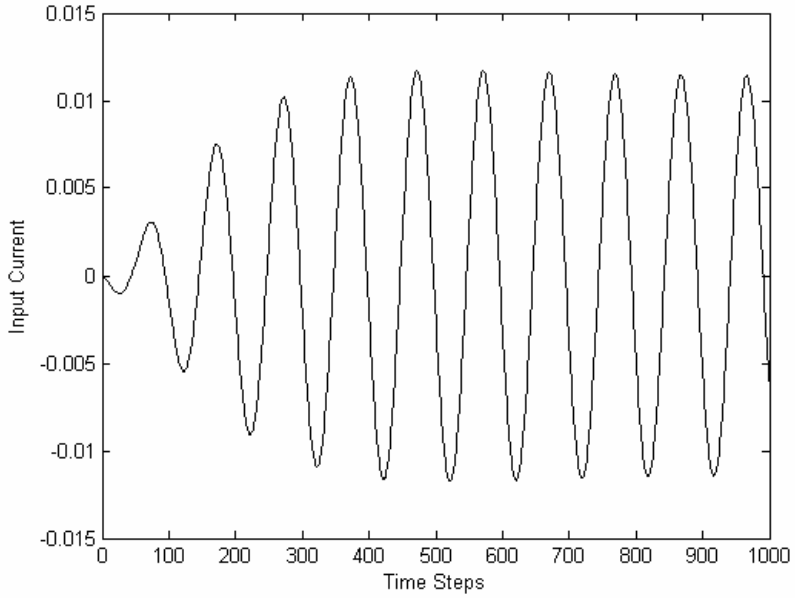

Figure 5.6: Input Current of the Dipole Antenna versus Time

5.3.2 Verification of Accuracy of Electric Field Intensity in FDTD Simulations

The current distribution along a very thin dipole can approximately be written as

$$I_e(x'=0, y'=0, z') = \begin{cases} \hat{a}_z I_0 \sin\left[k\left(\frac{l}{2} - z'\right)\right], 0 \le z' \le \frac{l}{2} \\ \hat{a}_z I_0 \sin\left[k\left(\frac{l}{2} + z'\right)\right], -\frac{l}{2} \le z' \le 0 \end{cases} \tag{5.14}$$

The θ and φ electric and magnetic field components in the intermediate field are expressed as

$$\begin{aligned} dE_\theta &\approx j\eta \frac{kI_e(x', y', z')e^{-jkR}}{4\pi R} \sin\theta dz' \\ dH_\phi &\approx j \frac{kI_e(x', y', z')e^{-jkR}}{4\pi R} \sin\theta dz' \end{aligned} \tag{5.15}$$

After some manipulations, (5.15) reduces to

$$E_\theta \approx j\eta \frac{I_0 e^{-jkr}}{2\pi R}\left[\frac{\cos\left(\frac{kl}{2}\cos\theta\right)-\cos\left(\frac{kl}{2}\right)}{\sin\theta}\right]$$
$$H_\phi = \frac{E_\theta}{\eta} \approx j\frac{I_0 e^{-jkr}}{2\pi R}\left[\frac{\cos\left(\frac{kl}{2}\cos\theta\right)-\cos\left(\frac{kl}{2}\right)}{\sin\theta}\right] \quad (5.16)$$

In Fig. 5.7, numerical and analytical results are compared for a z-directed thin dipole antenna extending along 25 cells and located in the middle of a computational domain with $70x70x70$ and 1 V is applied to the gap of the antenna. The cell size is lambda/50 and frequency is chosen as 900 MHz. E_z is computed analytically and numerically at a point 22 cells away from the gap on z=0 plane. A phase error is observed for this specific point but amplitude values match perfectly.

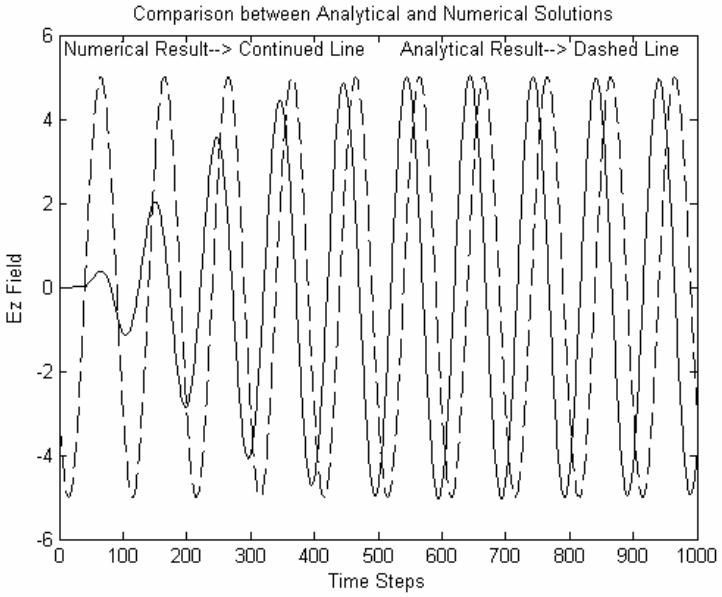

Figure 5.7: Comparison of the analytical and numerical results for E_z component

In Fig. 5.8, the observation point vector measured from the gap is taken as $(20\Delta x, 20\Delta y, 0)$ and the numerical and analytical values of the E_z component are given.

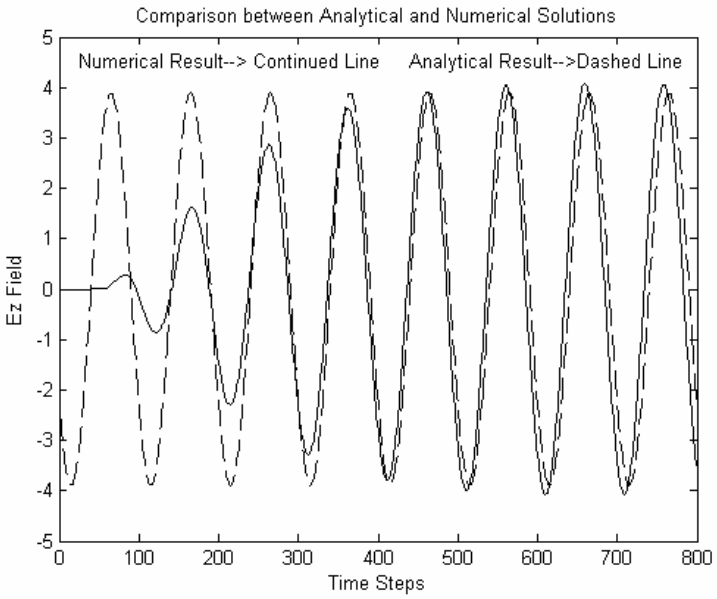

Figure 5.8: Comparison of the analytical and numerical results for E_z component. ($20x\sqrt{2}\ \Delta x$ away from the gap)

5.3.3 Power Density Calculations

The magnitude of the power density vector is given as

$$P_{density} = \frac{|E|^2}{2\eta} \tag{5.17}$$

If a voltage is applied to the antenna gap, the input power turns out to be

$$P = \frac{|V|^2}{2Z_{in}} \tag{5.18}$$

In equations (5.17) and (5.18), E and V are the peak values of the sinusoidal electric field and voltage, respectively.

The voltage that should be applied at the antenna gap must be determined in terms of the power and input impedance specifications. As a particular example, power can be taken as 0.6 W. (Power rating for cellular phones operating at 900 MHz) The length of the dipole is taken as $\frac{\lambda}{2}$. Consequently, input impedance can be taken approximately as $85\ \Omega$. Then, the applied voltage must be about 10 V. The behaviors of the E_z field and power density magnitudes are illustrated in Figs. 5.9 and 5.10.

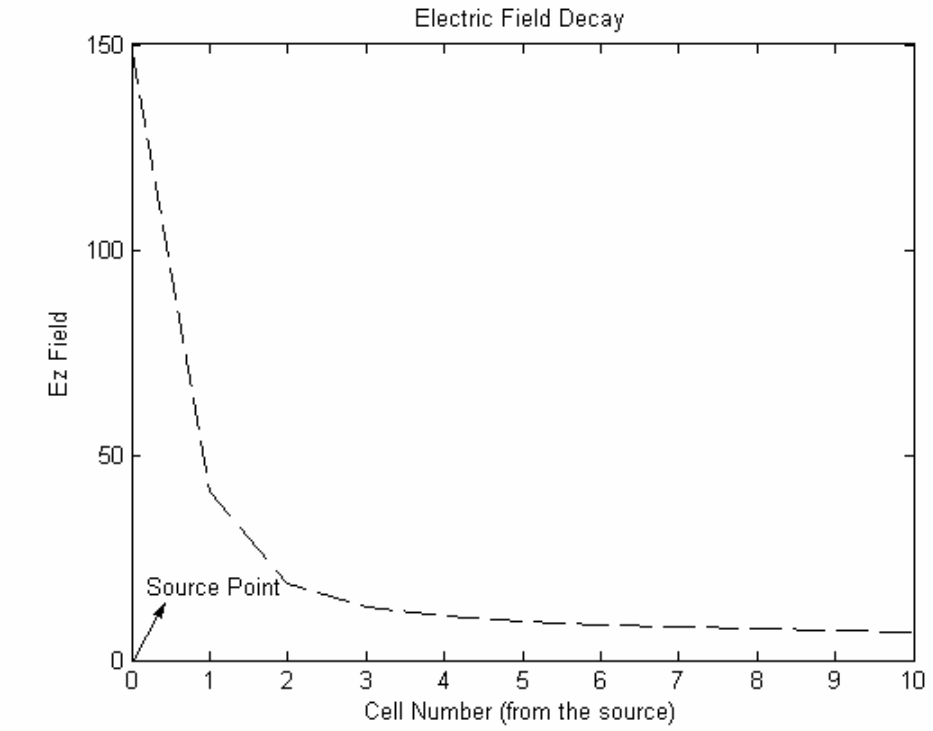

Figure 5.9: Electric Field Decay at an Axis (Half Wave Dipole)

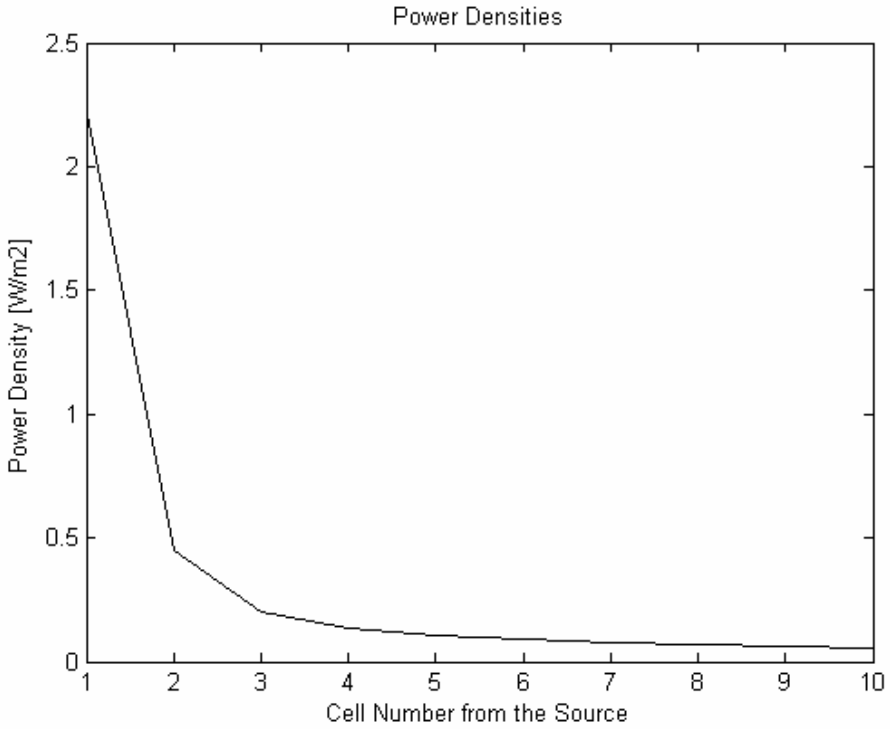

Figure 5.10: Power Density Decay at an Axis (Half Wave Dipole)

5.3.4 Examples Related to an Antenna Radiating in the Presence of Scatterers

5.3.4.a A Dipole Antenna Radiating in the Presence of a PEC Cube

In this example, a thin dipole antenna (whose length is equal to λ) radiates in the presence of a PEC cube is used to illustrate the propagation of wave about 900 MHz. The computational domain contains $50x50x50$ cells with cell size $\delta = \frac{\lambda}{10}$ and the side length of the cube is 10 δ. The PEC cube is located 5 cells away from the antenna. In Figs. (5.11-5.14), the snapshots of E_z component are illustrated.

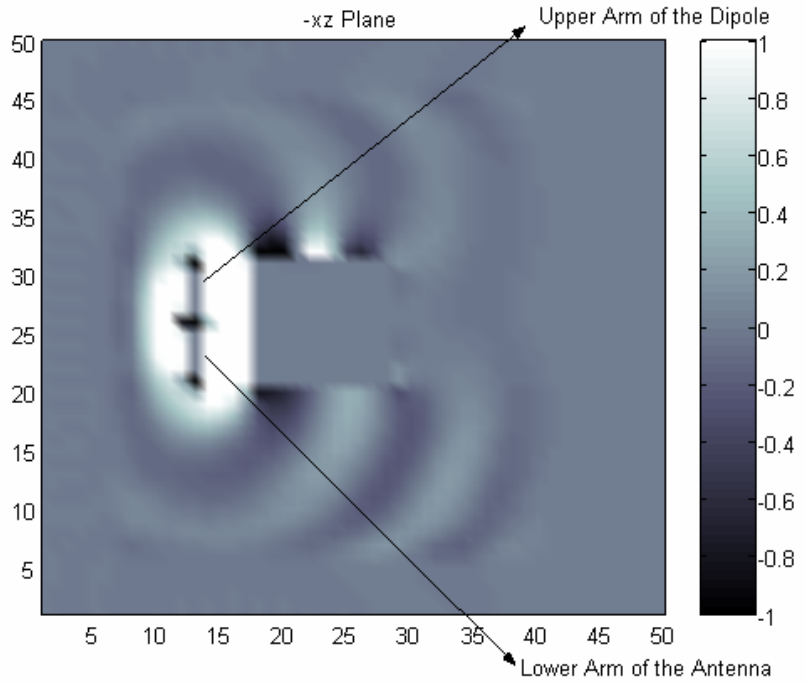

Figure 5.11: Snapshot of the E_z component at $y = 0$ plane (PEC cube case)

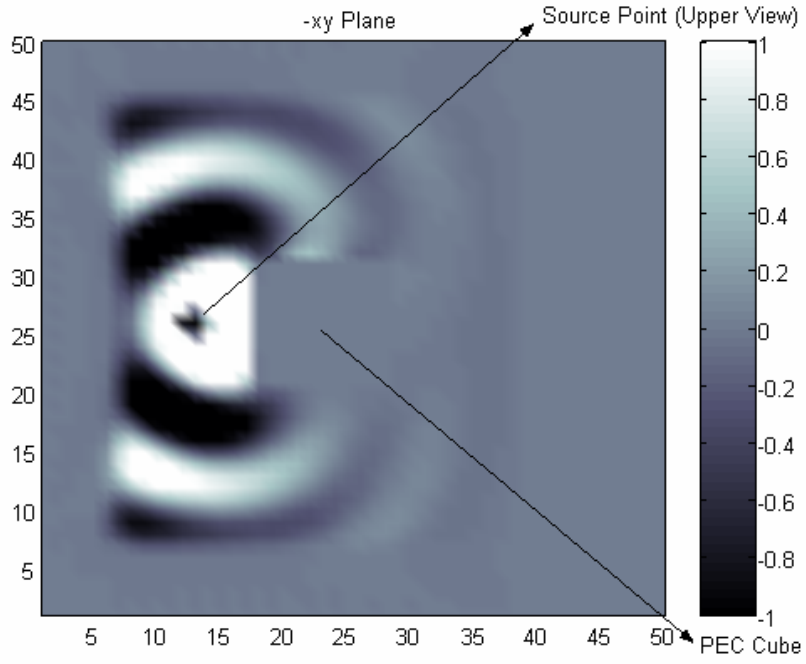

Figure 5.12: Snapshot of the E_z component at $z = 0$ plane (PEC cube case)

5.3.4.b A Dipole Antenna Radiating in the Presence of a Dielectric Cube

In this example, all the geometric specifications are exactly the same as those given in 5.3.4.a, but the PEC cube is replaced by a dielectric cube whose relative permittivity is 4. In Figs. (5.13-5.14), the snapshots of E_z component are illustrated for this case.

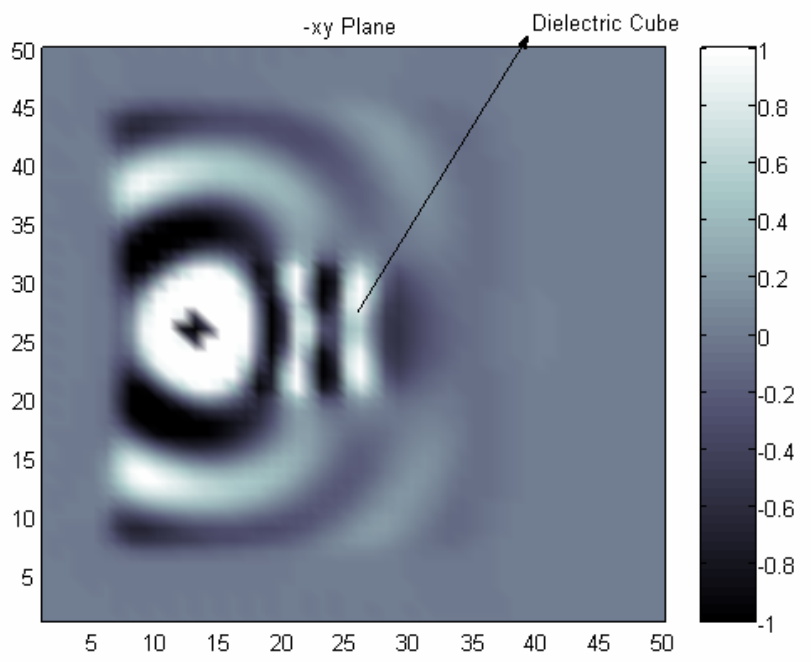

Figure 5.13: Snapshot of the E_z component at $z = 0$ plane (Dielectric cube case)

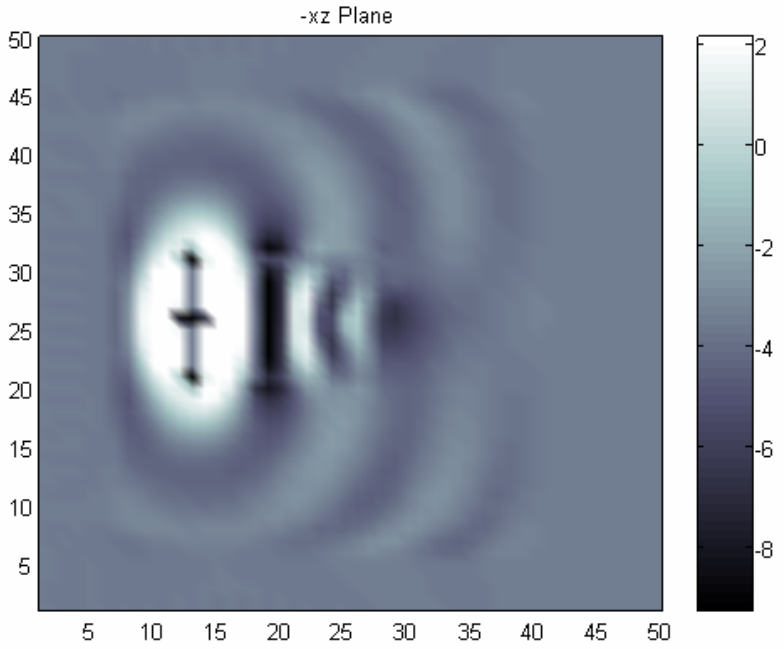

Figure 5.14: Snapshot of the E_z component at $y = 0$ plane (Dielectric cube case)

CHAPTER 6

FDTD SIMULATION OF THE INTERACTION OF ELECTROMAGNETIC FIELDS WITH THE HUMAN HEAD

6.1 Electromagnetic Spectrum and Cellular Phones

In Europe, the frequencies used in mobile communication are basically 900 and 1800 MHz. Mobile phones operate at frequencies in the Radio Frequency (RF) region, which is also known as the non-ionizing part of the electromagnetic spectrum. This implies that electromagnetic waves radiated from cellular phones are not able to ionize atoms or molecules in human body. However, the field penetrating in the body will induce currents which are dissipated and converted to heat energy. The main aim of this chapter is to obtain results in this direction by using FDTD models.

6.2 Field Strength, Power Density and Specific Absorption Rate (SAR)

In problems related to the interaction of electromagnetic fields with human body tissues, the values of the electric and magnetic field strengths, power density and the specific absorption rate (SAR) play a critical role. The specific absorption rate (SAR) is defined as follows:

$$SAR = \frac{|E|^2 \sigma}{\rho} \tag{6.1}$$

where $|E|$ is the magnitude of the measured or computed RMS electric field, σ is the tissue conductivity and ρ is the tissue mass density. SAR is a measure of the rate of energy absorption per unit mass at a specific location in the tissue. SAR may be expressed in the units such as watts/kg or miliwatts/gr.[14]

Before routine RF evaluation of a device can proceed, it must be determined whether it should be considered under the "mobile" or "portable" category, and whether exposure would occur under the occupational/controlled or general population/uncontrolled conditions. These decisions will generally determine whether a device should be evaluated with respect to field strength, power density or SAR limits, and which set of exposure limits would be applicable for determining compliance.

For certain devices, such as wireless modem modules and other transmitters that are designed to be integrated into other products or designed to operate in multiple configurations, RF exposure evaluation for both mobile and portable conditions may be necessary. In such cases, RF compliance must be determined with respect to SAR limits when portable configurations are applicable. There are other situations where the operator of a device is in close proximity to the transmitter but nearby persons are normally further away from the device. Under such conditions, the occupational/controlled exposure limits may be applied to the operator provided he or she is aware of the exposure conditions and can exercise control to limit the exposure durations and/or conditions to satisfy compliance. The more restrictive, general population/uncontrolled exposure limits must be applied to nearby persons who have no knowledge of their exposure conditions but are normally further away from the transmitter where the exposure is generally weaker. [14]

FCC Limits for Maximum Permissible Exposure (MPE):

Table 6.1: Limits for Occupational/Controlled Exposure (for MPE)

Frequency Range (MHz)	*Electric Field Strength (V/m)*	*Magnetic Field Strength (A/m)*	*Power Density (mW/cm^2)*
0.3-3.0	614	1.63	100
3.0-30	1842/f	4.89/f	900/f^2
30-300	61.4	0.163	1.0
300-1500	--	--	f/300
1500-100000	--	--	5

Table 6.2: Limits for General Population/Uncontrolled Exposure (for MPE)

Frequency Range (MHz)	*Electric Field Strength (V/m)*	*Magnetic Field Strength (A/m)*	*Power Density (mW/cm^2)*
0.3-3.0	614	1.63	100
3.0-30	824/f	2.19/f	180/f^2
30-300	27.5	0.073	0.2
300-1500	--	--	f/1500
1500-100000	--	--	1.0

FCC Limits for Specific Absorption Rate (SAR):

Table 6.3: Limits for Occupational/Controlled Exposure (for SAR)

Whole-Body	Partial-Body	Hands, Wrists, Feet and Ankles
0.4	8.0	20.0

Table 6.4: Limits for General Population/Uncontrolled Exposure (for SAR)

Whole-Body	Partial-Body	Hands, Wrists, Feet and Ankles
0.08	1.6	4.0

From Tables, 6.1, 6.2, 6.3 and 6.4, it can be clearly seen that for cellular phones, electric or magnetic field strengths are not directly applicable to handle safety issues. Instead, power density and SAR values must be calculated to estimate cellular phone safety. This necessitates the modeling of mobile phones as well as human head in FDTD simulations.

6.3 Phone Model and Maximum Permissible Exposure

In this work, a cellular phone model is used, whose dimensions are 4.55 cm. in x direction, 1.30 cm. in y direction and 11.05 cm. in z direction. The cubic cell size is $\delta = 0.65$ cm which means that the phone is consisting of 7 x 2 x 17 cells. The antenna length is taken as 4.55 cm. (7 cells). The phone model is illustrated in Figs. 6.1 and 6.2.

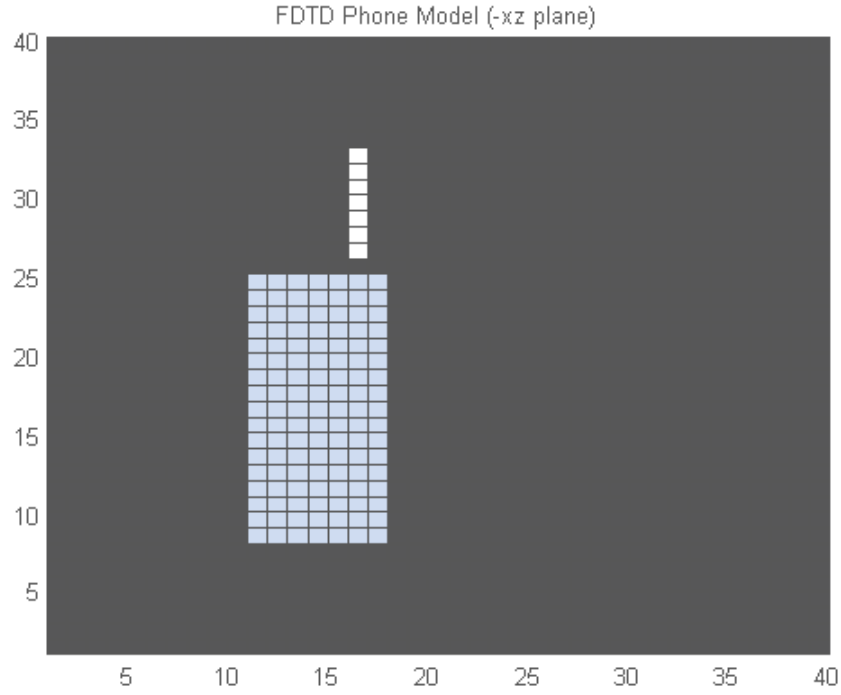

Figure 6.1: FDTD Phone Model ($y = 0$ plane)

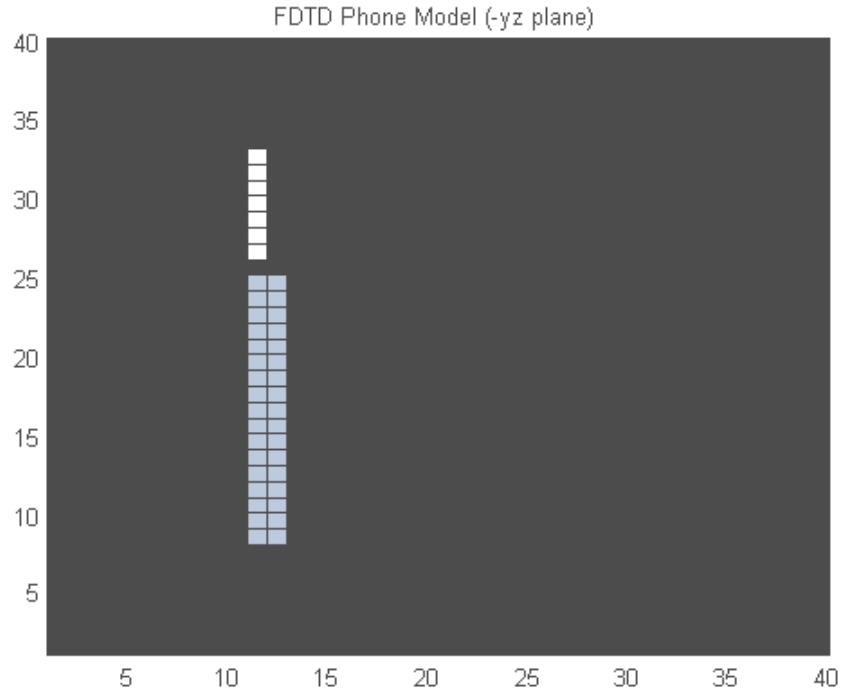

Figure 6.2: FDTD Phone Model ($x = 0$ plane)

From Table 6.2, it can be easily seen that for uncontrolled environment, maximum permissible exposure must be equal or less than $\frac{f[MHz]}{1500} = 0.6 \text{ mW}/cm^2$. In order to be able to understand the geometric restrictions under which this safety limit holds, the power density variation obtained from the FDTD simulation of the phone model is obtained which is illustrated in Fig. 6.5. It is seen that the threshold is slightly exceeded at the 6th cell. As a result, it can be concluded that the head must be at least 3.9 cm. away from the source or equivalently 2.6 cm. away from the front face of the phone. This result is almost a replica of the ANSI, IEEE advice which suggests that mobile phones should not be closer that 2 cm to human head [15].

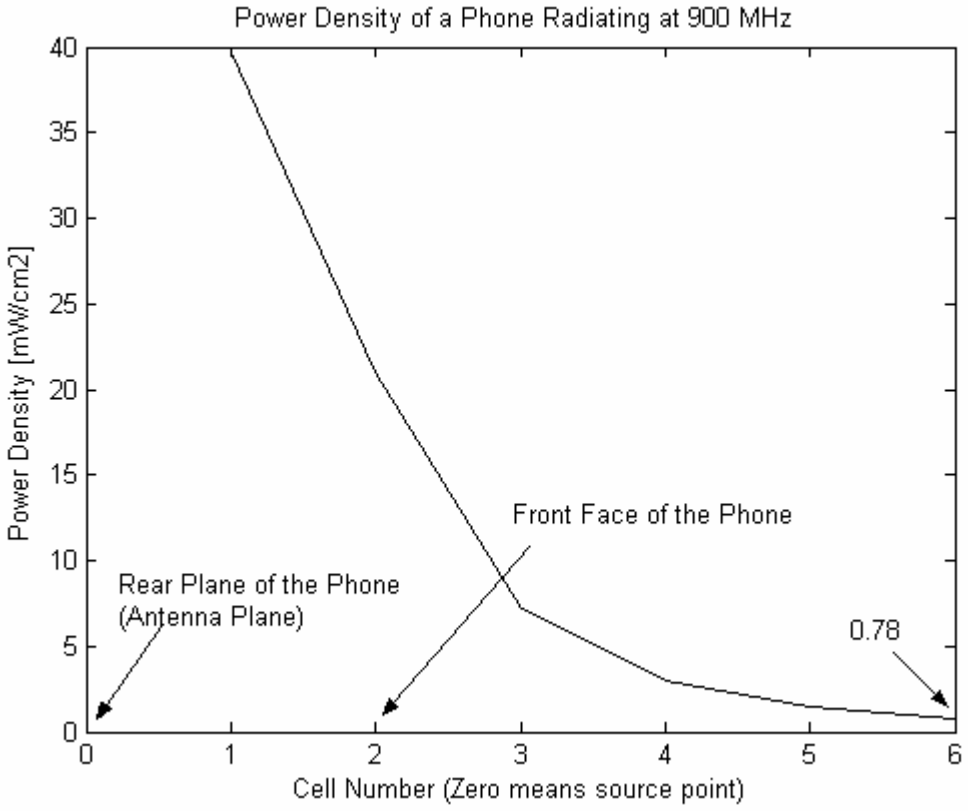

Figure 6.3: Power Density of a Phone radiating at 900 MHz

6.4 Specific Absorption Rate (SAR) Calculations by the Human Head-Mobile Phone FDTD Model

The MPE calculations are carried out in the absence of the human head, and the MPE definition is meaningful in the intermediate or far fields of antennas where the wave is almost a plane wave. However, in the case of a cellular phone placed close to a human head, near field calculations are essential. Therefore, in this case, the SAR concept proves to be the meaningful criterion for safety issues.

An exposure condition, which is given in Tables 6.3 and 6.4, can be considered to be acceptable if it can be shown that it produces SARs below 0.08 W/kg, as averaged over the whole body, and spatial peak SAR values not exceeding 1.6 W/kg, as averaged over any 1 g of tissue (defined as a tissue volume in the shape of cube). [15]

At 900 MHz, peak SAR values are shown in Fig. 6.4. There is no distance between phone and head. Simulation is finished after 10 cycles are passed. In other words, it reaches steady state. White color means equal or greater than 1.6 W/kg. That's why in the figures, white regions are equal or greater than upper limit.

6.5 Results of the FDTD Human Head-Mobile Phone Simulations

In this part of the thesis, the mobile phone-human head interaction is studied for some configurations. In the first simulation, the distance between the vertically placed mobile phone and the head is zero. Next, the distance between the head and the phone is raised to one cell. Finally, a simulation of the radiation of the tilted phone is discussed. In all cases, the human head model developed in Chapter 4 and the phone model developed in this chapter are placed in an FDTD grid with cell size $\delta = \frac{\lambda}{50}$.

6.5.1. First Simulation

In this case, the distance between the phone and head is taken to be zero. The power of the mobile phone is chosen as 0.6 W. The results are presented in Table 6.5 and Figs (6.4-6.7). In Table 6.5, peak and average SAR values are given in voxels (volume cells), and sometimes aggregates of cells need to be considered for SAR calculations in tissues with mass 1g. This distinction is mentioned in all Tables related to SAR calculations. The Figs. (6.4-6.7) denote the SAR value distribution within the head at $z = 0$, $y = 0$ and $x = 0$ planes respectively. In these figures, the upper limit of the gray scale is set to 1.6 W/Kg in order to be able to represent the tissue parts where the SAR value exceeds the safety limit. Fig. 6.7 is a replica of Fig. 6.6 with a reduced scale to show the penetration of the wave within the head. The maximum voxel-SAR value (18.6528 W/kg) occurs at the point $(34\delta, 14\delta, 36\delta)$, which corresponds to skin on auricle.

Table 6.5: SAR Distributions in the Head at 900 MHz

(The distance between antenna and head is 2 cells and between phone front plane and head is zero.)

	Adult Female
Peak 1-voxel SAR (W/kg)	18.6528
Peak 1-g SAR (W/kg)	5.7772
Peak 1-voxel SAR for Bone (W/kg)	1.7248
Peak 1-voxel SAR for Skin (W/kg)	18.6528
Peak 1-voxel SAR for Muscle (W/kg)	3.9255
Peak 1-voxel SAR for Brain (W/kg)	1.5873
Peak 1-voxel SAR for Humour (W/kg)	0.0050
Peak 1-voxel SAR for Lens (W/kg)	0.0023
Peak 1-voxel SAR for Cornea (W/kg)	0.0215
Peak 1-voxel SAR for Pitutary Gland (W/kg)	0.0152
Average SAR for Bone (mW/kg)	15.0
Average SAR for Skin (mW/kg)	61.2
Average SAR for Muscle (mW/kg)	24.7
Average SAR for Brain (mW/kg)	26.0
Average SAR for Humour (mW/kg)	1.8
Average SAR for Lens (mW/kg)	0.9
Average SAR for Cornea (mW/kg)	3.0
Average SAR for Pitutary Gland (mW/kg)	13.8
Average Whole Body SAR (W/kg)	0.1348

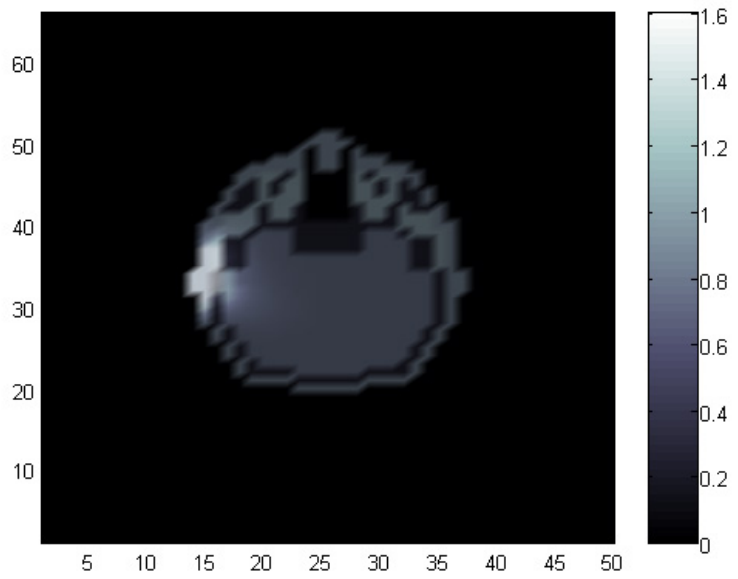

Figure 6.4: SAR distribution within the human head at $z = 0$ plane at 900 MHz (the distance between the head and the phone is zero)

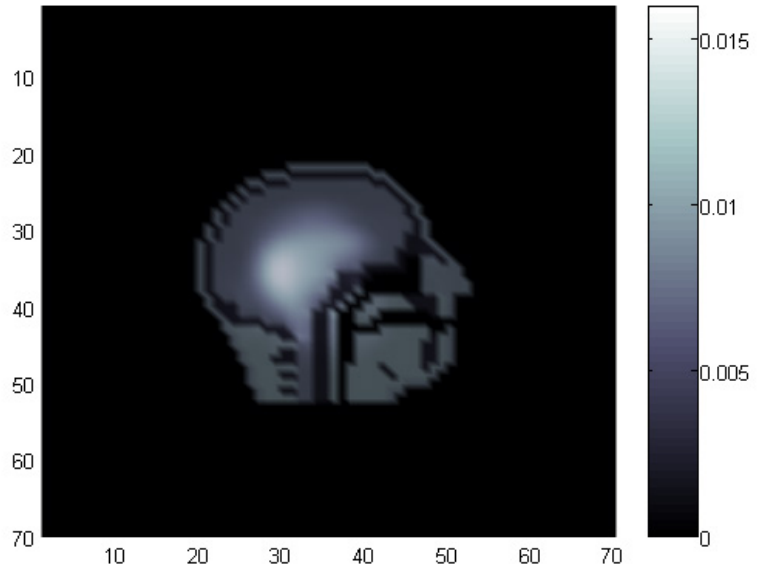

Figure 6.5: SAR distribution within the human head at $y = 0$ plane at 900 MHz (the distance between the head and the phone is zero)

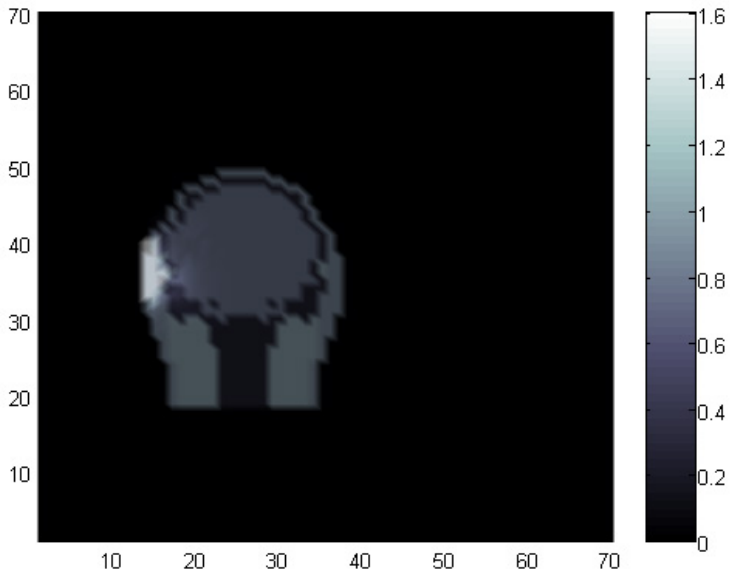

Figure 6.6: SAR distribution within the human head at $x = 0$ plane at 900 MHz (the distance between the head and the phone is zero)

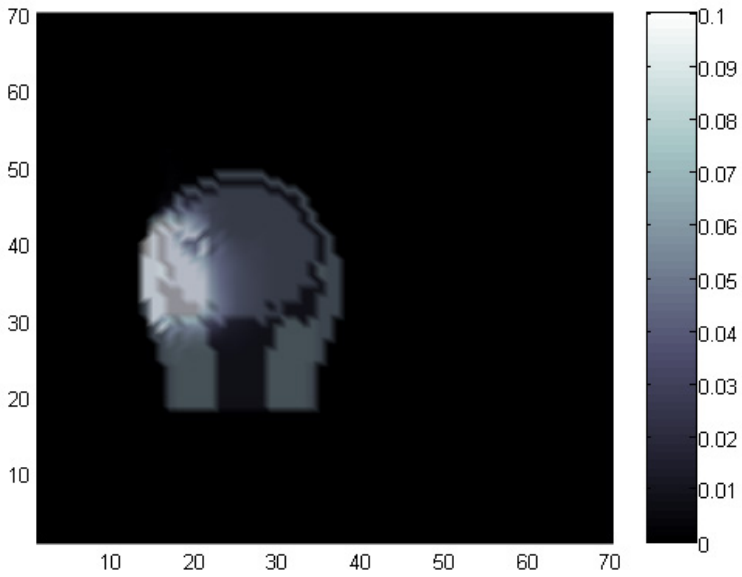

Figure 6.7: SAR distribution within the human head at $x = 0$ plane at 900 MHz (the distance between the head and the phone is zero and the scale is reduced.)

6.5.2 Second Simulation

All the specifications of this simulation are exactly the same as those given in Sec. 6.5.1, except that the distance between the front face of the phone and the head is raised to one cell. The results are given in Table 6.6 and Figs. (6.8-6.11). The table and the figures are exactly the counterparts of those in Sec 6.5.1, and they are interpreted in a similar way. In this case, it is possible to observe a considerable decrease in SAR values for some tissues. However, it is also observed that since the phone is moved away from the head, the SAR distribution is not localized, but occupies a larger volume.

Table 6.6: SAR Distributions in a Head at 900 MHz

(The distance between source and head is 3 cells and between phone front plane and head is one cell.)

	Adult Female
Peak 1-voxel SAR (W/kg)	4.9124
Peak 1-g SAR (W/kg)	1.7556
Peak 1-voxel SAR for Bone (W/kg)	0.3715
Peak 1-voxel SAR for Skin (W/kg)	4.9124
Peak 1-voxel SAR for Muscle (W/kg)	1.2501
Peak 1-voxel SAR for Brain (W/kg)	0.6309
Peak 1-voxel SAR for Humour (W/kg)	0.0212
Peak 1-voxel SAR for Lens (W/kg)	0.0069
Peak 1-voxel SAR for Cornea (W/kg)	0.0646
Peak 1-voxel SAR for Pitutary Gland (W/kg)	0.0644
Average SAR for Bone (mW/kg)	18.1
Average SAR for Skin (mW/kg)	153.9
Average SAR for Muscle (mW/kg)	85.2
Average SAR for Brain (mW/kg)	62.4
Average SAR for Humour (mW/kg)	9.2
Average SAR for Lens (mW/kg)	4.5
Average SAR for Cornea (mW/kg)	10.1
Average SAR for Pitutary Gland (mW/kg)	49.9
Average Whole Body SAR (W/kg)	0.0778

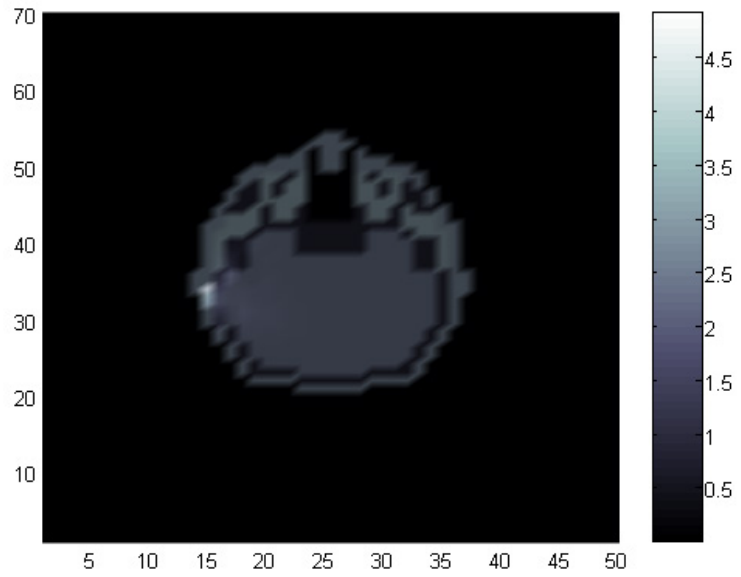

Figure 6.8: SAR distribution within the human head at $z = 0$ plane at 900 MHz (the distance between the head and the phone is one cell)

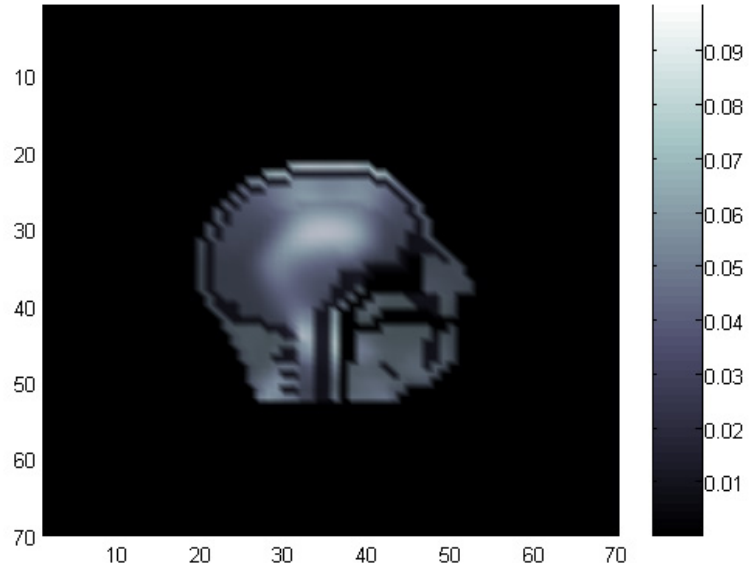

Figure 6.9: SAR distribution within the human head at $y = 0$ plane at 900 MHz (the distance between the head and the phone is one cell)

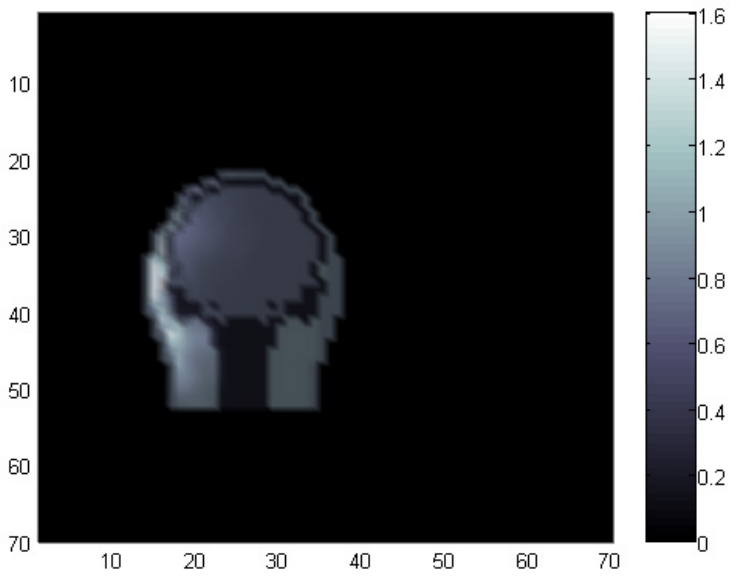

Figure 6.10: SAR distribution within the human head at $x = 0$ plane at 900 MHz (the distance between the head and the phone is one cell)

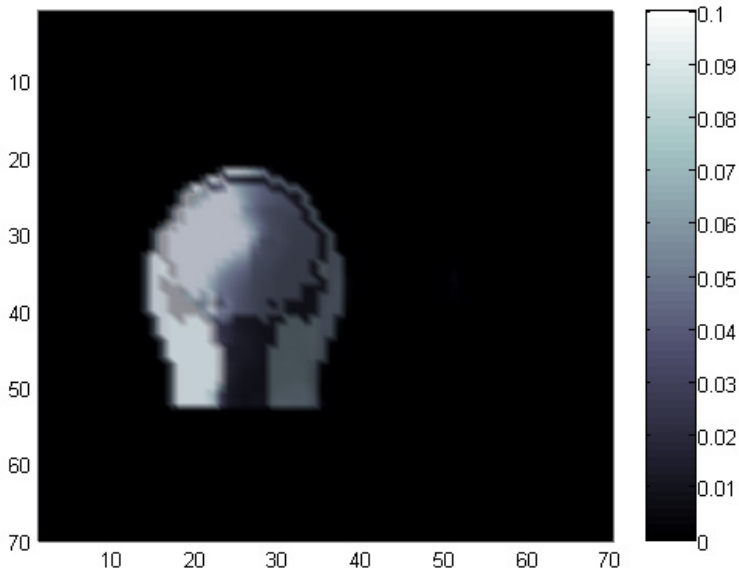

Figure 6.11: SAR distribution within the human head at $x = 0$ plane at 900 MHz (the distance between the head and the phone is one cell and the scale is reduced.)

6.5.3 Third Simulation

All the specifications of this simulation are exactly the same as those given in Sec. 6.5.2, except that the phone axis is tilted by 15º. The results are given in Table 6.7 and Figs. (6.12-6.15). The table and the figures are exactly the counterparts of those in Sec. 6.5.2, and they are interpreted in a similar way. The SAR values are now different for the corresponding voxels in the head, but the overall distribution of the values is not very different from that in Sec. 6.5.2

Table 6.7: SAR Distributions in a Head at 900 MHz (15° tilted)
(The distance between source and head is 3 cells and between phone front plane and head is one cell.)

	Adult Female
Peak 1-voxel SAR (W/kg)	4.0285
Peak 1-g SAR (W/kg)	1.8534
Peak 1-voxel SAR for Bone (W/kg)	0.4210
Peak 1-voxel SAR for Skin (W/kg)	4.0285
Peak 1-voxel SAR for Muscle (W/kg)	2.5190
Peak 1-voxel SAR for Brain (W/kg)	0.8936
Peak 1-voxel SAR for Humour (W/kg)	0.1319
Peak 1-voxel SAR for Lens (W/kg)	0.0381
Peak 1-voxel SAR for Cornea (W/kg)	0.1376
Peak 1-voxel SAR for Pitutary Gland (W/kg)	0.1022
Average SAR for Bone (mW/kg)	26.1
Average SAR for Skin (mW/kg)	183.8
Average SAR for Muscle (mW/kg)	158.9
Average SAR for Brain (mW/kg)	60.6
Average SAR for Humour (mW/kg)	50.7
Average SAR for Lens (mW/kg)	17.7
Average SAR for Cornea (mW/kg)	28.7
Average SAR for Pitutary Gland (mW/kg)	105.5
Average Whole Body SAR (W/kg)	0.1055

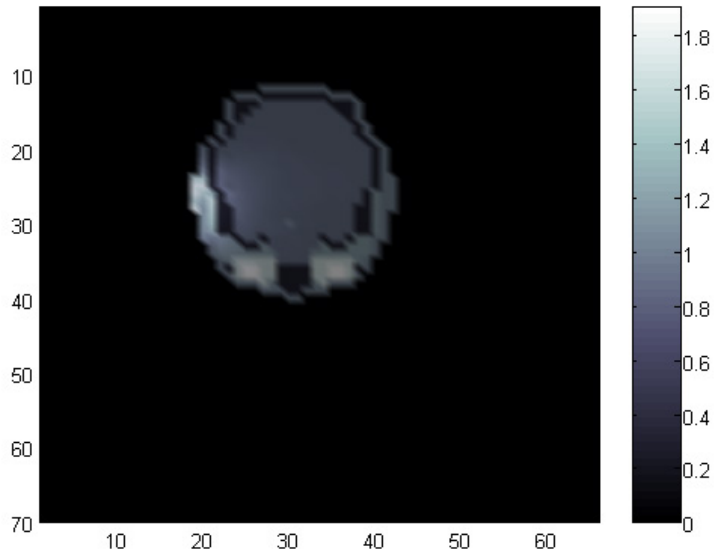

Figure 6.12: SAR distribution within the human head at $z = 0$ plane at 900 MHz (the distance between the head and the phone is zero and the phone is tilted by 15º)

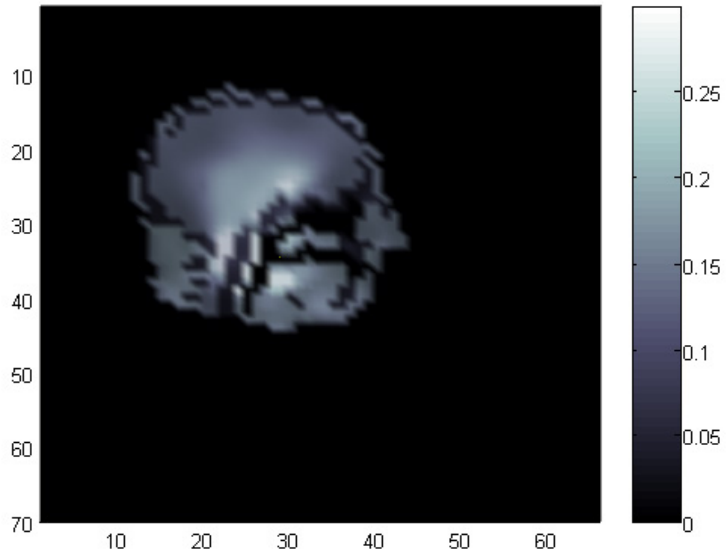

Figure 6.13: SAR distribution within the human head at $y = 0$ plane at 900 MHz (the distance between the head and the phone is zero and the phone is tilted by 15º)

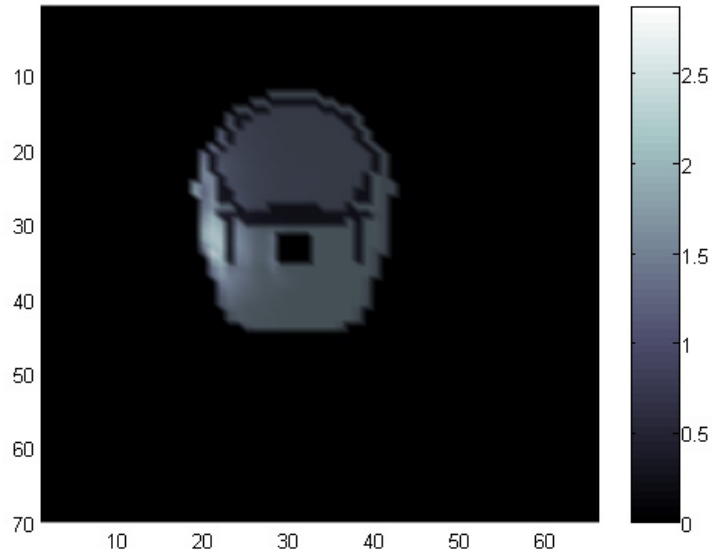

Figure 6.14: SAR distribution within the human head at $x = 0$ plane at 900 MHz (the distance between the head and the phone is zero and the phone is tilted by 15º)

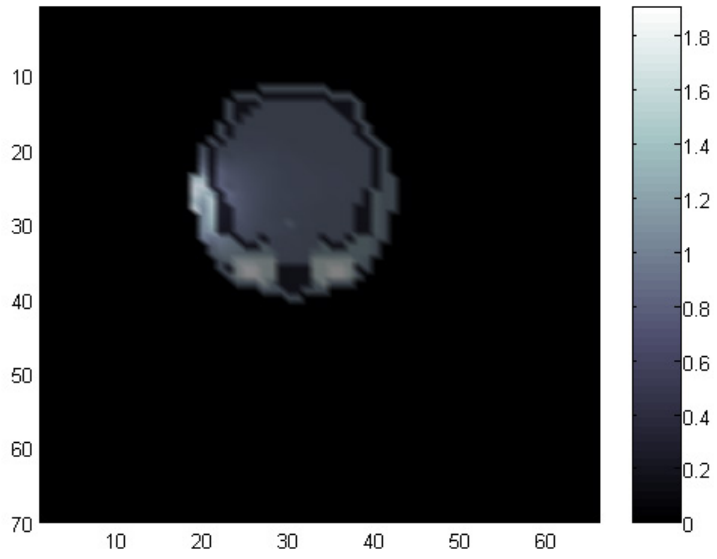

Figure 6.15: SAR distribution within the human head at z=0 plane at 900 MHz(the distance between the head and the phone is zero, the phone is tilted by 15º and the scale is reduced.)

CHAPTER 7

CONCLUSION AND DISCUSSION

The main contribution of this thesis is the development of an FDTD code to study the interaction of electromagnetic waves (created by a mobile phone) with the human head. To this end, the study has been carried out by following the steps given below:

1. A MATLAB code is developed to simulate the FDTD spatio-temporal difference equations.
2. The equations of the uniaxial anisotropic PML have been implemented and included in the MATLAB code, for the purpose of FDTD grid truncation.
3. The human head model is developed by using MRI images.
4. Antenna feed models are developed and tested in the FDTD code.
5. The phone model is developed.
6. The phone and head models are combined and SAR calculations have been carried out.

Several examples have been considered to validate the code and to obtain results related to SAR calculations, which is the main goal of this thesis. It has been observed that the obtained results are similar to those reported in the literature.

Consequently, it seems that the FDTD approach is a valuable tool in the simulation studies related to the interaction of electromagnetic waves with human tissue. It is possible to represent different body parts geometrically and the specification of the constitutive parameters is very easy.

REFERENCES

[1] R.F. Harrington, "Field Computation by Moment Methods, The IEEE/OUP Series on Electromagnetic Wave Theory", Piscataway, 1993

[2] P.P. Sylvester and R.L. Ferrari, "Finite Elements for Electrical Engineers", ISBN 0-521-37829-x

[3] Bayliss. A., Gunzburger M. And Turkel E., "Boundary conditions for the numerical solution of elliptic equations in exterior domains", SIAM J. Appl. Math., 42 pp.430-451, 1982

[4] Jean-Pierre Berenger, "Three-Dimensional Perfectly Matched Layer for the Absorpsion of Electromagnetic Waves", Journal of Computational Physics 127, 363-379 1996

[5] K.S. Yee, "Numerical Solution of Initial Boundary Value Problems Involving Maxwell's Equations in Isotropic Media", IEEE Trans. Antennas Propagat., Vol. 14, No. 3, pp. 302,307, 1966

[6] Karl S. Kunz, Raymond J. Luebbers, "The Finite Difference Time Domain Method for Electromagnetics", CRC Press, 1992

[7] A. Taflove, "Computational Electrodynamics: The Finite Difference Time Domain Method", Boston, MA: Artech House, 1995

[8] D. K. Cheng, "Field and Wave Electromagnetics", Menlo Park, CA: Addison-Wesley, 1992

[9] Stephen D.Gedney, "An Anisotropic Perfectly Matched Layer-Absorbing Medium for the Truncation of FDTD Lattices", IEEE Transactions on Antennas and Propagation, Vol. 44, No:12, December 1996

[10] G. Mur, Absorbing boundary conditions for the finite-difference approximation of the time domain electromagnetic field equations, IEEE Trans. Electromagnetic Compatibility, vol.23, 1981, pp.377-384

[11] FCC interactive program for calculation of tissue dielectric properties. Available http://www.fcc.gov/fcc-bin/dielec.sh

[12] Om P. Gandhi, Gianluca Lazzi and Cynthia M.Furse, "Electromagnetic Absorption in the Human Head and Neck for Mobile Telephones at 835 and 1900 MHz.", IEEE Trans. On Microwave Theory and Techniques VOL. 44 No:10 October 1996

[13] Constantine A. Balanis, "Antenna Theory: Analysis and Design", 2nd Edition, Wiley, 1996

[14] Evaluating Compliance with FCC Guidelines for Human Exposure to Radiofrequency Electromagnetic Fields, Supplement C (Edition 97-01) to OET Bulletin 65 (Edition 97-01), December 1997

[15] ANSI IEEE C95.1-1992 American National Standard-safety Levels with Respect to Human Exposure to Radio Frequency Electromagnetic Fields 3 kHz to 300 GHz, New York, IEEE

[16] Bernadi P., Cavagnaro M., Pisa S., Evaluation of SAR Distribution in the Human Head for CellularPhones Used in a Partially Closed Enviroment, IEEE Transactions on Electromagnetic Compatibility, Vol. 38, No 3, August 1996.

[17] Dimbylow P.J., Mann S.M., SAR calculations in an anatomically realistic model of the head for mobilecommunication transceivers at 900 MHz and 1,8 GHz, Phys. Med. Biol., 1991, Vol 39, 1994.

[18] Hombach V, Meier K., Burkhardt M., Kühn E., Kuster N., The Dependence of EM Absorption upon Human Head Modeling at 900 MHz, IEEE-Transactions on Microwave Technology, October 1995.

[19] Kuster N., Balzano Q., Energy absorption mechanism by biological bodies in the near field of dipoleantennas above 300 MHz, IEEE Transactions on Vehicular Technology, vol. 41, no. 1, Februar 1992.

[20] “Questions and Answers about Biological Effects and Potential Hazards of Radiofrequency Electromagnetic Fields”, Federal Communications Commission Office of Engineering & Technology, OET Bulletin 56, Fourth Edition, August 1999

[21] Selçuk Paker, Levent Sevgi, “FDTD Evaluation of the SAR Distribution in a Human Head Near a Mobile Cellular Phone”, ELEKTRİK. VOL.6 NO.3,1998, TÜBİTAK

[22] European Bioelectromagnetics Assc.: www.ebea.org

APPENDIX A

MRI IMAGES OF THE SAGITAL SLICES

Figure A.1: 1st MRI Image of the Sagital Slices

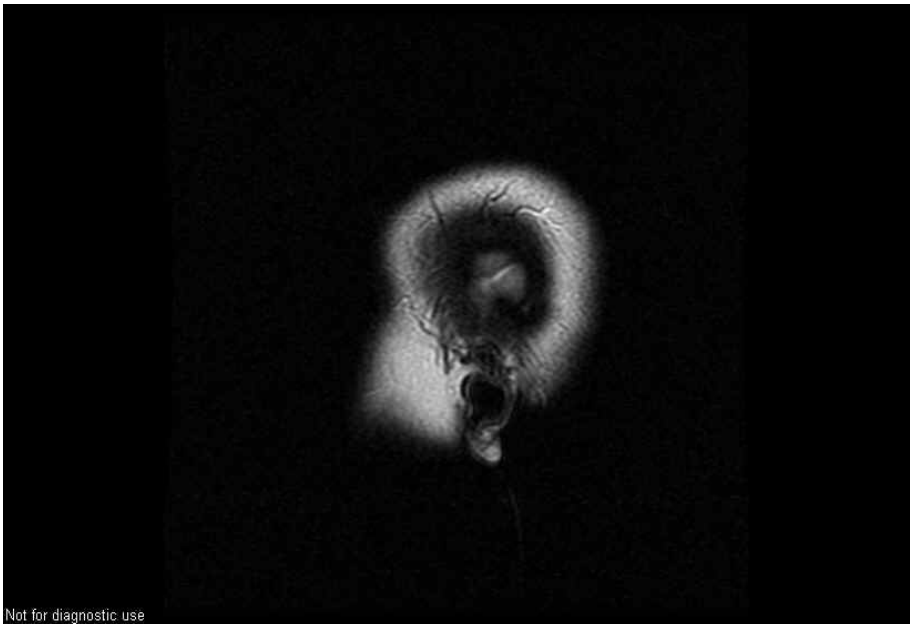

Figure A.2: 2nd MRI Image of the Sagital Slices

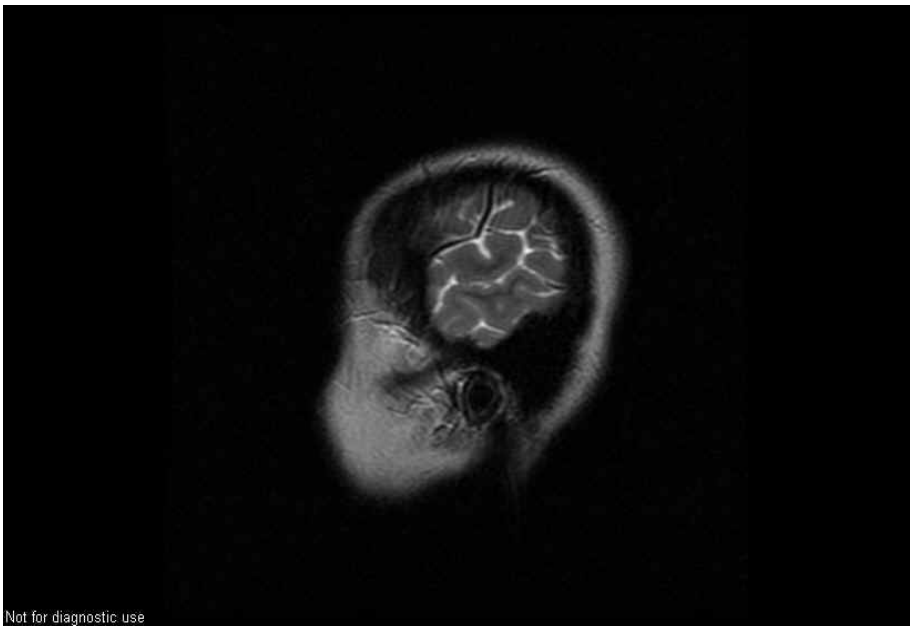

Figure A.3: 3rd MRI Image of the Sagital Slices

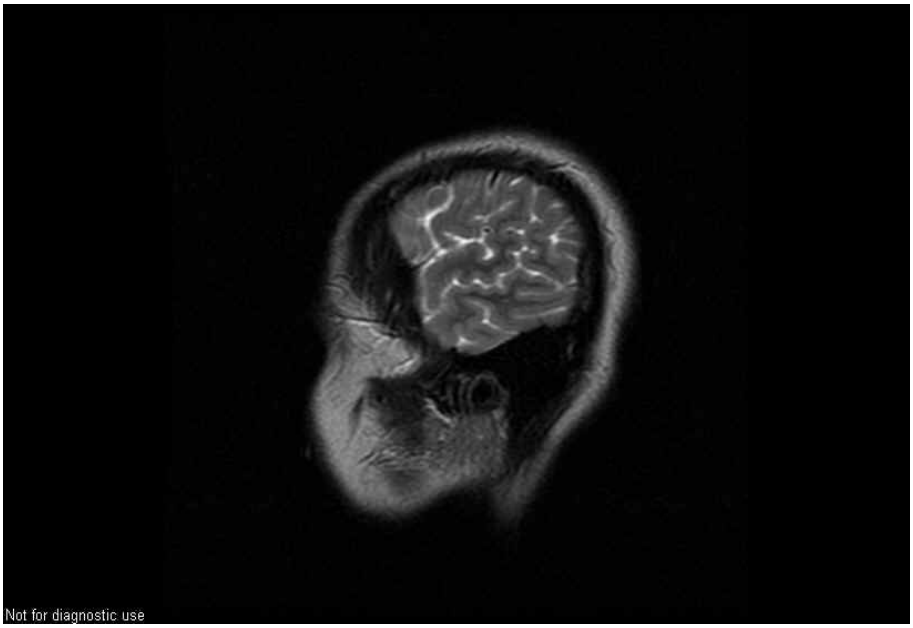

Figure A.4: 4th MRI Image of the Sagital Slices

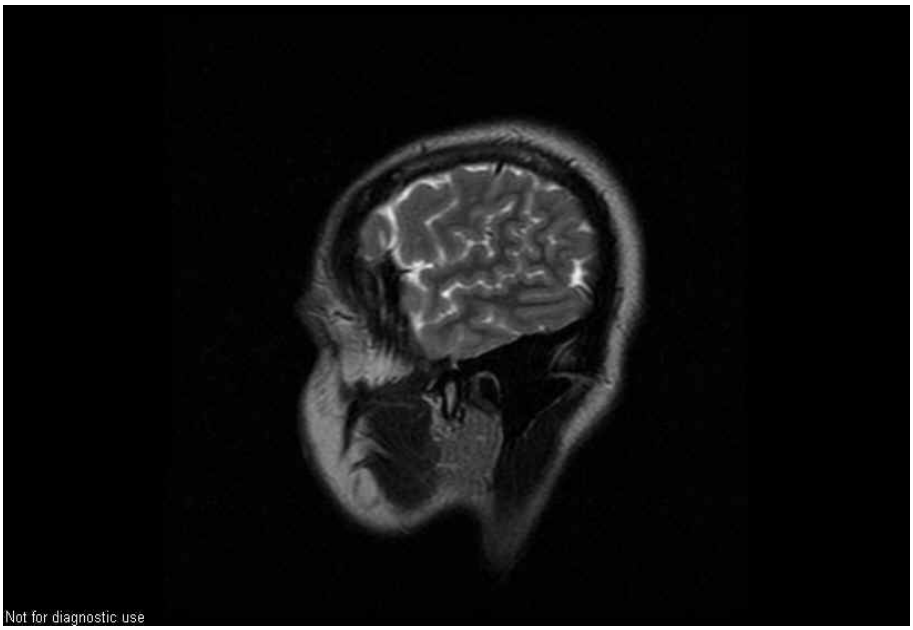

Figure A.5: 5th MRI Image of the Sagital Slices

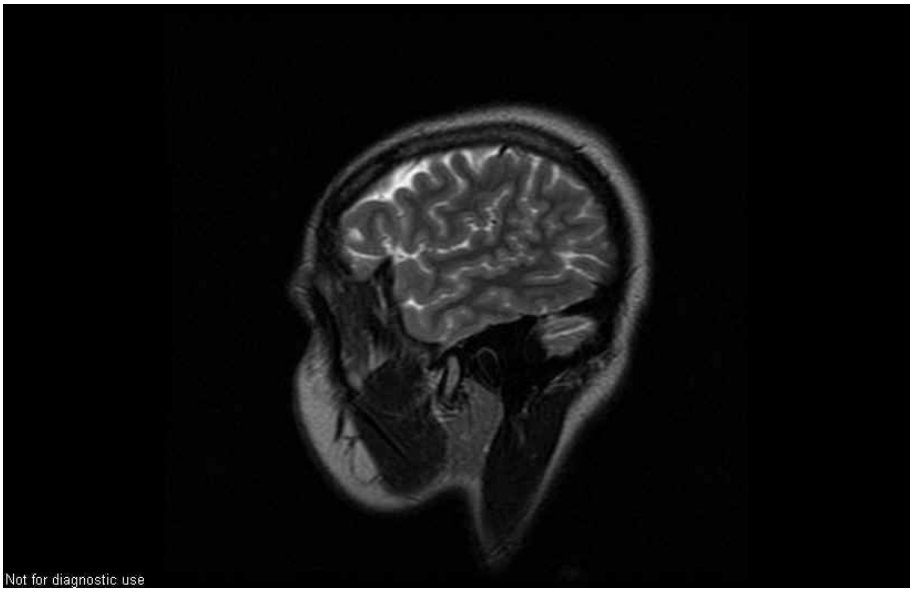

Figure A.6: 6th MRI Image of the Sagital Slices

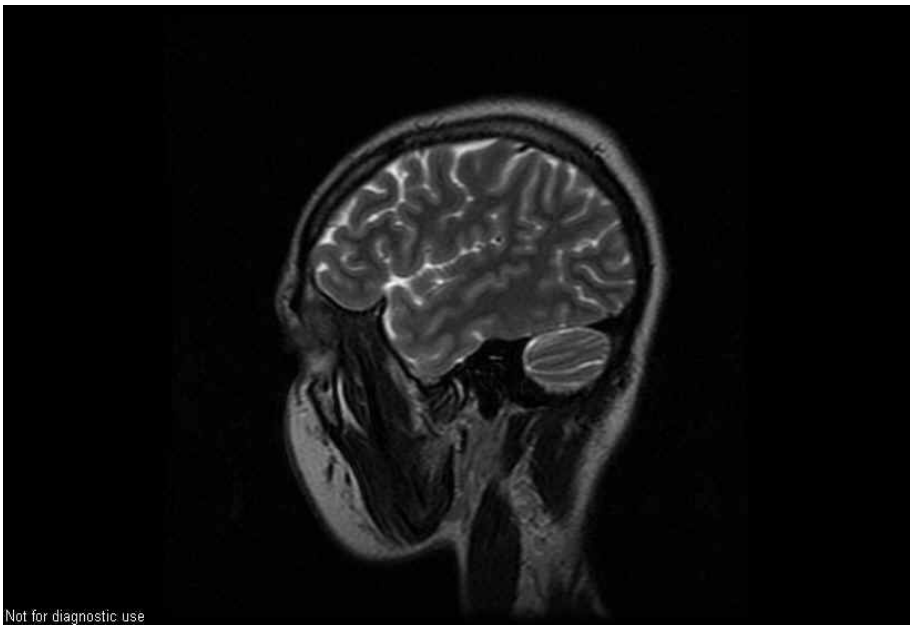

Figure A.7: 7th MRI Image of the Sagital Slices

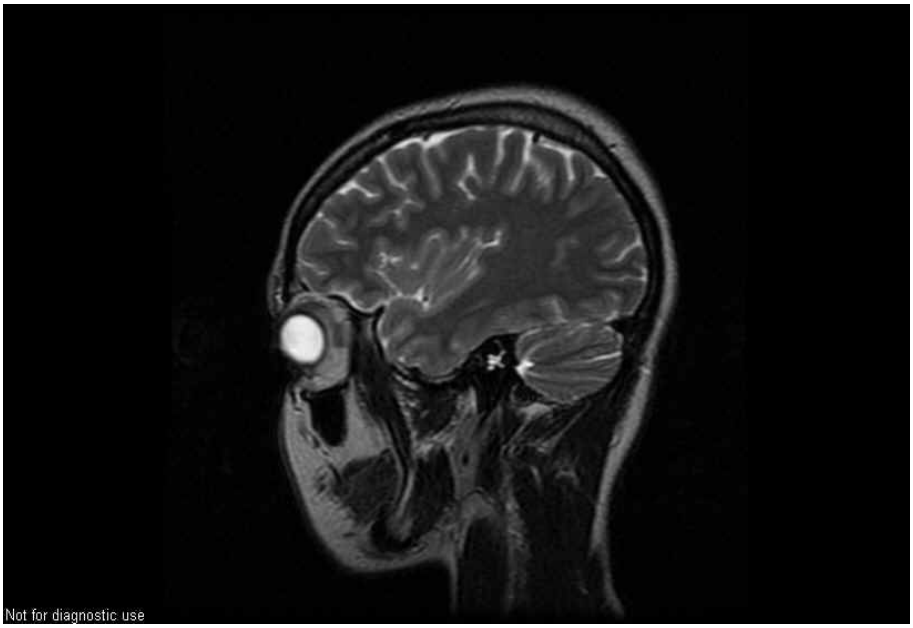

Figure A.8: 8th MRI Image of the Sagital Slices

Figure A.9: 9th MRI Image of the Sagital Slices

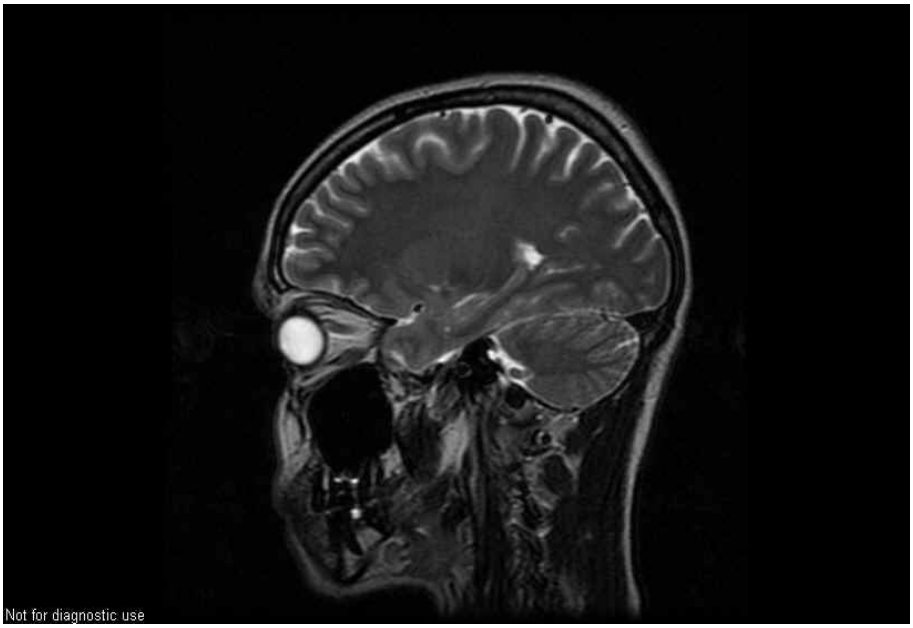

Figure A.10: 10th MRI Image of the Sagital Slices

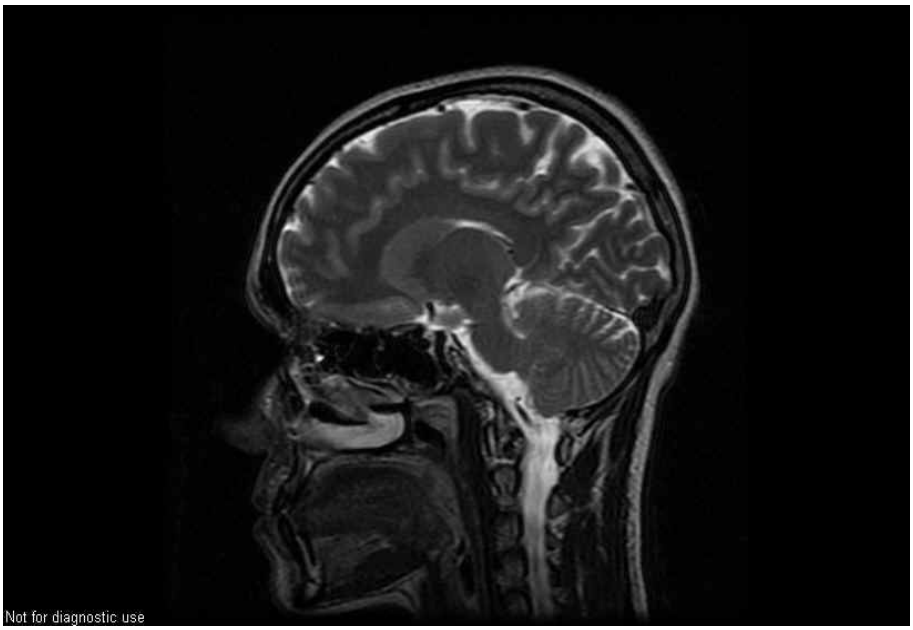

Figure A.11: 11th MRI Image of the Sagital Slices

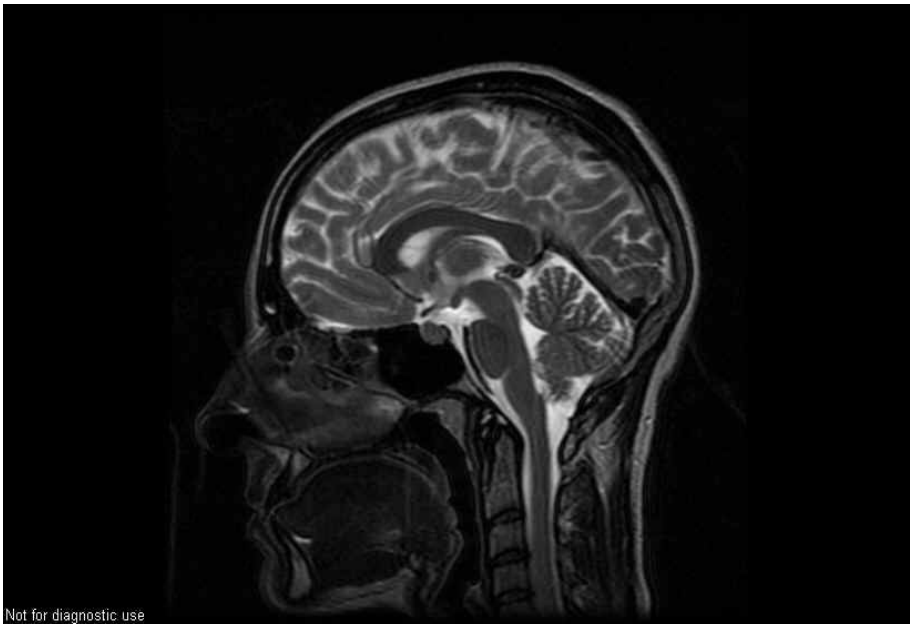

Figure A.12: 12th MRI Image of the Sagital Slices

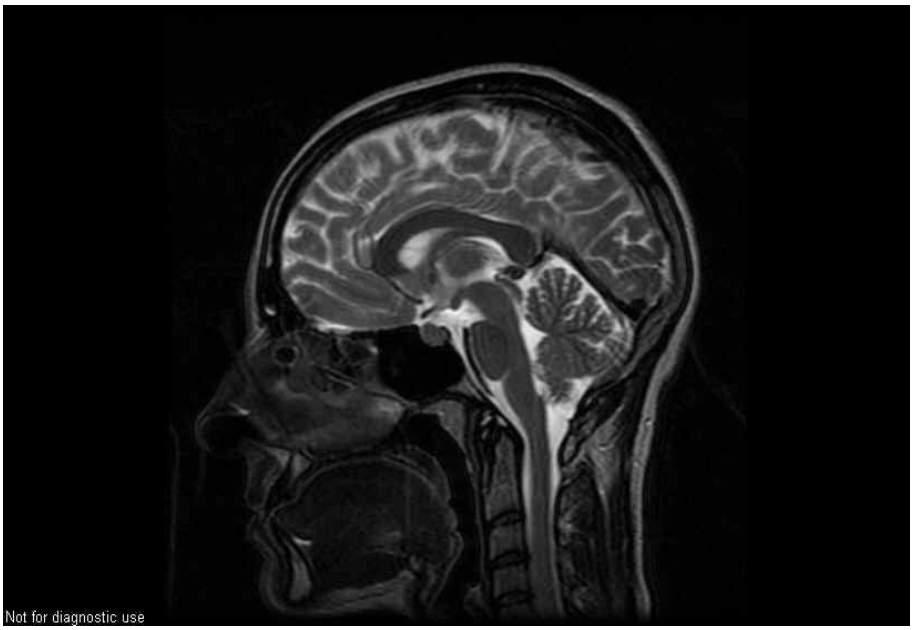

Figure A.13: 13th MRI Image of the Sagital Slices

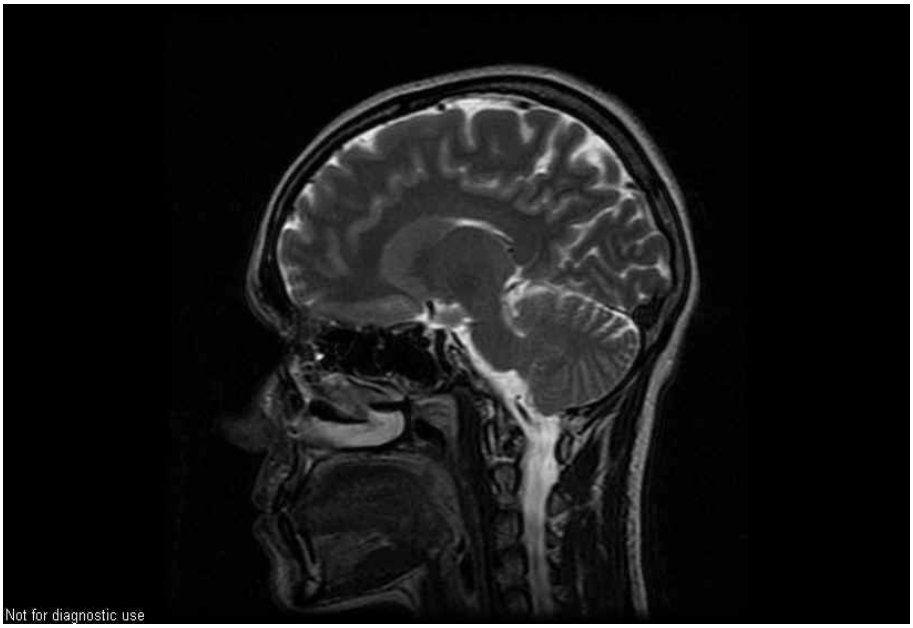

Figure A.14: 14th MRI Image of the Sagital Slices

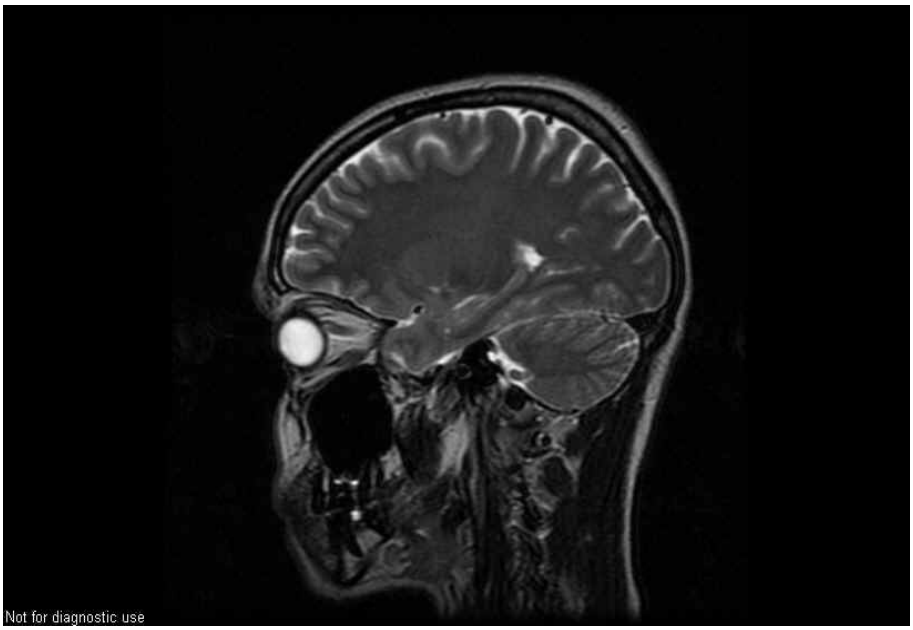

Figure A.15: 15th MRI Image of the Sagital Slices

Figure A.16: 16th MRI Image of the Sagital Slices

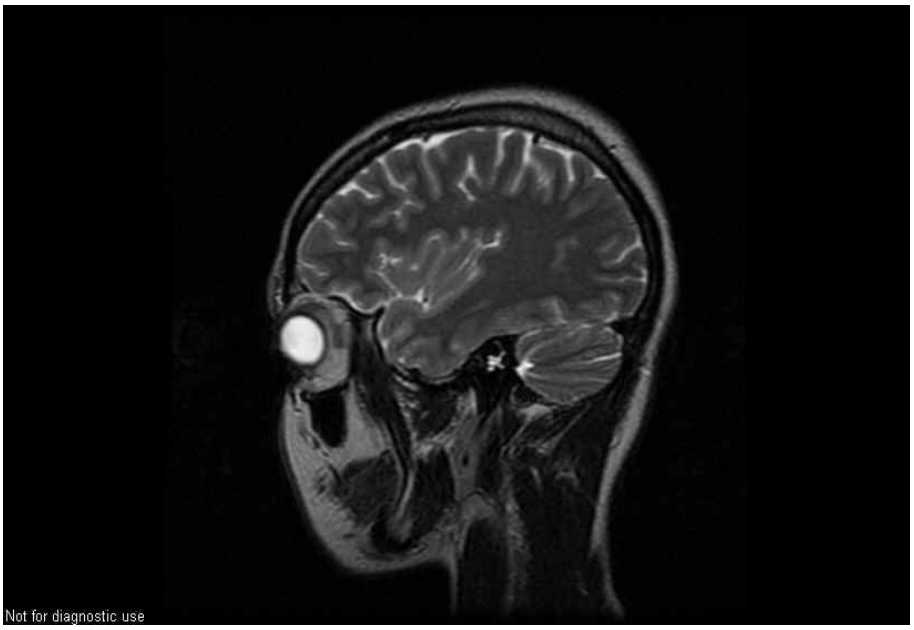

Figure A.17: 17th MRI Image of the Sagital Slices

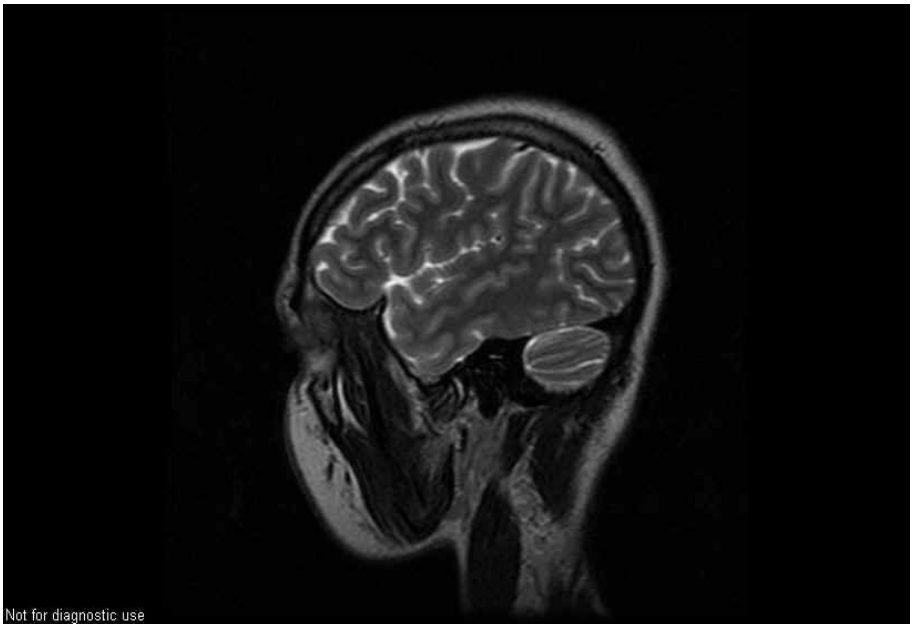

Figure A.18: 18th MRI Image of the Sagital Slices

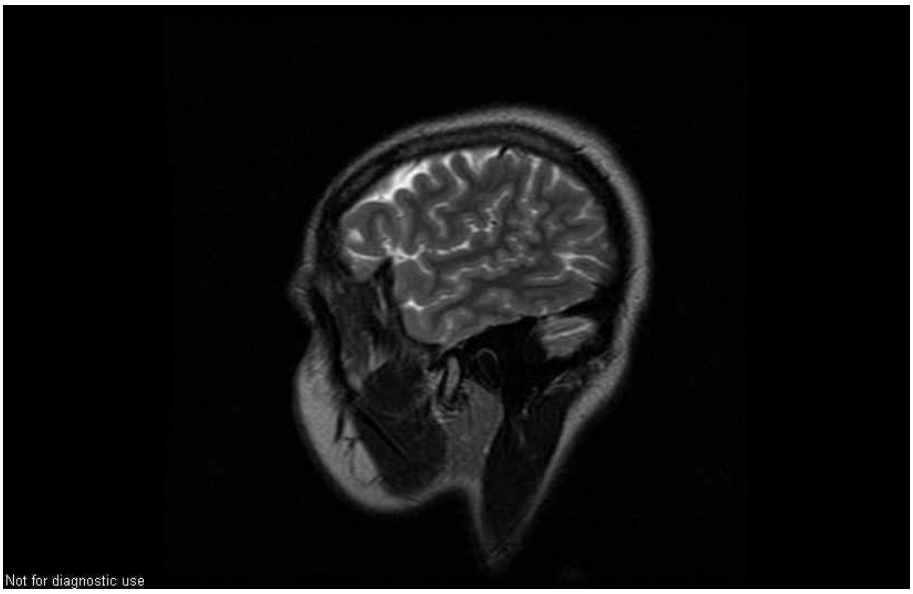

Figure A.19: 19th MRI Image of the Sagital Slices

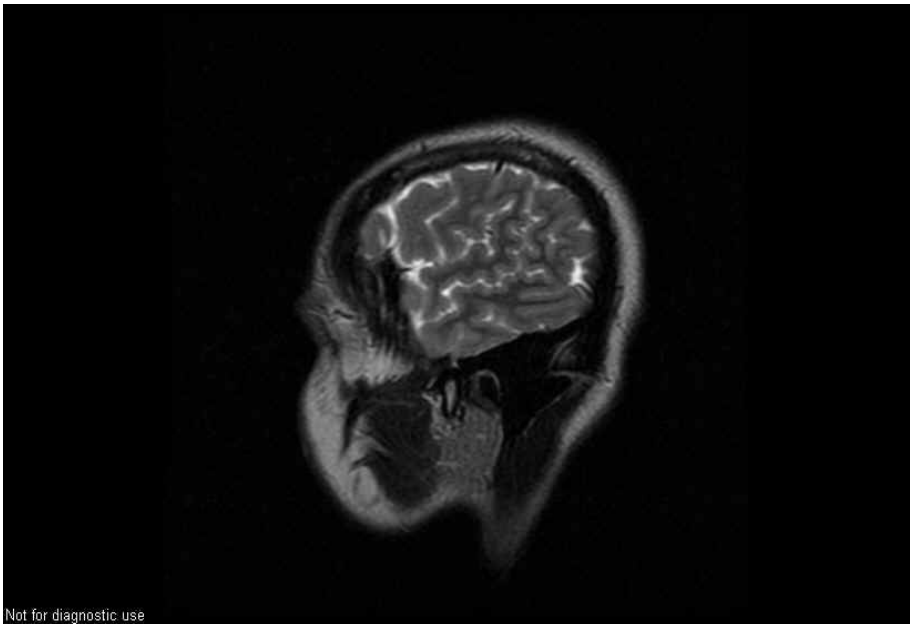

Figure A.20: 20th MRI Image of the Sagital Slices

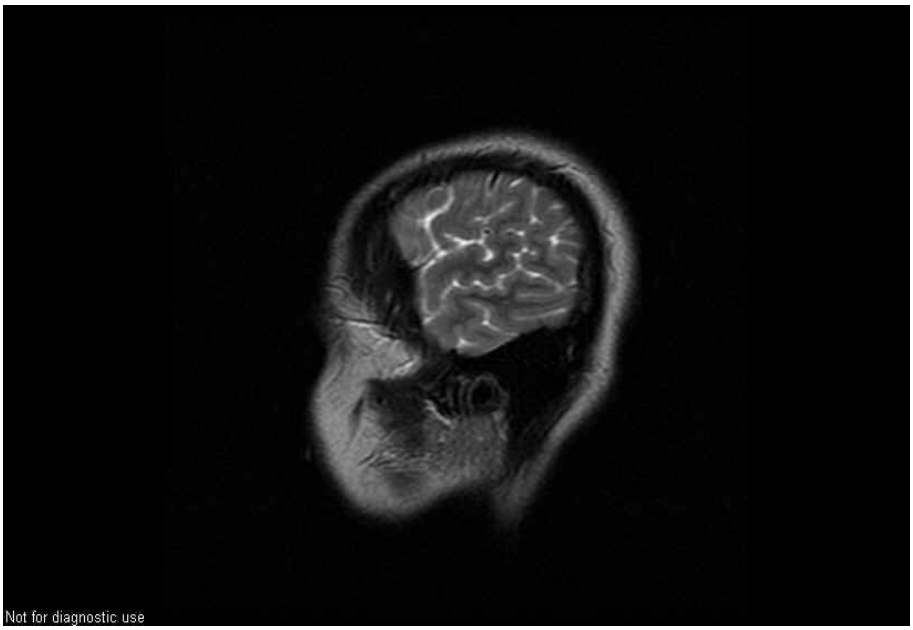

Figure A.21: 21st MRI Image of the Sagital Slices

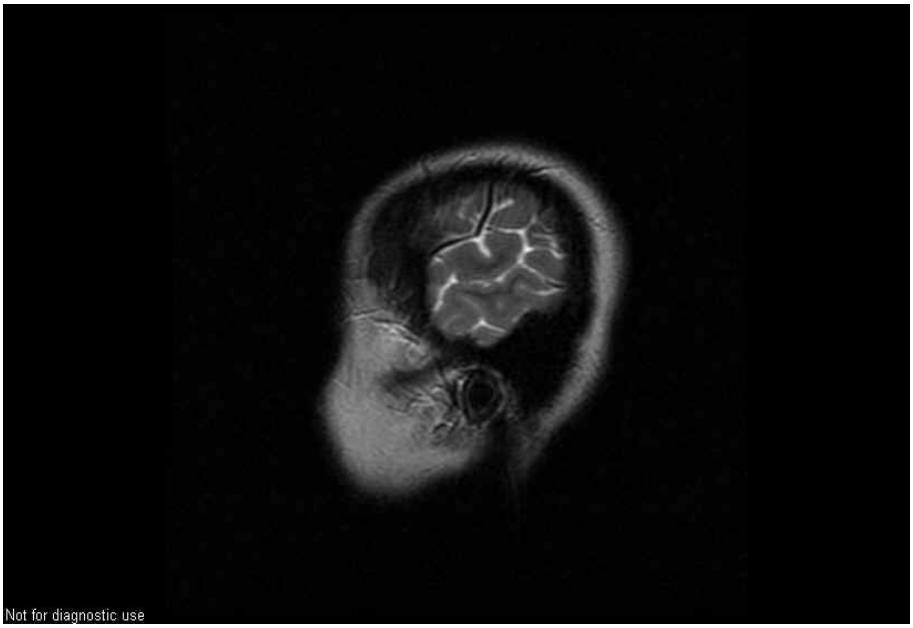

Figure A.22: 22nd MRI Image of the Sagital Slices

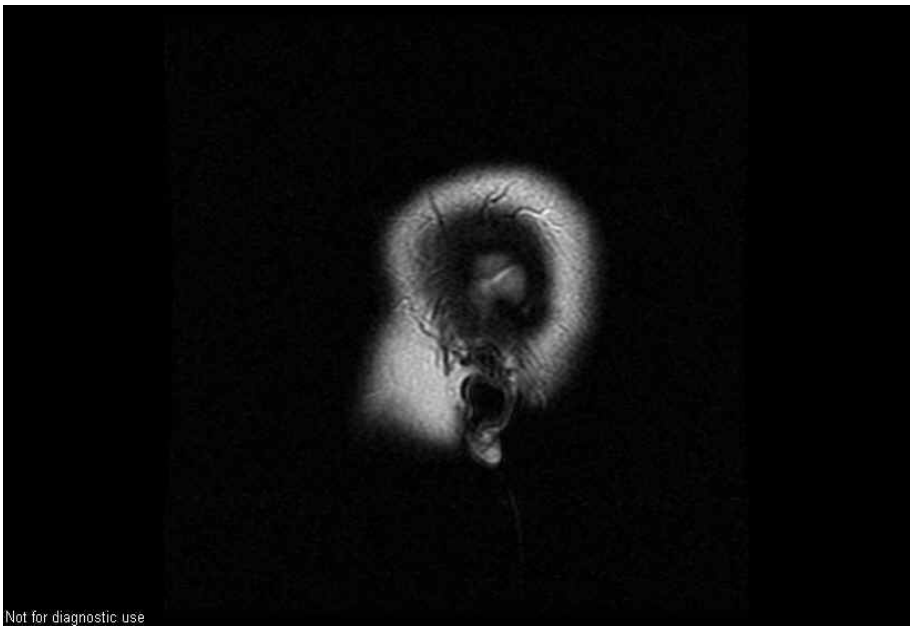

Figure A.23: 23rd MRI Image of the Sagital Slices

Figure A.24: 24th MRI Image of the Sagital Slices